Petrological Constraints on Formation of Corona around Garnet in the Lützow-Holm Complex, East Antarctica

森, 祐紀

https://doi.org/10.15017/4060000

出版情報：九州大学, 2019, 博士（理学）, 課程博士
バージョン：
権利関係：

Petrological Constraints on Formation of Corona around Garnet in the Lützow-Holm Complex, East Antarctica

東南極リュツォ・ホルム岩体に産する柘榴石周囲に発達するコロナの形成要因の岩石学的制約

March 2020

Doctoral Dissertation

Yuki MORI

Department of Earth and Planetary Sciences,

Graduate School of Science,

Kyushu University

CONTENTS

ABSTRACT

Coronas around garnet occur in high-grade metamorphic complexes all over the world. The coronas often have been used for the estimation of pressure-temperature path or mass transfer in previous studies. However, not all rocks have the coronas even if the rocks have similar mineral assemblages to that of corona-bearing rocks. Such coronas have been described in the Lützow-Holm Complex (LHC) in East Antarctica and used as evidence of decompression in the clockwise P-T paths of the complex. However, the reactions of formation of corona have been described based on textural observation only although the coronas are dealt as important evidence of decompression. Corona-free gneisses also commonly occur in the LHC. Therefore, the LHC is an appropriate example for the study of constraints for the formation of coronas. This study performed the following three subjects: (1) Textural observation of garnet-bearing mafic gneisses and determination of reactants using chemical analysis, (2) Estimation of P-T condition of Niban Rock and Akarui Point, (3) Determination of the constraints for the formation of corona.

The occurrences of coronas have been reported from ten exposures in previous studies, and the reports are limited from transitional and granulite-facies zones only. I examined 4 mafic gneisses from 4 exposures in the amphibolite-facies zone, 3 mafic gneisses from 2 exposures in the transitional zone, and 14 mafic gneisses from 10 exposures in the granulite-facies zone of the LHC. All the examined mafic gneisses contain garnet and amphibole, and plagioclase, orthopyroxene, clinopyroxene, biotite, or quartz are contained as matrix minerals. The 12 of 17 mafic gneisses from transitional and granulite-facies zones contain coronas, whereas the remains do not contain. In the amphibolite-facies zone, no corona was found although mineral assemblages are same or

similar to those of corona-bearing gneisses in transitional and granulite-facies zones.

I determined the reactant minerals using chemical analysis. All the corona-bearing gneisses contain garnet and calcic amphibole, and thus they can be candidates for reactants of coronal formation. All the examined garnet surrounded by coronas do not preserve growth zonings of major elements, and thus I selected Cr to detect it. Using high beam current of FE-EPMA, Cr zoning showing polygonal shape was detected, and the zoning is partially cut by corona. The rim is considered to have consumed by coronal formation, and thus garnet is one of reactants of coronal formation. Calcic amphiboles containing Cl were used for investigation as a reactant. Cl-bearing amphibole in corona-bearing samples show Cl-rich core and Cl-poor rim. In addition, the Cl in rim decrease with distance from corona. Cl-bearing amphibole in corona-free sample does not show core-rim structure in terms of Cl, and Cl concentration is constant in one grain. Constituent minerals of felsite-nanogranite inclusions (FNIs) are rich in Cl, and thus the melt coexisted during garnet growth were rich in Cl. Most coronal minerals cannot contain Cl in their structures. Therefore, Cl should be released from reaction front, and thus melt is one of the reactants. In addition, hornblende is one of reactants because hornblende is contained in all samples and coronas develop between garnet and hornblende.

I investigated P-T condition of Niban Rock and Akarui Point. A pelitic gneiss was used for P-T estimation of Niban Rock. Applying Zr-in-rutile geothermometer, garnet-biotite geothermometer, garnet-sillimanite-plagioclase-quartz geobarometer, and pseudosection, 650 – 701 °C (assuming pressure of 6.5 – 14 kbar) as prograde condition, 625 – 720 °C and 4.2 – 7.4 kbar as peak condition, and 654 – 687 °C and 4.5 – 5.2 kbar as retrograde condition were obtained. Low-pressure condition of Akarui Point was

estimated based on mineral assemblage of FNI in garnet surrounded by corona in a mafic gneiss. Andalusite and Cl-rich scapolite is directly contact in FNIs, and the stability fields of both minerals are over 700 °C at $P < 1.6$ kbar. Therefore, Akarui Point kept high temperature of 700 °C even at low pressure. Based on these result, amphibolite-facies zone is much lower temperature than transitional zone, and thus this difference in metamorphic temperature would be responsible for formation of corona by combining with distribution of corona in the LHC. Water-saturated basalt solidus locates almost between the temperatures of Niban Rock and Akarui Point, and thus effect of partial melting for formation of corona is considered.

I investigated the relation between partial melting and formation of corona. Previous studies found FNIs in mafic gneisses from three exposures in granulite-facies zone. In this study, FNIs were found in three samples from Akarui Point, Skallen, and Skallevikshalsen. All the garnet containing FNIs investigated in this study are surrounded by corona, and all the available photomicrographs of the garnet containing FNIs in the previous studies show corona around garnet. Therefore, melt is required for formation of corona in addition to high temperature.

In conclusions, garnet and amphibole are the reactants of coronal formation, and melt is also required to the formation. Therefore, melt should be taken into account for corona-forming reaction.

1. INTRODUCTION

1.1. Previous Study on Non-equilibrium Structures

Non-equilibrium structures, including coronas, attract the interest of petrologists because of their distinct appearance. Their structural feature that both reactants and products are preserved brings us precious clues for understanding mass transfer and diffusion during metamorphic reactions, as well as pressure (P)-temperature (T) paths (e.g., Nishiyama, 1983; Ashworth & Birdi, 1990; Nakamura, 2002; Santosh & Sajeev, 2006; Mori & Ikeda, 2018).

An essential approach when studying coronas is the determination of the net reaction of their formation. This requires judging whether the system was open or closed to various components during the reaction. The isocon method proposed by Grant (1986) enables the graphical display of differences in mass of components between the reactants and products. Applying this method to coronas between olivine and plagioclase, Ashworth & Birdi (1990) evaluated the mobility of the components and demonstrated that Al and Si were almost conserved throughout the corona formation. A statistical method, referred to as the singular value decomposition (SVD), provides possible solutions for the net reaction despite substantial analytical errors (Fisher, 1989). Chowdhury et al. (2013) applied the SVD method to double-layered spinel-plagioclase coronas between corundum and hornblende. Four plausible net reactions were proposed based on the textural constraints such as the volume ratio of the spinel and plagioclase, and the occurrence of the spinel as pseudomorphs after corundum by which they assumed no volume change to form the spinel after corundum. All the plausible reactions indicated

that Al was almost conserved within the coronas and the neighboring hornblende.

The determination of the position of the initial boundary between the reactant phases allows us to clarify the growth directions of the layers and the mass transfers across the layer boundaries (e.g., Fukuyama et al., 2006; Mori & Ikeda, 2018). Fukuyama et al. (2006) examined the triple-layer reaction zones of diopside, garnet, and wollastonite between metamorphosed mafic dykes and marble. The occurrence of residual calcite within the diopside zone suggested that the initial boundary was set in this zone, and the reasonable growth directions were determined. By performing the two steady-diffusion models for open systems proposed by Ashworth & Birdi (1990) and Johnson & Carlson (1990), they obtained the stoichiometric relations and quantitative mass transfers across the boundaries. Mori & Ikeda (2018) dealt with triple-layer coronas between corundum and hornblende in a mafic gneiss from the Lützow-Holm Complex, East Antarctica. They constrained initial boundary between garnet and hornblende based on the spatial distribution of brownish-green spinel. The SVD method was applied to estimate the amounts of mass transfer with assumption of Al as closed component, and they revealed that the reaction of formation of corona should be open system with respect to Na_2O and CaO, Na_2O and MgO, or CaO and SiO_2. Based on the calculation of volume changes between products and reactants, the corona-forming reaction took place during the decompressional stage of the complex.

Driving force of mass transfer is also focused in some studies. Nakamura (2002) dealt with plagioclase corona developed between kyanite and quartz in eclogitic rock and revealed that gradient of chemical potential between two intergranular regions arisen during decompression is a driving force of mass transfer. Anorhite content of plagioclase near kyanite shows higher than that near quartz. He explained that this variation is caused

to attain local equilibrium at local areas around kyanite and quartz by illustrating a Gibbs free energy diagram in binary components.

1.2. Previous Description of Corona in the LHC

Coronas around garnet in the LHC have been described in some previous studies since the 1980s (e.g., Yanai et al., 1984). In particular, the coronas have been regarded as important evidence for decompression in a clockwise pressure-temperature path of the complex (e.g., Hiroi et al., 1991; Iwamura et al., 2013; Takamura et al., 2017). For example, Iwamura et al. (2013) conducted pseudosection analysis on a mafic gneiss from Akarui Point. The corona develops around garnet and shows symplectitic texture composed of plagioclase, orthopyroxene, spinel, and sapphirine. Based on their textural observation, they considered that the breakdown reaction of garnet into the coronal minerals (i.e., garnet → plagioclase + orthopyroxene + spinel ± sapphirine) took place in the sample. In their pseudosection, garnet appears in high-pressure P-T fields (about > 9.5 kbar at 900 °C). Therefore, they concluded the sample experienced a decompression from high-P conditions, and the P-T path of the LHC was clockwise.

The coronas have a variation in their constituent minerals, e.g., biotite + plagioclase (Ikeda and Shimada, 2015), orthopyroxene + spinel + plagioclase ± sapphirine (e.g., Hiroi et al., 1991; Iwamura et al., 2013), and orthopyroxene + plagioclase (e.g., Takamura et al., 2017). The coronas have been previously found in mafic gneisses from 10 exposures, and they are summarized in Table 1-1. Exceptionally, at Rundvågshetta, pelitic gneisses also contain garnet surrounded by corona composed of plagioclase + cordierite (e.g., Kawasaki et al., 1993).

As mentioned above, Iwamura et al. (2013) considered the breakdown reaction of garnet as the corona-forming reaction. However, other authors described other corona-forming reactions based on textural observation. For example, the following four reactions were proposed in previous studies:

Grt + Qtz → Pl + Opx (e.g., Fraser, 2000; Osanai et al., 2004),

Grt + Cpx → Pl + Opx (e.g, Fraser, 2000),

Grt + Amp ± Cpx → Opx + Pl + Mgt + H_2O (e.g., Fraser, 2000),

Grt + Cpx + Qtz + H_2O → Pl + Hbl (e.g., Takahashi & Tsunogae, 2017).

1.3. Difficulty in Studying on High-grade Metamorphic Rocks

One of the difficulties in studying high-grade metamorphic rocks is determination of metamorphic history. At high-temperature conditions, atoms in minerals easily diffuse, and composition of prograde stage is modified by peak and retrograde metamorphism. In grains of garnet, homogenization of chemical zoning by volume diffusion takes place at high temperature over 700 °C (e.g., Yardley, 1977). In addition, high-grade metamorphism is often associated with mass transfer by fluid activity or melt migration, and they significantly affect chemical compositions of whole rock and constituent minerals (e.g., Takahashi & Tsunogae, 2017).

This difficulty also make study on corona difficult. On the corona, determination of product is quite easy because product minerals surround a mineral grain and shows textural difference from matrix (e.g., symplectite). Although determination of products is so easy, determination of reactants is difficult because of re-equilibrium during retrograde stages. In addition, compositions of reactants may have been affected by open

components released by corona formation (e.g., Chowdhury et al., 2013). In previous studies on coronas, determination of reactants has solely depended on textural observation only even though determination of reactants is necessary for the use of corona for P-T path estimation performed in the previous studies.

To confront the difficulty, selection of elements that lesser affected by re-equilibrium during retrograde stages is key to determine reactants. However, high-temperature metamorphic rocks may also experience partial melting or be affected by fluid infiltration. Therefore, elements that can be incorporated by melt and fluid as well as minerals or are almost immobile in minerals even at high temperature should be selected.

Cl is one of such elements. Only limited major rock-forming minerals such as biotite, amphibole, scapolite, and apatite can incorporate Cl into their crystal structures (e.g., Mi & Pan, 2018). Melt and fluid can also incorporate Cl as their component. Therefore, Cl has been used in some previous studies that investigate behavior of bubbles in magma, or brine infiltration into high-grade metamorphic rocks (e.g., Higashino et al., 2019; Yoshimura et al., 2019). However, incorporation of Cl into biotite or amphibole is believed that it sometimes controlled by original concentration of Mg in the minerals, i.e., Mg-Cl avoidance (e.g., Munoz, 1984; Morrison, 1991). Although Mg-Cl avoidance is reported in many previous studies, the nature is still unclear whether more Cl can be incorporated by Mg-poor composition or Cl can eliminate Mg to be incorporated into biotite or amphibole. Therefore, evaluation of effect of Cl on rock-forming minerals should be carefully discussed by comparing many case studies.

Trace elements in rock-forming minerals are also a good tool because trace elements often have much smaller diffusivity than that of major components. For example,

P in garnet is often used for discussion of garnet growth in pelitic rock occurring in high-grade metamorphic complex (e.g., Hiroi et al., 1997; Kawakami & Hokada, 2010; Hiroi et al., 2019; Suzuki & Kawakami, 2019). Kawakami & Hokada (2010) performed elemental mapping of P in garnet from Skallevikshalsen in the LHC. The garnet shows distinct zoning of P-poor core and P-rich rim. The P-poor core shows irregular shape, and thus they explained the P-rich rim grew over the core after resorption stage of garnet, indicating two-stage garnet growth. Other trace elements in garnet (e.g., Y, Ti, Cr) also show slow volume diffusion and are also useful to detect original zoning pattern (e.g, Yang & Rivers, 2002; Li et al, 2018).

1.4. P-T Estimation of High-grade Metamorphic Rocks

The records of prograde stage as major components of minerals in high-temperature metamorphic rocks are often erased because of high diffusion rate at high-temperature conditions, as mentioned before. In addition, some minerals existed early stage of metamorphism already may be broken down and can be detected only as inclusion, pseudomorph, or reaction product.

Pseudosection is a method to calculate stability fields of certain mineral assemblage based on whole-rock compositions and activity model of minerals (e.g., Perple_X by Connolly, 2005; THERMOCALC by Holland & Powell, 2011; Theriak-Domino by de Capitani & Petrakakis, 2010). The Perple_X software developed by Connolly (2005) calculate stability fields of certain mineral assemblages based on whole-rock composition and activity models of minerals to minimize the total Gibbs free energy. Nakano et al. (2011) calculated peak P-T condition that is already erased by retrograde

metamorphism of amphibolitized olivine granulite from the Sør Rondane Mountains, East Antarctica using Perple_X. Bulk composition of spinel + orthopyroxene symplectite was input to the software, and they found that garnet that is presently lack in the rock is required to make the symplectite. Calculation using whole-rock composition revealed that the missed P-T condition was 12 kbar at 1000 °C although the granulite presently records a subsequent amphibolite-facies overprint (<700 °C at <6 kbar).

Geothermometers based on trace elements in rock-forming minerals are also useful tools to reveal metamorphic conditions. For example, Zr concentration in rutile is known that it corresponds to its crystallization temperature when the rutile coexisted with zircon and quartz (e.g., Zack et al., 2004; Watson et al., 2006; Ferry and Watson, 2007; Tomkins et al., 2007). Especially rutile enclosed in garnet records the temperature at entrapment because the rutile can escape from re-equilibrium among rutile, quartz, and zircon, and exchange of Zr between rutile and garnet after entrapment is believed to be small. These natures of Zr in rutile have worked for deciphering metamorphic temperature of highly re-crystallized or altered rocks (e.g., Suzuki & Kawakami, 2019). Trace element geothermometers are also owing to progress in analytical instrument. For example, field-emission type electron-probe microanalyzer (FE-EPMA) can emit stable high beam current, and recent detectors can count weak X-rays from trace elements of several ppm within very small counting error enough to applying for geothermometer.

1.5. Significance of Performing a Study in the Lützow-Holm Complex on Corona around Garnet

Coronas around garnet are ubiquitous in high-grade metamorphic complex all over the

world (e.g., Nakano et al., 2013; Takamura et al., 2015; Faryad & Fišera, 2015). However, not all garnet occurring in high-grade metamorphic complex shows corona, and such garnet without corona is also common (e.g., Arima et al., 2011; Schantl et al., 2019).

Based on my compilation of occurrence of coronas around garnet in the LHC summarized above, mafic gneisses from the amphibolite-facies zone do not have the coronas, whereas those from transitional and granulite-facies zones contain the coronas. Therefore, the LHC is a good locality to compare the corona-free and corona-bearing samples directly in one metamorphic complex.

1.6. Purpose of This Study

As mentioned above, reactants of coronal formation have been depended on textural observation only. The determination of reactant is very important because lack of reactants must not form corona. I will determine that what minerals should be examined in this study based on textural observations of many corona-bearing and corona-free samples collected from entire area of the LHC. I will carefully determine the reactant minerals by performing chemical analysis in terms of elements that can be detected even the samples are affected retrograde metamorphism or alteration. Combining detailed textural observation, I will determine what control the corona formation.

I consider that the compilation of occurrence of coronas are giving a hint of possible controlling factor on the presence of corona. That is, metamorphic temperature may have a potential to constrain the corona formation.

The metamorphic grade of the LHC has been considered to show progressive increase from the upper amphibolite facies to granulite facies toward the southwest of the

complex (Hiroi et al., 1991). However, this progressive metamorphic condition is questioned in some recent studies as described in a later section. In addition, P-T conditions of amphibolite-facies zone have not well studied. To investigate whether the metamorphic condition affected corona formation or not, re-examination of P-T path of exposures in amphibolite-facies zone is essential. I consider that Niban Rock in the amphibolite-facies zone is appropriate exposure to estimate P-T condition for the study of corona formation because the position in the LHC is close to the boundary between amphibolite-facies and transitional zones. I also confirmed that the studied mafic gneiss from Niban Rock does not contain corona around garnet as shown later, and coronas have not reported from the exposure by previous studies. The metamorphic condition of Niban Rock was estimated by only one previous study of Hiroi et al. (1983). However, detailed P-T condition of each stage of prograde, peak, and retrograde of the exposure has not been estimated. Therefore, I examine the P-T path of Niban Rock. In addition, P-T condition at low pressure of Akarui Point in transitional zone also should be investigated because the exposure locates near the boundary between transitional and amphibolite-facies zones and coronas occur in the exposure. I will compare the P-T paths of Akarui Point and Niban Rock as representative exposures that corona occurs and corona does not occur.

Therefore, the following are the subjects of this study.

- Determination of reactants based on chemical analyses.
- Estimation of metamorphic conditions of Niban Rock and Akarui Point.
- Determination of what controls formation of corona around garnet in the LHC.

The mineral abbreviations used in this paper are after Whitney and Evans (2010).

Table 1-1 Coronas in mafic gneisses from the LHC reported in previous studies.

Exposure	Coronal Mineral Assemblage	Reference (e.g.)
Cape Hinode	Hbl + Bt + Pl	Hiroi et al. (2008)
Tenmondai Rock	Opx + Pl	Takamura et al. (2017abst)
Akarui Point	Opx + Pl + Spl ± Spr	Hiroi et al. (1986)
East Ongul Island	Bt + Pl	Ikeda & Shimada (2015abst)
Telen	Opx + Pl	Koizumi et al. (2014)
Skallen	Opx + Pl	Osanai et al. (2004)
Skallevikshalsen	Opx + Pl ± Mgt	Suda et al. (2006)
Rundvågshetta	Opx + Pl + Mgt	Suda et al. (2006)
Austhovde	Opx + Pl ± Hbl	Takahashi & Tsunogae (2017)
Innhovde	Opx + Pl	Shiraishi & Yoshida (1987)

2. GEOLOGICAL SETTING

2.1. Regional Geology

The LHC is one of Neoproterozoic-Cambrian high-grade metamorphic complex along the Prince Olav Coast and Lützow-Holm Bay in eastern Dronning Maud Land, East Antarctica (Fig. 2-1). It is bounded by the Western Rayner Complex to the east and the Yamato-Belgica Complex to the west in East Antarctica (e.g., Hiroi et al., 1991; Shiraishi et al., 2003) (Fig. 2-1). The main lithology of the LHC is well-layered pelitic to psammatic and intermediate gneisses with minor amounts of metamorphosed mafic to ultramafic gneiss occurring as lenticular masses or thin layers in metasedimentary gneisses (e.g., Hiroi et al., 1991).

The metamorphic grade increases progressively from the upper amphibolite facies to granulite facies toward the southwest of the complex. The LHC is divided into three metamorphic zones referred to as the amphibolite-facies zone, transitional zone, and granulite-facies zone (Hiroi et al., 1983a, 1987, 1991) (Fig. 2-2). The presence of Ca-poor amphiboles and the absence of orthopyroxene characterize the amphibolite-facies zone, while Ca-poor amphiboles are absent, and orthopyroxene is present in the granulite-facies zone. The transitional zone is characterized by the occurrence of both Ca-poor amphiboles and orthopyroxene (Hiroi et al., 1983a; Shiraishi et al., 1984).

The continuity and framework of the LHC is still in argument. The most obvious discontinuity is found around Cape Hinode, an exposure located on the eastern part of the Prince Olav Coast between Niban Rock and Akebono Rock. Shiraishi et al. (1994) reported 1017 Ma of metamorphic age of metatrondjemite from Cape Hinode, which is

much older than major metamorphic ages of the LHC. Hiroi et al. (2006) describe the high-grade metamorphic rocks corresponding to granulite facies, which is apparently higher grade than that of neighboring exposures of Niban Rock and Akebono Rock. Nogi et al. (2013) performed aerogeophysical survey over the LHC and found boundaries among magnetic anomalies around Cape Hinode. They also proposed a possibility that strike-slip is responsible for such discontinuity in the LHC and Cape Hinode was originally a component of Western Rayner Complex. Therefore, Cape Hinode is presently regarded as an allochthonous unit in the LHC. Recently, Suzuki & Kawakami (2019) reported that the metamorphic condition of Akarui Point located in the transitional zone attained 844 °C at high-pressure stage using Zr-in-rutile geothermometer for pelitic gneiss. They concluded that metamorphic zone mapping based on matrix minerals does not reflect the highest metamorphic condition.

The ultra-high temperature metamorphism was confirmed from Rundvågshetta and Skallevikshalsen (e.g., Motoyoshi et al., 1985; Kawakami & Motoyoshi, 2004). Kawasaki et al. (2011) estimated the peak P-T conditions of Rundvågshetta, the highest-grade area of the LHC, as 1040 °C, 1300 – 1500 MPa. The subsequent retrograde conditions were 1010 °C, 1000 MPa, and 830 °C, 610 MPa.

Recently, Hiroi et al. (2019) described the occurrence of felsite-nanogranite inclusions (FNIs) from Rundvågshetta and estimated decompressional P-T path based on the occurrence of andalusite in FNIs. The FNIs are considered to have been originally trapped as melt and crystallized during decompression or cooling. In the LHC, FNIs are found from West Ongul Island, Honnör Okuiwa Rock, Skallevikshalsen, Rundvågshetta, Austhovde, and Botnnuten. According to description of Hiroi et al. (2019), FNIs are found in only three mafic granulites from Skallevikshalsen, Rundvågshetta, and Austhovde.

Symplectites around garnet, and relic inclusions of kyanite and staurolite in plagioclase and garnet are commonly recognized from some exposures in the LHC, and they are regarded as evidences for a clockwise P–T path (e.g., Hiroi et al., 1983a, 1983b, 1986; Kawasaki et al., 1993; Fraser et al., 2000; Iwamura et al., 2013). Andalusite locally occurs in the rock matrix and is considered as a product due to intrusion of granites at ca. 500 Ma after main regional metamorphic event (Hiroi et al., 1983).

2.2. Fluid Activity

Fluid activities in the LHC have been reported in some previous studies. Their evidence is recorded as mineral composition or fluid inclusion. Satish-Kumar et al. (2006) focused on reaction textures in scapolite boudins occurring at Skallen. The scapolite shows Cl-rich core, indicating infiltration of Cl-rich fluid during prograde stage. Based on scapolite-fluid equilibria and thermometry using CO_2-fluid inclusion in healed fractures in scapolite poikiloblasts, they revealed that the composition of scapolite preserves the temperature of >600 °C and a minimum pressure of 3.8 kbar. Kawakami et al. (2016) found that inclusion biotite in garnet in garnet-sillimanite gneiss from Skallevikshalsen is rich in Cl. Combining with result of age dating, Cl-rich fluid infiltrated at about 560 – 500 Ma accompanied with partial melting. Takahashi & Tsunogae (2017) dealt with garnet-pyroxene granulite from Austhovde. The grains of garnet, plagioclase, and quartz in their samples enclose CO_2-rich fluid inclusions. Primary fluid inclusions in garnet shows too low in density that it is considered to have been trapped during post-peak decompression stage. However, according to their P-T pseudosection, garnet does not growth during retrograde stage and cannot trap fluid inclusions. Therefore, they explained

that such fluid inclusion would be affected by partial fluid leakage during decompression. Secondary fluid inclusions in garnet and plagioclase indicate that CO_2 fluid activity also occurred during decompression stages of 2.5 – 4.0 kbar at 750 – 900 °C, according to their isochores.

2.3. Geochronology

Sensitive high-resolution ion microprobe (SHRIMP) analyses yielded metamorphic U-Pb zircon ages of 550 – 520 Ma (Shiraishi et al. 2003), and electron microprobe U-Th-Pb monazite dating from Skallen showed an age of 560 – 500 Ma (Hokada and Motoyoshi, 2006). Kawakami et al. (2016) obtained older age population of 650 – 580 Ma and younger age population of 560 – 550 Ma from garnet-sillimanite gneiss from Skallevikshalsen using electron microprobe U-Th-Pb dating of monazite and LA-ICP-MS U-Pb dating of zircon, and hence they proposed polymetamorphism. Takahashi et al. (2018) divided the LHC into southern LHC (ca. 2.5 Ga, also called as Shirase microcontinent), central LHC (ca. 1.8 Ga), and northern LHC (ca. 1.0 Ga) based on protolith ages obtained from zircon cores in orthogneisses.

2.4. Geology of Exposures Focused in This Study

2.4.1. Niban Rock

Niban rock is a 2.5 km x 3.5 km exposure located in amphibolite-facies zone of the LHC (Fig. 2-2). It is located at about 15 km to the southwest of Cape Hinode. Niban Rock is

underlain mainly by sillimanite-garnet-biotite gneiss, biotite gneiss, and biotite-hornblende gneiss with minor metabasite, calc-silicate gneiss, granite, and aplite (Kizaki et al., 1983) (Fig. 2-3). P-T condition of Niban rock is previously reported as 700 °C, 6.66 kbar by Hiroi et al. (1983) (Fig. 2-4). Dunkley et al. (2014) reported 1.1 – 0.9 Ga of xenocryst age, 551 ± 11 Ma of protolith age, and 532 ± 7 Ma from metagranitic dyke.

2.4.2. Akarui Point

Akarui Point is an exposure located in the transitional zone (Fig. 2-2). It is underlain mainly by garnet-biotite, biotite-hornblende, and hornblende–biotite gneisses with minor metabasites (Yanai et al., 1984) (Fig. 2-5). The peak P-T conditions for Akarui Point are estimated as follows: 770 – 980 MPa, 770 – 790 °C using the garnet-biotite geothermometers and garnet-sillimanite-quartz-plagioclase geobarometers for the silimanite-biotite-garnet gneiss (Kawakami et al., 2008), 825 – 900 °C using the ternary-feldspar geothermometry for the same gneiss as Kawakami et al. (2008) (Nakamura et al., 2014), 500 – 600 MPa, 900 – 920 °C based on the pseudosection combined with the orthopyroxene-spinel geothermometry for the mafic granulite (Iwamura et al., 2013), prograde temperature of 764 – 844 °C (assuming 0 – 14 kbar) and retrograde temperature of 773 – 828 °C (sillimanite stability field) based on Zr-in-rutile geothermometry (Suzuki & Kawakami, 2019) (Fig. 2-4). Iwamura et al. (2013) proposed the clockwise P-T path for Akarui Point as 1100 – 1200 MPa at ~ 900 °C for the prograde condition and 500 – 600 MPa at 90 – 920 °C for the peak condition (Fig. 2-4).

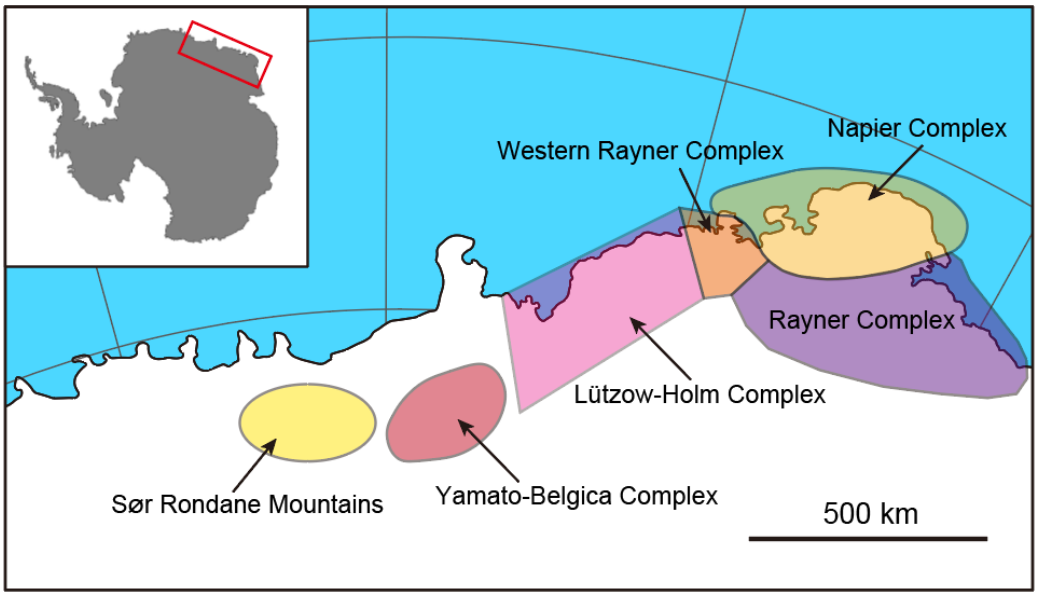

Figure 2-1. Position of complexes in eastern Dronning Maud Land, East Antarctica.

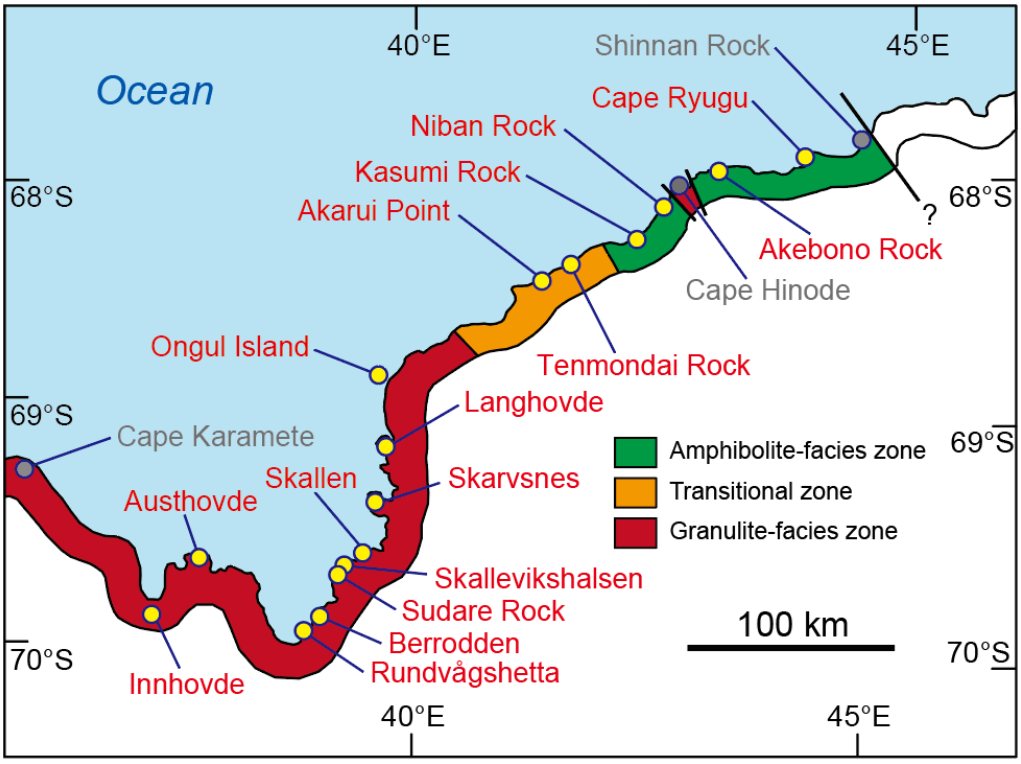

Figure 2-2. Metamorphic zonation of the LHC and position of exposures. Names of exposures dealt in this study is colored in red. Metamorphic zonation is after Hiroi et al. (1991).

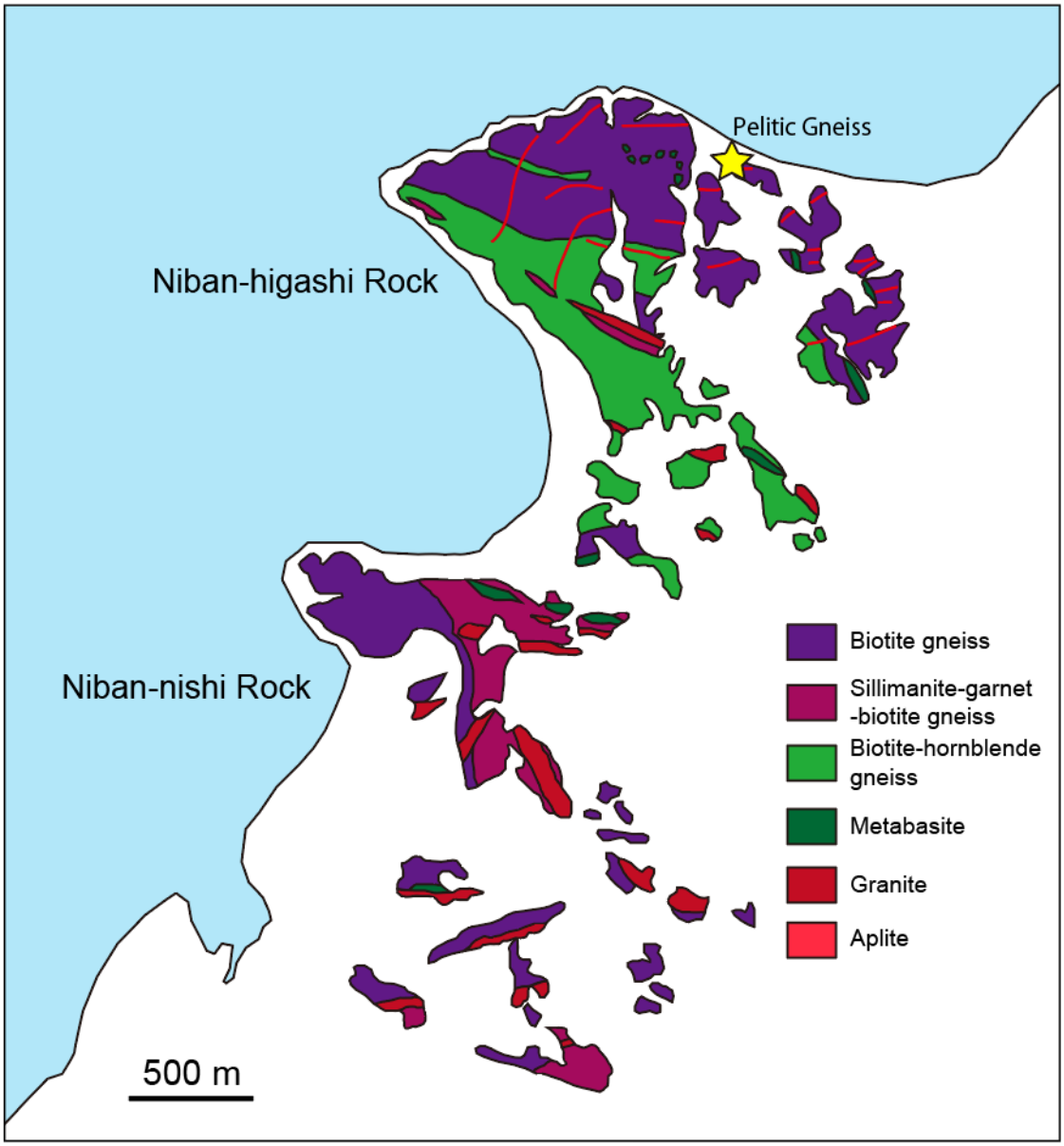

Figure 2-3. Geological Map of Niban Rock (after Kizaki et al., 1983).

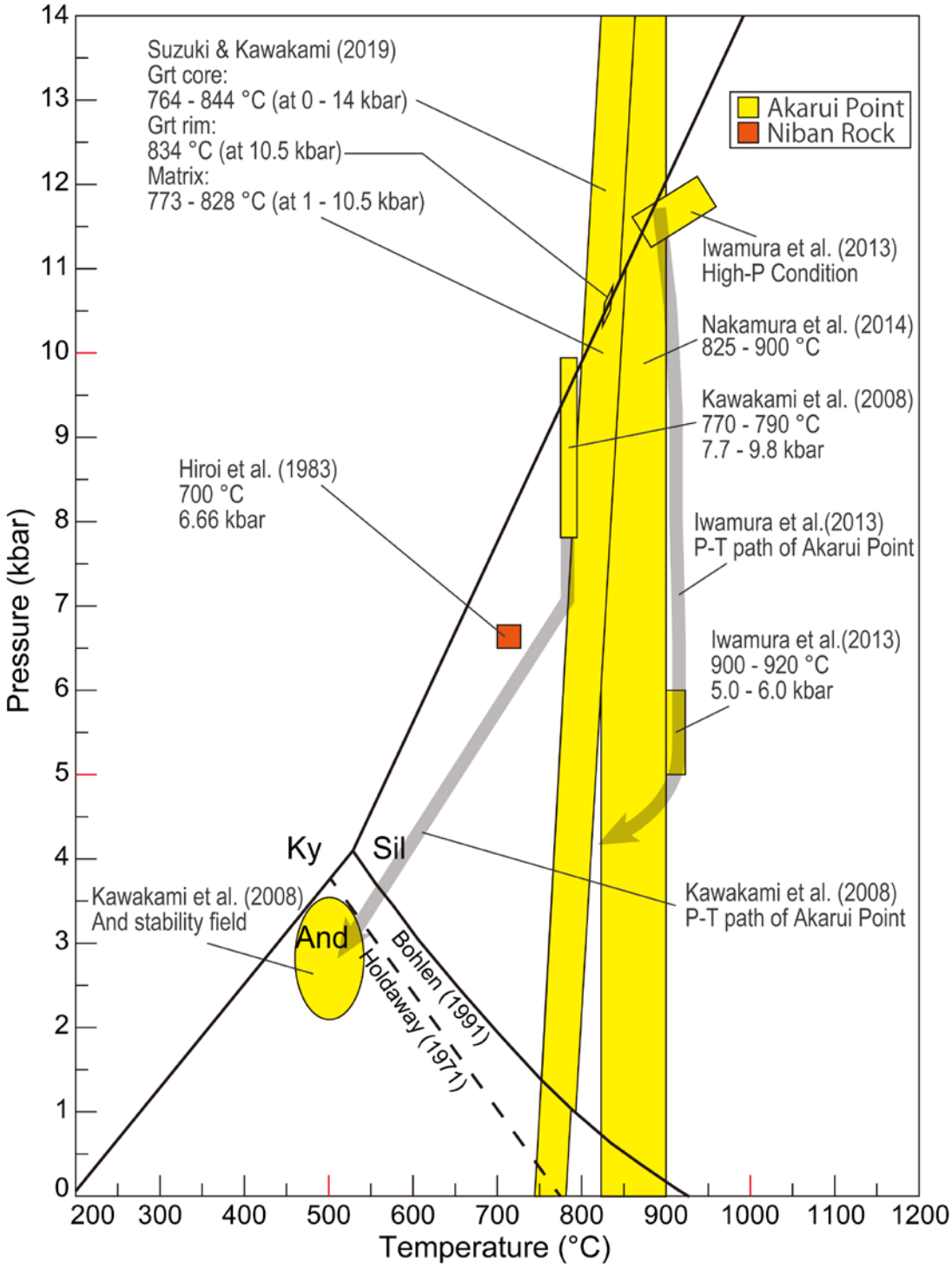

Figure 2-4. P-T conditions of Niban Rock (orange square) and Akarui Point (yellow square) reported in previous studies. Triple points of aluminosilicates are after Holdaway (1971) and Bohlen (1991).

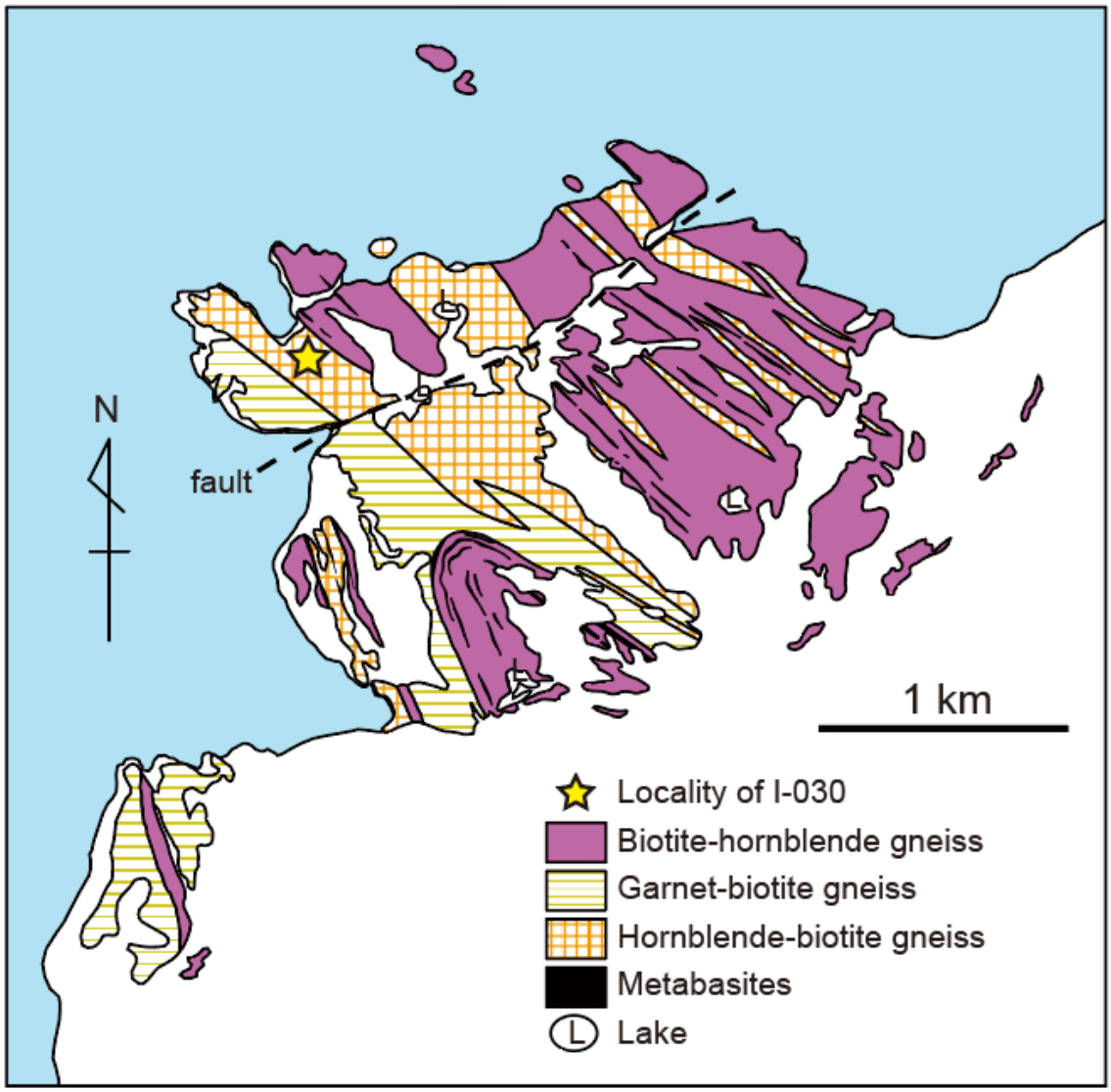

Figure 2-5. Geological Map of Akarui Point (after Yanai et al., 1984)

3. ANALYTICAL METHODS

3.1. Mineral Chemistry

Mineral chemistry was investigated using a JEOL JXA-8530F field emission electron probe microanalyzer equipped with wavelength dispersive X–ray spectrometers at Kyushu University, Japan. Carbon coated thin sections were used for the mineral chemical analyses. Natural and synthetic materials were used for standards. The ZAF method was applied for data correction using a software supplied by JEOL Ltd.

The quantitative analyses of major components in the constituent minerals were carried out using an accelerating voltage of 15 kV and a beam current of 5 or 10 nA with a probe diameter of 2 – 6 μm. The counting times for the peak and backgrounds were 10 sec and 5 sec, respectively. In some analyses, the counting time for the peak and backgrounds was 30 sec and 15 sec for Cl, 60 sec and 30 sec for F, and 10 sec and 5 sec for other elements to reduce counting error. In apatite analyses, an accelerating voltage of 15 kV and a beam current of 5 nA were used to reduce beam damage. Counting times for the peak and backgrounds were 10 sec and 5 sec for all elements, respectively.

The quantitative analyses of Zr in rutile were carried out using an accelerating voltage of 20 kV and a beam current of 150 nA with a probe diameter of 1 – 3 μm. The counting times of Zr for the peak and backgrounds were 300 and 150 sec, respectively. The counting error of Zr was 3.38 % (1σ level at 364 ppm), which is considered to small enough for the application for Zr-in-rutile geothermometry because the error provides only about ±3 °C. Si, Ti, Al, Cr, V, Fe, Nb were quantified in addition to Zr (cf. Zack et al., 2004). The results with Si < 200 ppm and Nb < 17000 ppm were adopted for the Zr-

in-rutile geothermometer according to the recommendation by Zack et al. (2004).

The analytical conditions for X-ray mapping of garnet grains except for P, Y, and Cr were 15 kV acceleration voltage, 80 – 100 nA probe current with 5 – 12 μm beam diameter, and 20 – 25 msec dwell time per pixel. That for P, Y, and Cr in garnet was 15 kV accelerating voltage, 500 nA probe current with 5 – 12 μm beam diameter, and 150 – 200 msec dwell time per pixel.

3.2. Whole-rock Chemistry

The rock sample utilized for X-ray fluorescence (XRF) analysis was powdered in a tungsten-carbide mill at Kyushu University. Loss on ignition was measured for powdered rock samples after heating at 1000 °C for 6 hours using an electric furnace. A 1:5 weight ratio of powdered rock sample and anhydrous dilithium tetraborate flux was fused to prepare a glass bead. Major and minor element compositions of whole rock samples were determined by X-ray fluorescence spectrometry (Rigaku-ZSX Primus IV) at Kyushu University applying calibration technique using glass discs described in Nakada (1985) and Nakada et al. (1985).

3.3. Raman Spectroscopy

Minerals were identified using a laser Raman spectrometer (STR laser micro-Raman spectroscopy system, Seki Technotron Corporation) at Kyushu University. The instrument was equipped with a 532 nm Nd–YAG laser, a charge coupled device (CCD) detector cooled by a Peltier element, and an automated confocal microscope (Nikon). The

objective was a Nikon 100X lens with a numerical aperture of 0.9. The laser had a maximum power of 50 mW. The spectral range with a grating of 1800 lines per mm. The spectrometer was calibrated using silicon wafer (520.5 cm^{-1}) and sulfur (219.1 and 473.2 cm^{-1}). The room temperature was maintained at 22 ± 1 °C.

4. RESULTS

4.1. Sample Description

4.1.1. Mafic Gneisses

In this section, I describe all mafic gneisses dealt in this study. Coronal mineral assemblages are also summarized in Table 4-1. A mafic gneiss (I-030) from Akarui Point and a pelitic gneiss from Niban Rock will be described in later sections.

Cape Ryugu

Sample No. YN78010312 (Corona free) (Fig. 4-1)

This gneiss is composed mainly of garnet, hornblende, biotite, plagioclase, and quartz with minor amounts of ilmenite. Garnet in the gneiss does not have corona and directly contacts with hornblende, biotite, quartz, or plagioclase. Garnet shows irregular shape (up to about 5 mm). Matrix hornblende, plagioclase, biotite, and quartz are elongated (about 0.6 mm long), and they define the gneissosity.

Akebono Rock

Sample No. YH81012016 (Corona free) (Fig. 4-2)

This gneiss is composed mainly of garnet, hornblende, biotite, plagioclase, and quartz with minor amounts of ilmenite. The large garnet porphyroblast (2 cm in diameter) is a

character of this sample. Garnet in the gneiss does not have corona and directly contacts with hornblende, biotite, quartz, or plagioclase. Matrix hornblende, plagioclase, and quartz are elongated (about 0.5 mm long), and they define the gneissosity. Ilmenite exsolution is present in the matrix hornblende.

Niban Rock

Sample No. TM11020803A (Corona free) (Fig. 4-3)

The constituent minerals of this mafic gneiss are garnet, hornblende, quartz, plagioclase, biotite, and ilmenite. Garnet in the gneiss does not have corona and is in directly contact with hornblende, biotite, quartz, or plagioclase. Garnet shows irregular to rounded shape (up to about 5 mm). Matrix hornblende, plagioclase, and quartz are slightly elongated (1 mm long), and they define the gneissosity.

Kasumi Rock

Sample No. I-554 (Corona free) (Fig. 4-4)

The constituent minerals of this mafic gneiss are garnet, hornblende, quartz, plagioclase, biotite, and ilmenite. Garnet in the gneiss does not have corona. Garnet shows irregular shape (up to about 5 mm). Area around garnet is mostly occupied by plagioclase, and garnet is partially in contact with hornblende directly. The matrix is composed mainly of polygonal plagioclase and anhedral hornblende with minor amounts of biotite and ilmenite.

Tenmondai Rock

Sample No. TM11021006A (Corona free) (Fig. 4-5)

The constituent minerals of this mafic gneiss are garnet, hornblende, quartz, plagioclase, biotite, and ilmenite. Garnet in the gneiss does not have corona. This sample is composed of two domains of garnet- or plagioclase-rich domain and hornblende-rich domain. In garnet- or plagioclase-rich domain, garnet, hornblende, quartz, and plagioclase are equigranular (0.8 – 1.0 mm in diameter). Hornblende in hornblende-rich domain is coarser than that in the garnet- or plagioclase-rich domain (up to 1.5 mm). Hornblende shows pleochroism from dark brownish-green to brownish-yellow. Biotite shows pleochroism from brown to pale brownish-yellow.

Akarui Point

Sample No. I-008 (Corona bearing) (Fig. 4-6)

This sample is composed mainly of garnet and hornblende with minor amounts of plagioclase, spinel, and sapphirine. The garnet is surrounded symplectitic corona of orthopyroxene + plagioclase + spinel. Hornblende shows pleochroism from bluish-green to pale greenish-yellow. A small amount of retrograde gedrite is locally present in the corona. Numerous tiny rounded to polygonal grains of hornblende are included in garnet. Matrix sapphirine is often associated with spinel.

East Ongul Island

Sample No. I-518 (Corona bearing) (Fig. 4-7)

This gneiss is composed mainly of garnet, hornblende, plagioclase, and biotite with a minor amount of orthopyroxene. Garnet is large as about 2 cm in diameter and is surrounded by biotite + plagioclase corona. The rim of garnet locally shows concavo-convex shape. Hornblende and plagioclase with minor amounts of biotite and orthopyroxene consist matrix. Hornblende and plagioclase show polygonal to slightly rounded shape. Biotite composing corona is green, whereas that in matrix is brown.

Langhovde

Sample No. TM11021501E (Corona free) (Fig. 4-8)

This sample is composed mainly of garnet, hornblende, biotite, and plagioclase. Garnet in the gneiss does not have corona. Garnet (about 1 mm) is irregular shape. Hornblende (about 0.7 – 1 mm) shows pleochroism from dark drownish-green to greenish-yellow. Plagioclase (about 0.7 mm) is polygonal shape, while hornblende is irregular shape. Biotite (about 1mm) shows pleochroism from dark drownish-green to greenish-yellow.

Skarvsnes

Sample No. 92010203A (Corona free) (Fig. 4-9)

This sample is composed mainly of garnet, hornblende, clinopyroxene, and plagioclase. Garnet in the gneiss does not have corona. Garnet (about 2 - 10 mm) and clinopyroxene (about 1 mm) show irregular shape. Most plagioclase broke down into mineral aggregate (unidentified). Hornblende (about 0.7 – 1 mm) shows pleochroism from dark drownish-

green to greenish-yellow.

Skallen

Sample No. I-232 (Corona free) (Fig. 4-10)

This gneiss is composed mainly of garnet, hornblende, plagioclase, clinopyroxene, and orthopyroxene. Garnet in the gneiss does not have corona. The garnet grain is coarse (10 mm long) and elongated. The garnet and the hornblende define gneissosity of the rock. The hornblende is brown to pale brown.

Sample No. I-223 (Corona bearing) (Fig. 4-11)

This gneiss is composed mainly of garnet, hornblende, plagioclase, clinopyroxene, orthopyroxene, and biotite. The garnet grains are coarse (15 mm in diameter) and surrounded by the symplectitic coronas composed of orthopyroxene and plagioclase. The most periphery of the garnet contacts to the corona except for some parts which contact to the hornblende grains and the coarse-grained plagioclase directly. The garnet grain includes felsite-nanogranite inclusion (about 150 μm) composed of quartz, biotite, plagioclase, and K-feldspar (Fig. 4-12). The matrix is composed mainly of hornblende, plagioclase, clinopyroxene, and orthopyroxene with minor amounts of biotite and magnetite. The matrix hornblende is brown to brownish-green. The matrix plagioclase often exhibits antiparthite texture, and K-feldspar occurs as antiparthite only. The grains of clinopyroxene have thin lamellae and are usually rimmed by orthopyroxene. The clinopyroxene exhibits pleochroism from bluish-green to brownish-green. Both the coronal and matrix orthopyroxene show pale red to pale green.

Skallevikshalsen

Sample No. I-293 (Corona bearing) (Fig. 4-13)

The gneiss is composed mainly of garnet, plagioclase, hornblende, clinopyroxene, orthopyroxene, and biotite. Quartz + plagioclase vein is present. Garnet is surrounded by orthopyroxene + plagioclase corona and contains FNIs (about 50 μm) (Fig. 4-14). Clinopyroxene, orthopyroxene, plagioclase, and hornblende are equigranular.

Sudare Rock

Sample No. TM11010503E (Corona bearing) (Fig. 4-15)

The gneiss is composed mainly of garnet, biotite, plagioclase, hornblende, and orthopyroxene. Garnet (2 mm) is irregular shape. The garnet is partially rimmed by corona of orthopyroxene + plagioclase. Hornblende (0.7 mm) shows pleochroism from dark green to brownish-green. Biotite (2 mm) shows pleochroism from reddish-brown to pale brown. Orthopyroxene (0.7 mm) shows pleochroism from pale red to pale bluish-green.

Berrodden

Sample No. 93012101C (Corona bearing) (Fig. 4-16)

The gneiss is composed mainly of garnet, plagioclase, hornblende, biotite, orthopyroxene, and clinopyroxene. Those in matrix are relatively fine (0.3 mm). Garnet is partially

surrounded by symplectitic corona of orthopyroxene + plagioclase.

Rundvågshetta

Sample No. I-122 (Corona bearing) (Fig. 4-17)

The studied gneiss is composed mainly of hornblende, garnet, and plagioclase. The garnet grains (5 mm in diameter) are mostly surrounded by the symplectitic coronas composed of orthopyroxene (pale green to pale red), plagioclase, and magnetite. Some parts of the periphery of the garnet grains contact with the matrix hornblende or plagioclase directly without the corona. The matrix is composed mainly of equigranular hornblende and plagioclase (2-4 mm in diameter) with a minor amount of biotite (1-2 mm long). The hornblende exhibits pleochroism from brownish-green to light brown. Biotite is brown to light brown. Some grains of the matrix plagioclase show albite twinning.

Sample No. 93010701C (Corona bearing) (Fig. 4-18)

The studied gneiss is composed mainly of garnet, hornblende, plagioclase, orthopyroxene, magnetite and spinel. The matrix is composed mainly of equigranular hornblende and plagioclase (2 – 4 mm in diameter) or plagioclase, magnetite, and spinel. Garnet (2 – 3 mm) occurs in coarse-grained plagioclase-rich domain. The garnet shows irregular shape. Symplectitic orthopyroxene + plagioclase + spinel develops between garnet and hornblende, but most part of garnet rim are directly in contact with coarse-grained plagioclase.

Austhovde

Sample No. 93012301C (Corona free) (Fig. 4-19)

The studied gneiss is composed mainly of garnet, hornblende, clinopyroxene, plagioclase, and ilmenite. Garnet in the gneiss does not have corona. The matrix hornblende and clinopyroxene are polygonal shape and equigranular (about 0.8 mm). The matrix plagioclase is small (about 0.3 mm).

Sample No. 93012411B (Corona bearing) (Fig. 4-20)

The studied gneiss is composed mainly of garnet, plagioclase, clinopyroxene, orthopyroxene, hornblende, magnetite, and ilmenite. Garnet shows irregular shape and is surrounded by symplectitic corona of orthopyroxene + plagioclase + magnetite. The matrix clinopyroxene is polygonal shape. The matrix hornblende is smaller than the matrix clinopyroxene.

Sample No. 93012301B (Corona bearing, with matrix quartz) (Fig. 4-21)

The studied gneiss is composed mainly of garnet, hornblende, biotite, plagioclase, orthopyroxene, clinopyroxene, quartz with minor amounts of ilmenite, K-feldspar, and apatite. Plagioclase in the matrix shows antiperthite. Garnet is surrounded by symplectic corona composed of plagioclase and orthopyroxene with a minor amount of calcic amphibole. K-feldspar occurs as only antiparthite of the matrix plagioclase.

Innhovde

Sample No. 84011107(T) (Corona bearing) (Fig. 4-22)

This gneiss is composed mainly of garnet, clinopyroxene, orthopyroxene, plagioclase, and ilmenite. The garnet (2 mm in diameter) is surrounded by symplectitic corona of orthopyroxene + plagioclase + clinopyroxene. The matrix minerals are polygonal shape and equigranular (about 0.5 mm).

Table 4-1. Summary of occurrence of coronas found in this study

Exposure	Sample No.	Coronal Mineral Assemblage
Akarui Point	I-008	Opx + Pl + Spl
Akarui Point	I-030	Ged + Pl
East Ongul Island	I-518	Bt + Pl
Skallen	I-223	Opx + Pl ± Mgt
Skallevikshalsen	I-293	Opx + Pl
Sudare Rock	TM11010503E	Opx + Pl
Berrodden	93012101C	Opx + Pl
Rundvågshetta	I-122	Opx + Pl + Mgt
Rundvågshetta	93010701C	Opx + Pl + Spl
Austhovde	93012301B	Opx + Pl ± Amp
Austhovde	93012411B	Opx + Pl ± Mgt
Innhovde	84011107(T)	Opx + Pl ± Cpx ± Amp

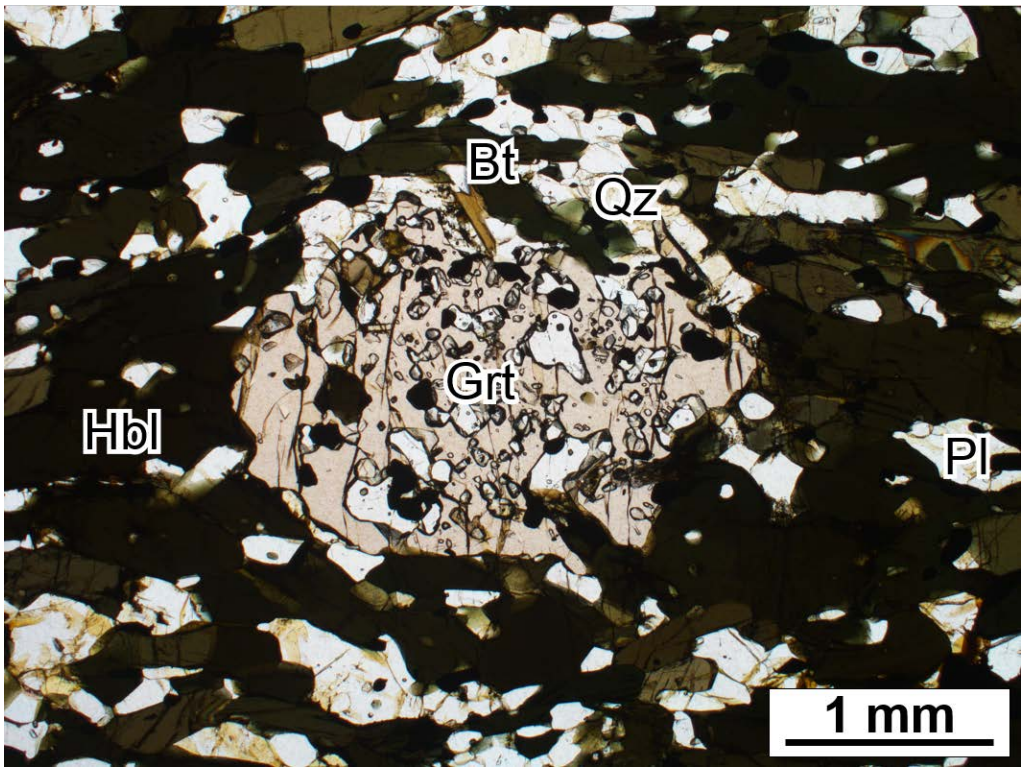

Figure 4-1. Photomicrograph of representative texture of sample YN78010312 from Cape Ryugu.

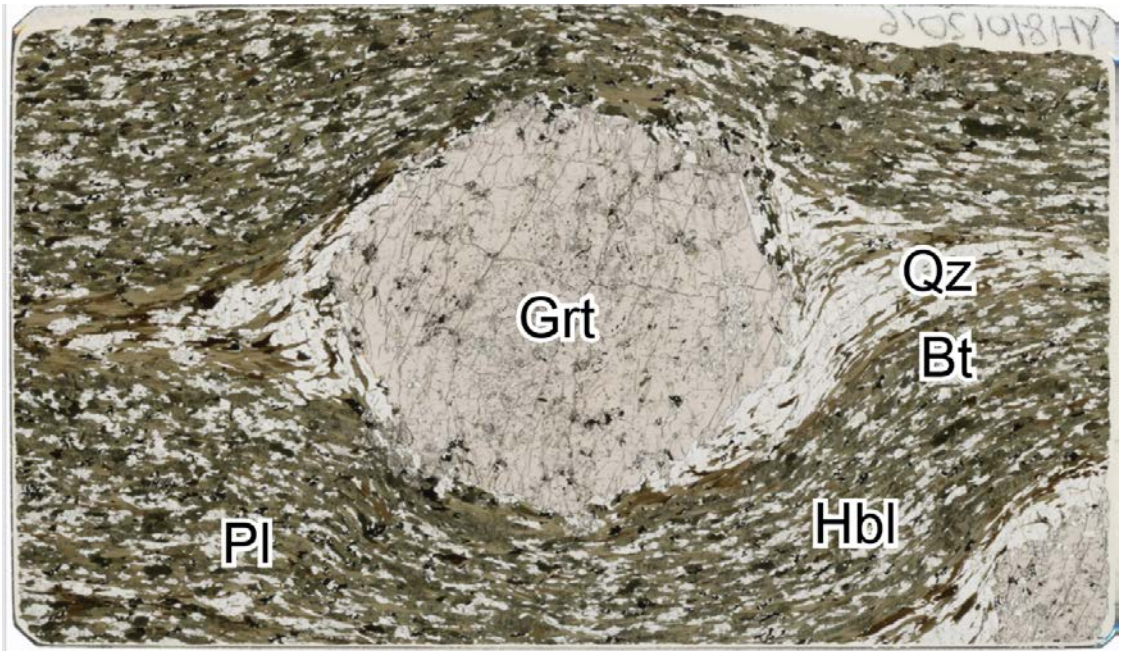

Figure 4-2. Photograph of thin section showing representative texture of sample YH81012016 from Akebono Rock (4.8 cm in width).

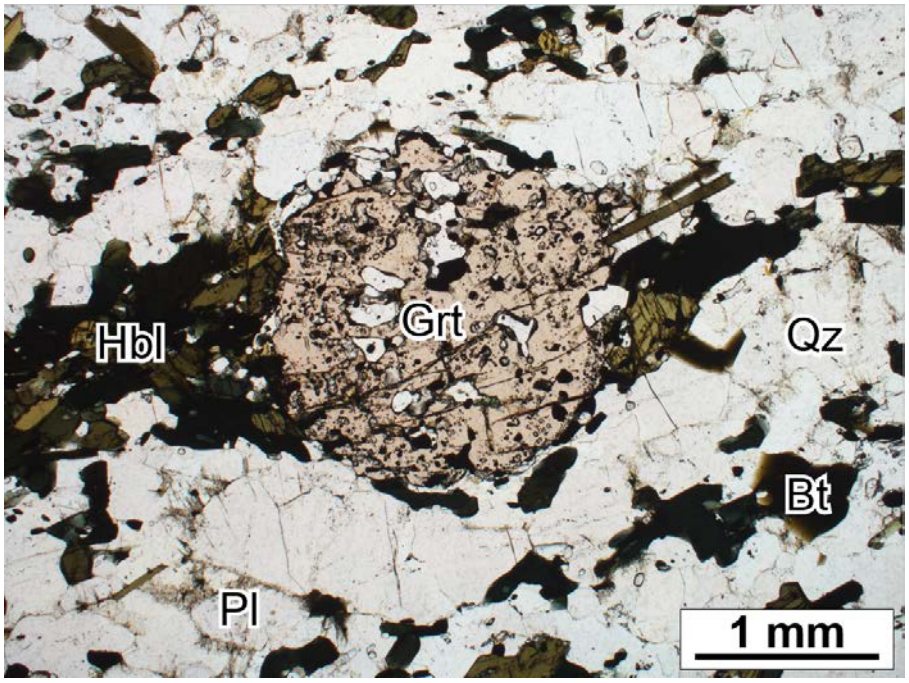

Figure 4-3. Photomicrograph of representative texture of sample TM11020803A from Niban Rock.

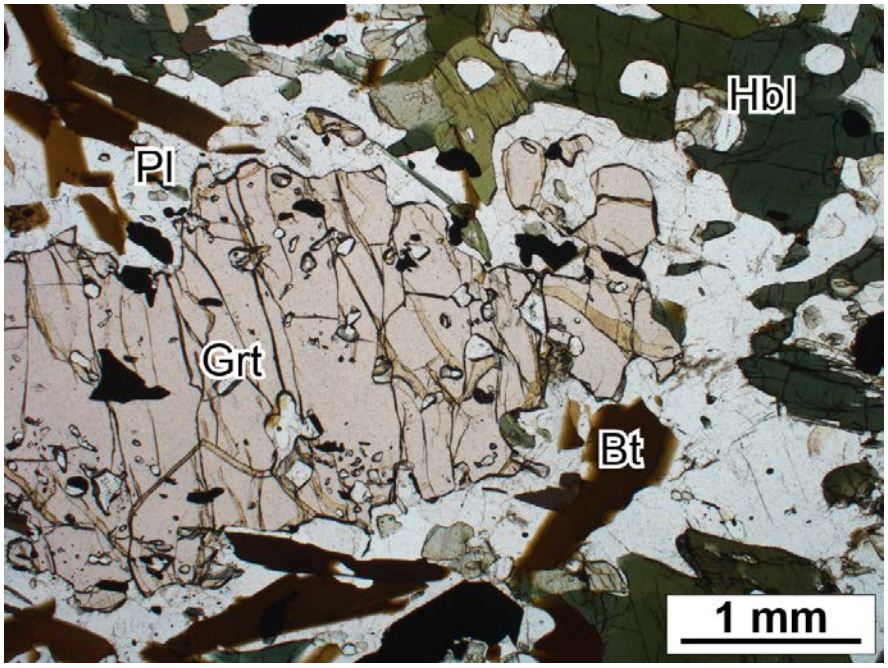

Figure 4-4. Photomicrograph of representative texture of sample I-554 from Kasumi Rock.

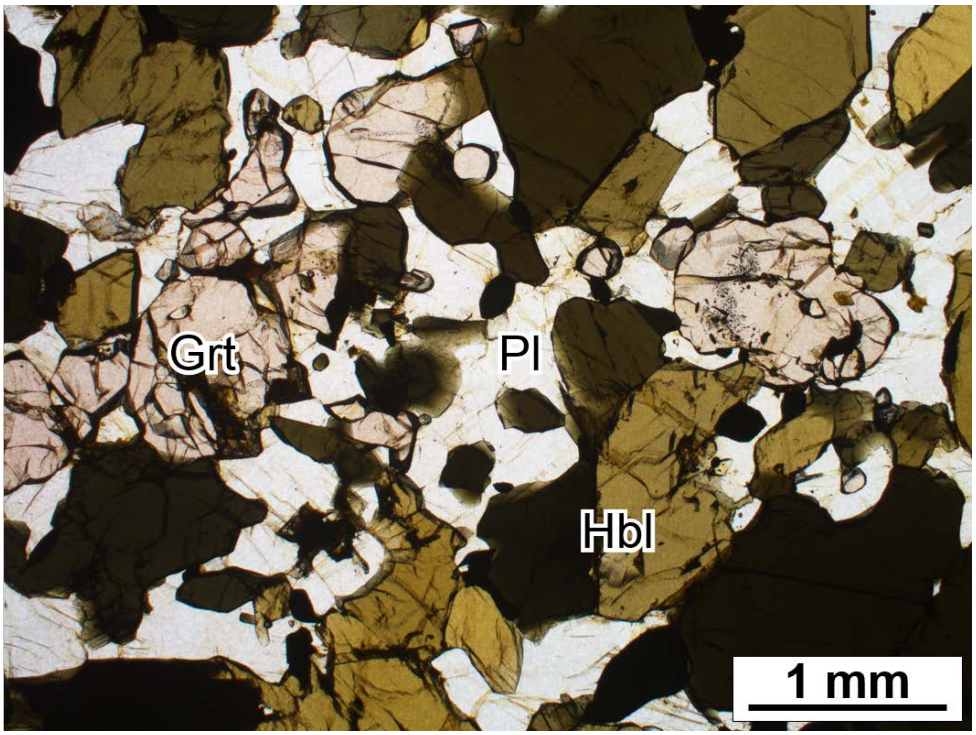

Figure 4-5. Photomicrograph of representative texture of sample TM11021006A from Tenmondai Rock.

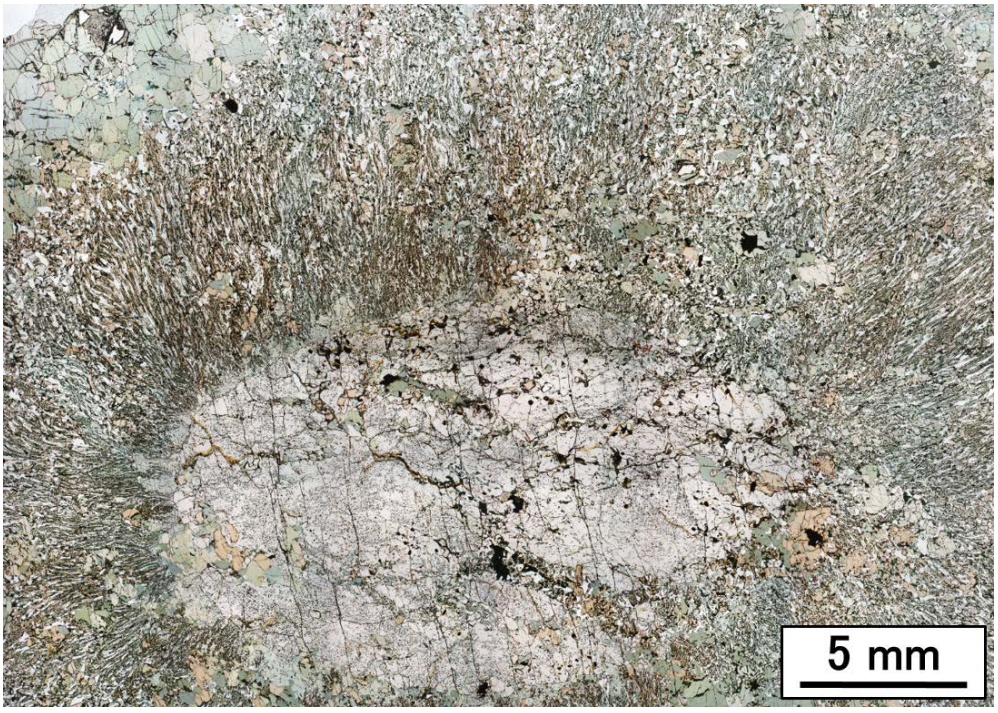

Figure 4-6. Photomicrograph of representative texture of sample from I-008 Akarui Point.

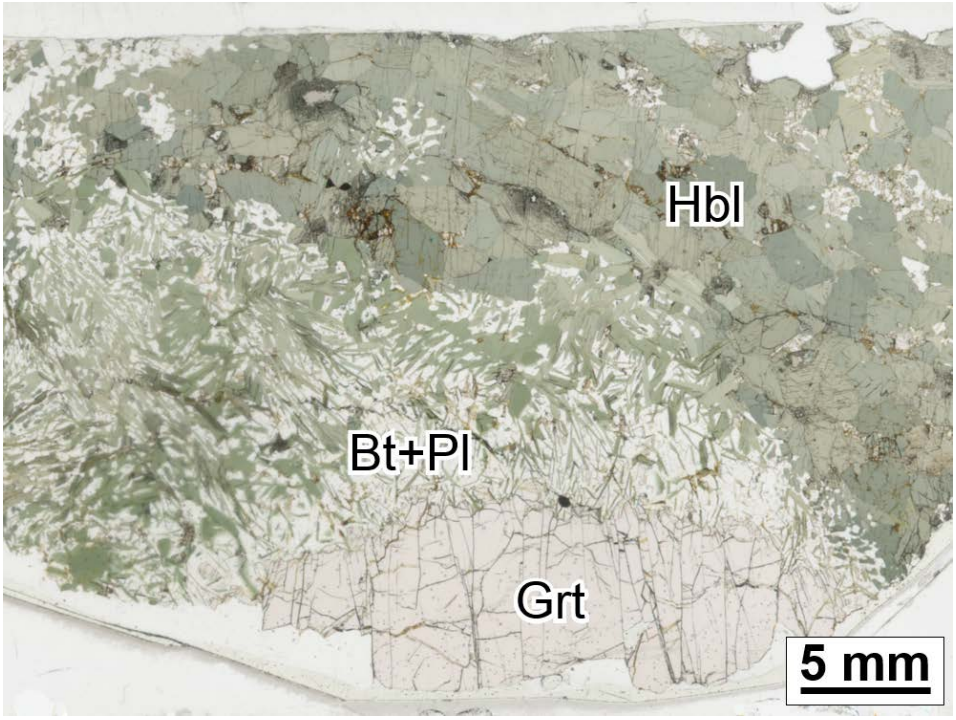

Figure 4-7. Photograph of thin section showing representative texture of sample I-518 from East Ongul Island.

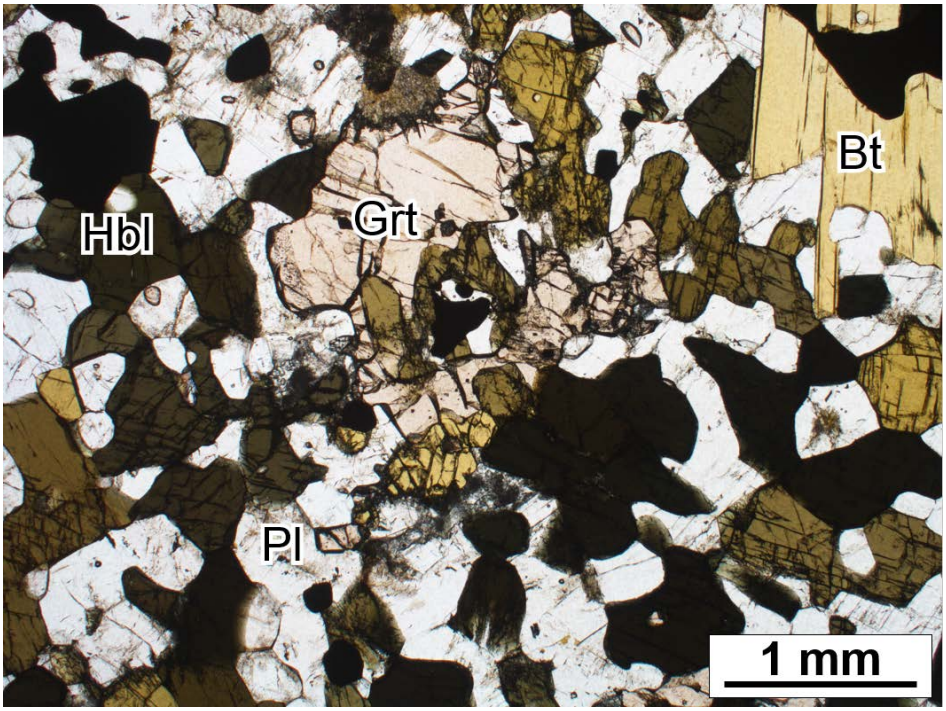

Figure 4-8. Photomicrograph of representative texture of sample TM11021501E from Langhovde.

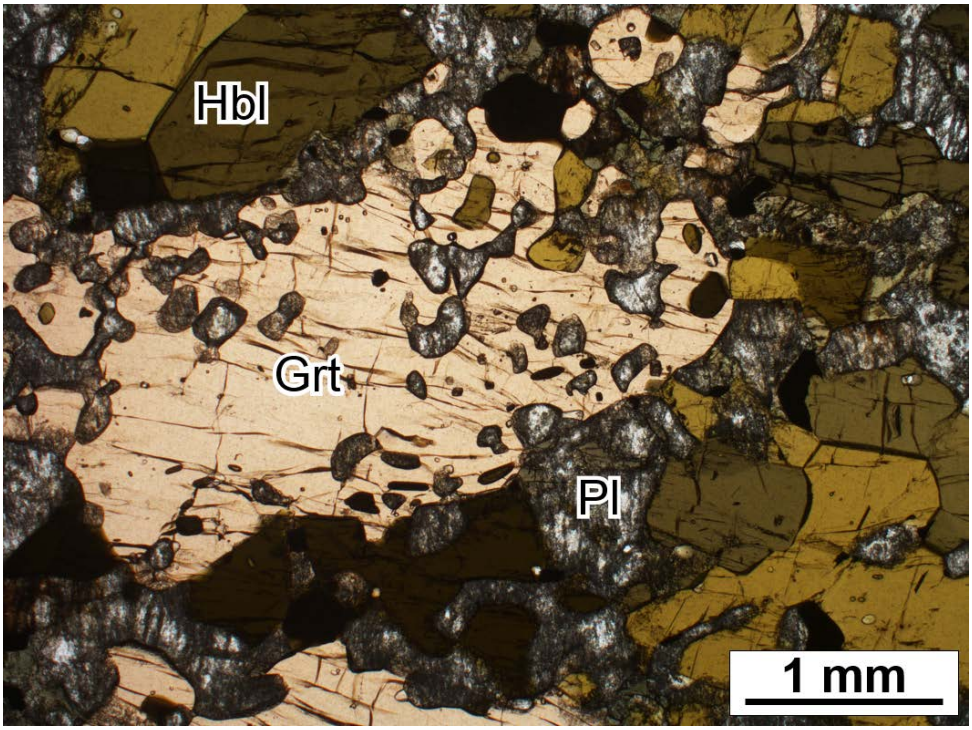

Figure 4-9. Photomicrograph of representative texture of sample 92010203A from Skarvsnes.

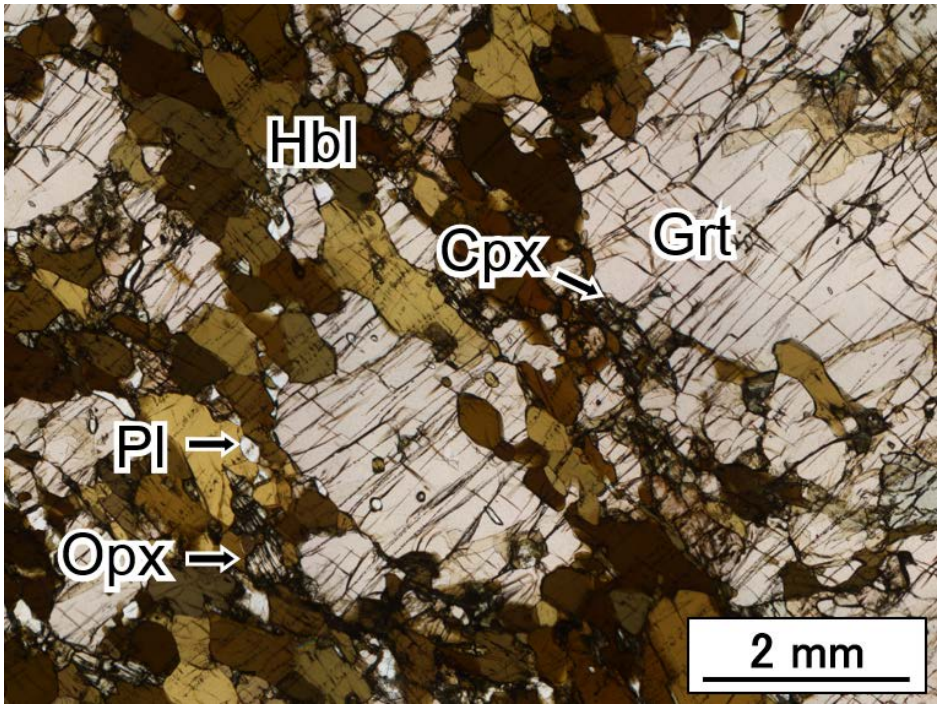

Figure 4-10. Photomicrograph of representative texture of sample I-232 from Skallen.

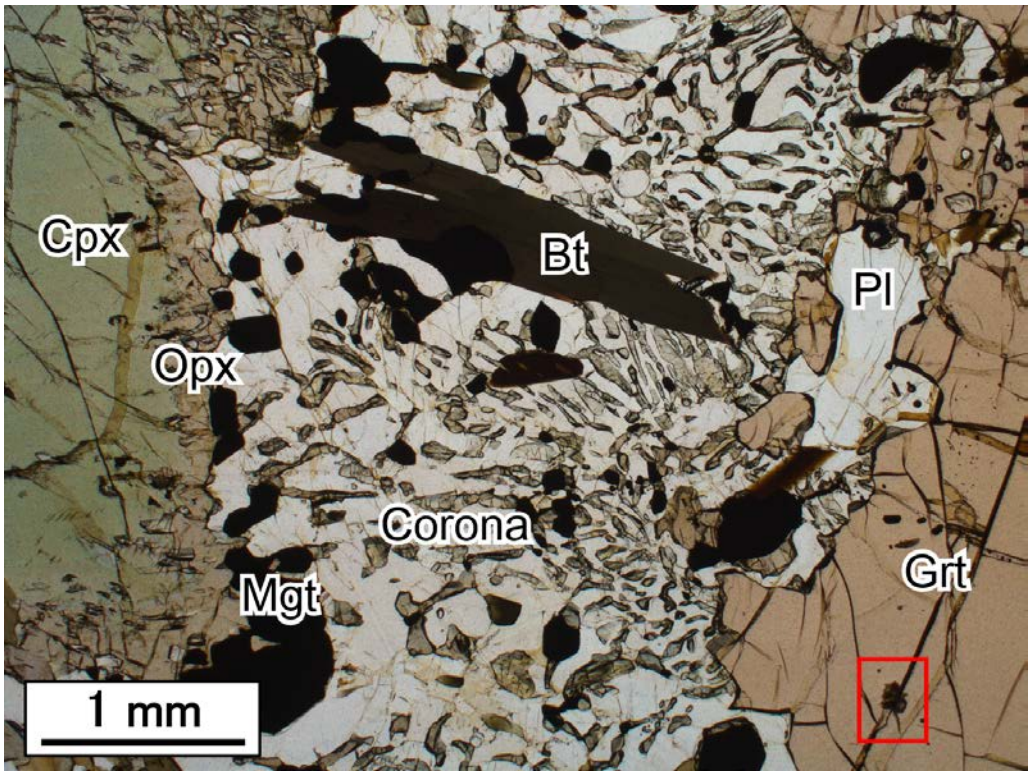

Figure 4-11. Photomicrograph of representative texture of sample I-223 from Skallen.

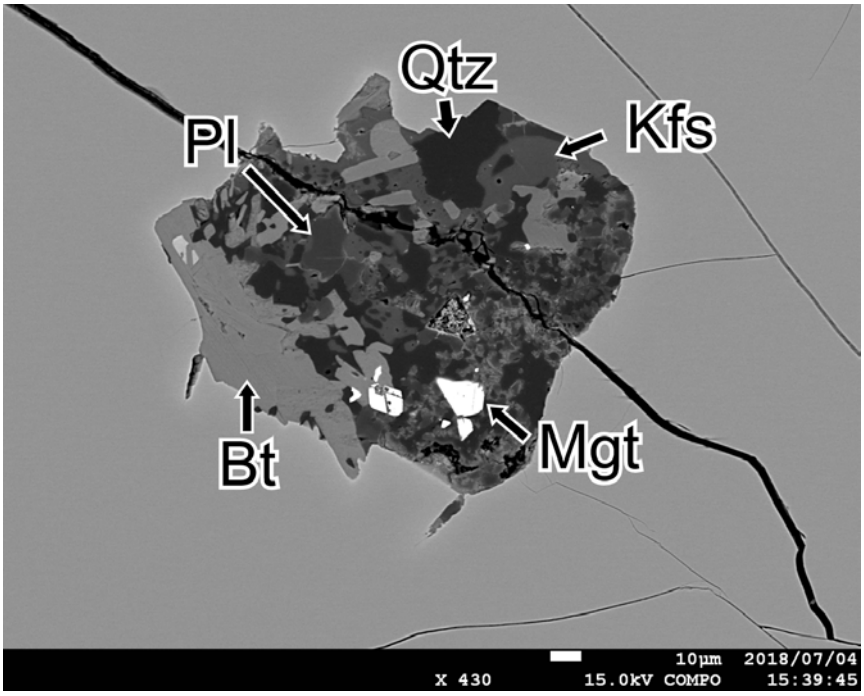

Figure 4-12. BSE image showing texture of felsite-nanogranite inclusion in garnet in I-223 from Skallen.

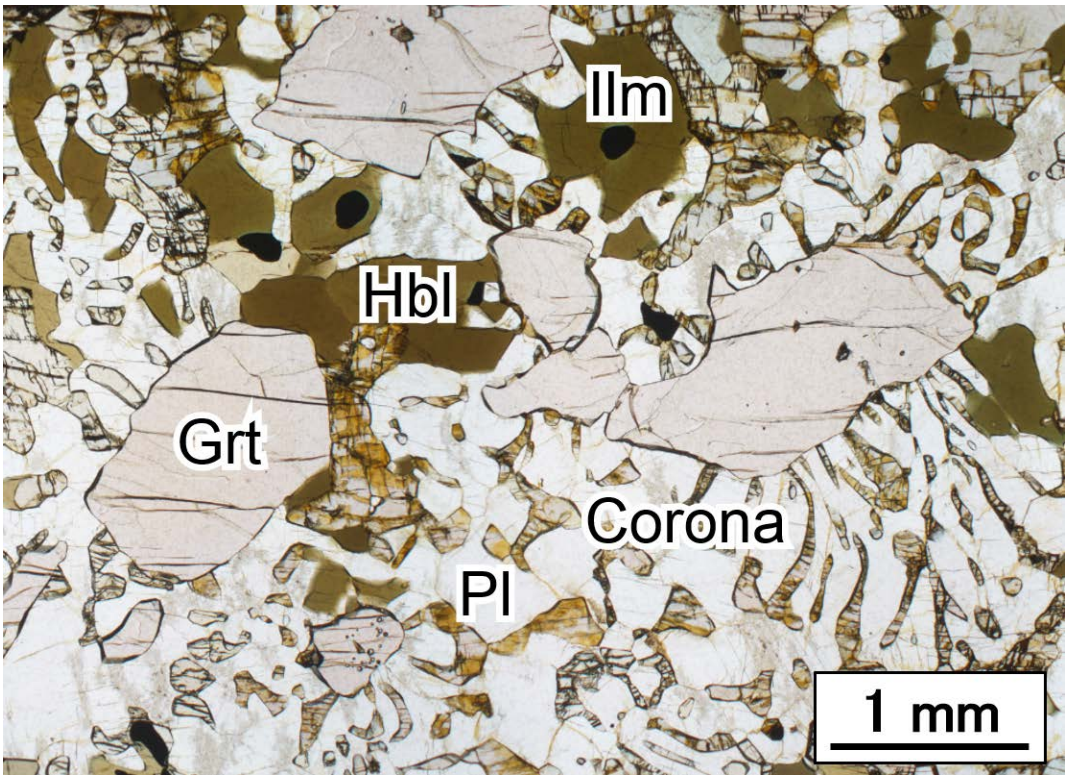

Figure 4-13. Photomicrograph of representative texture of sample I-293 from Skallevikshalsen.

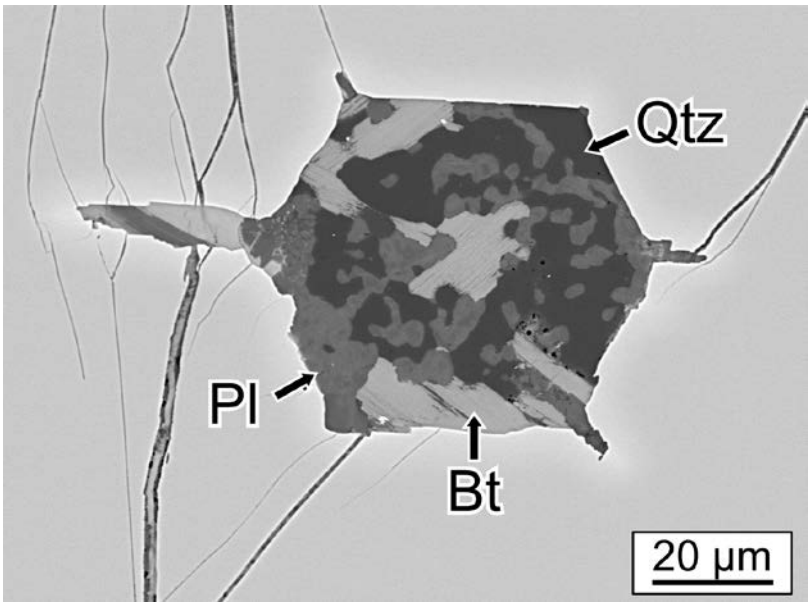

Figure 4-14. BSE image showing texture of felsite-nanogranite inclusion in I-293 from Skallevikshalsen.

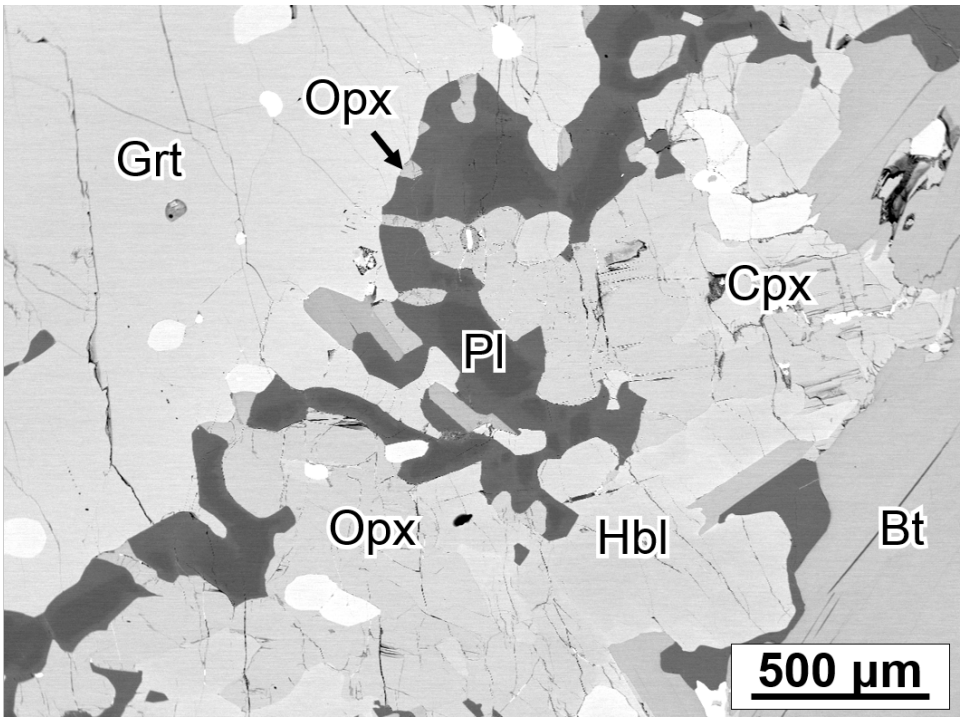

Figure 4-15. BSE image of representative texture of sample TM11010503E from Sudare Rock.

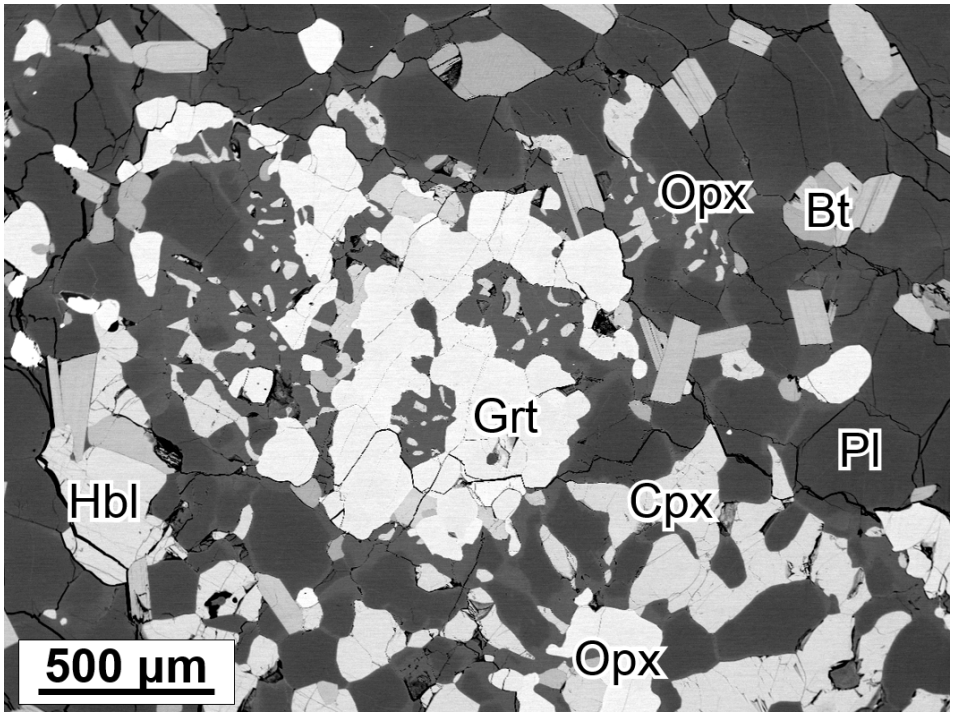

Figure 4-16. BSE image of representative texture of sample 93012101C from Berrodden.

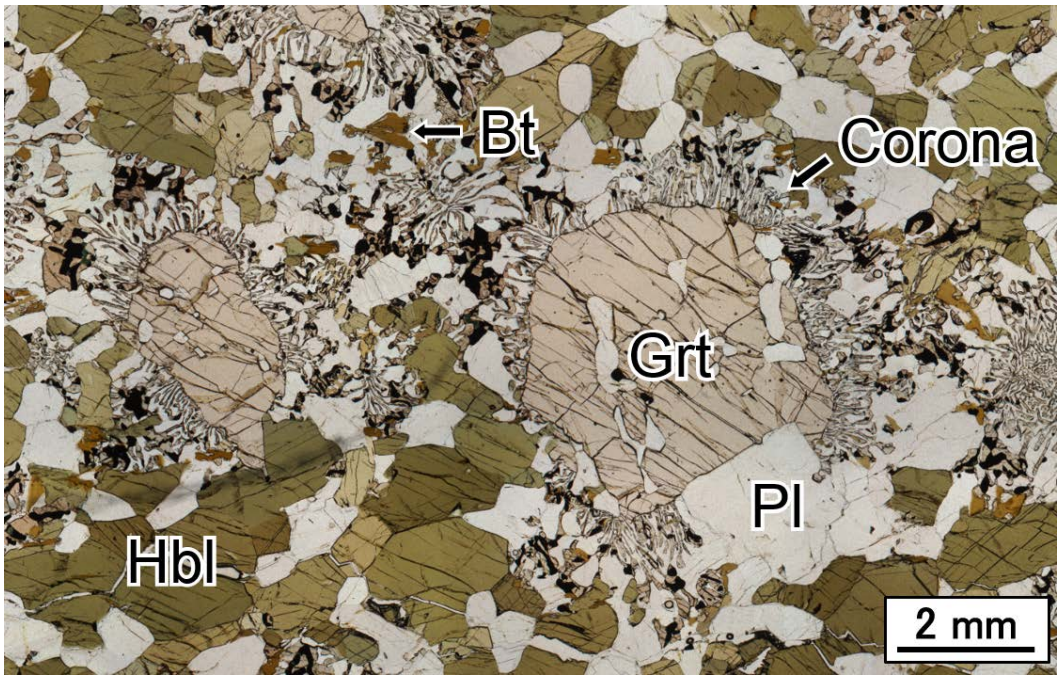

Figure 4-17. Photomicrograph of representative texture of sample I-122 from Rundvågshetta. Matrix hornblende is directly in contact with garnet in part.

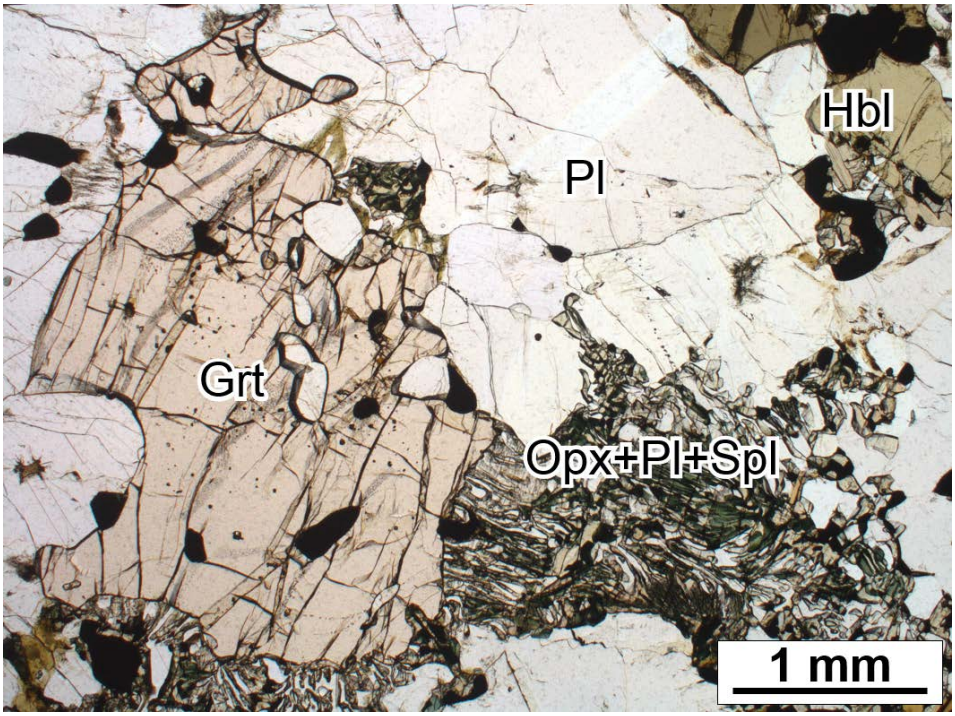

Figure 4-18. Photomicrograph of representative texture of sample 93010701C from Rundvågshetta.

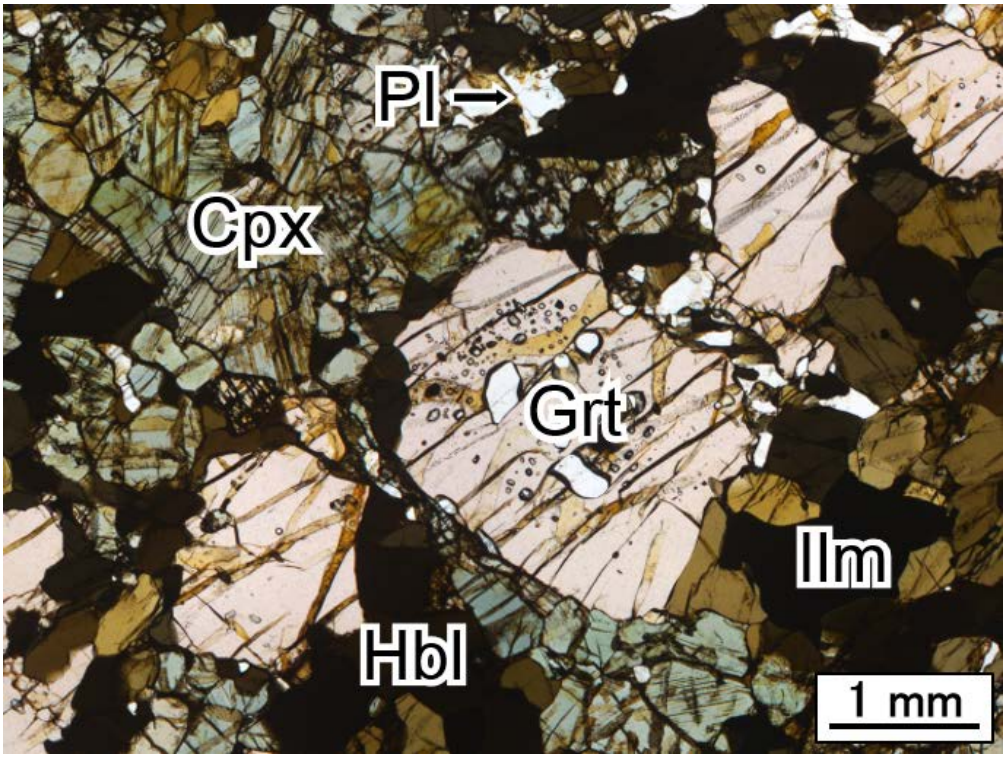

Figure 4-19. Photomicrograph of representative texture of sample 93012301B from Austhovde.

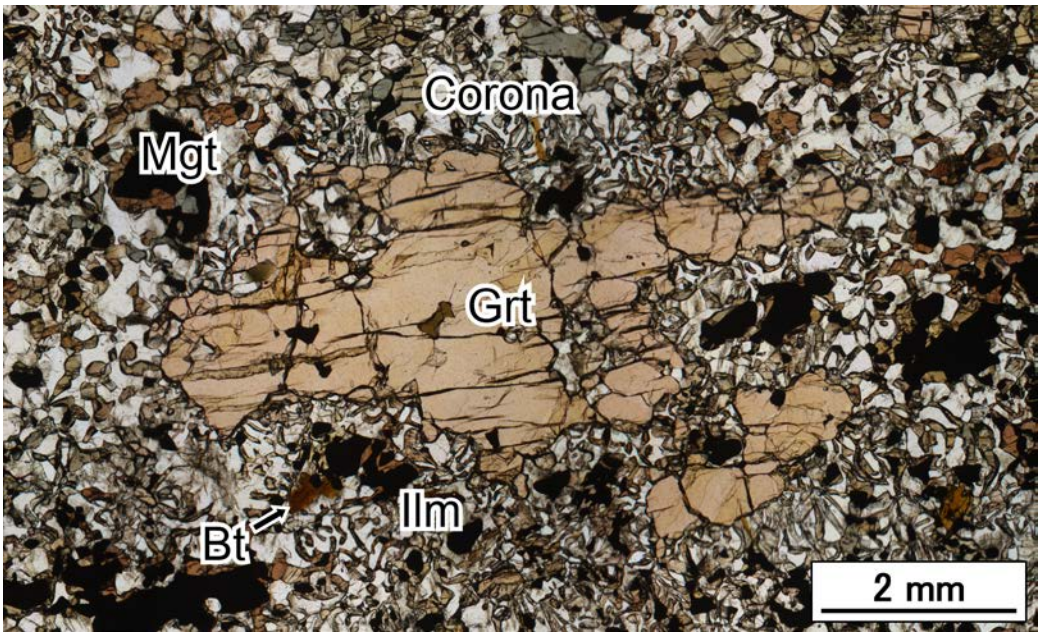

Figure 4-20. Photomicrograph of representative texture of sample 93012411B from Austhovde.

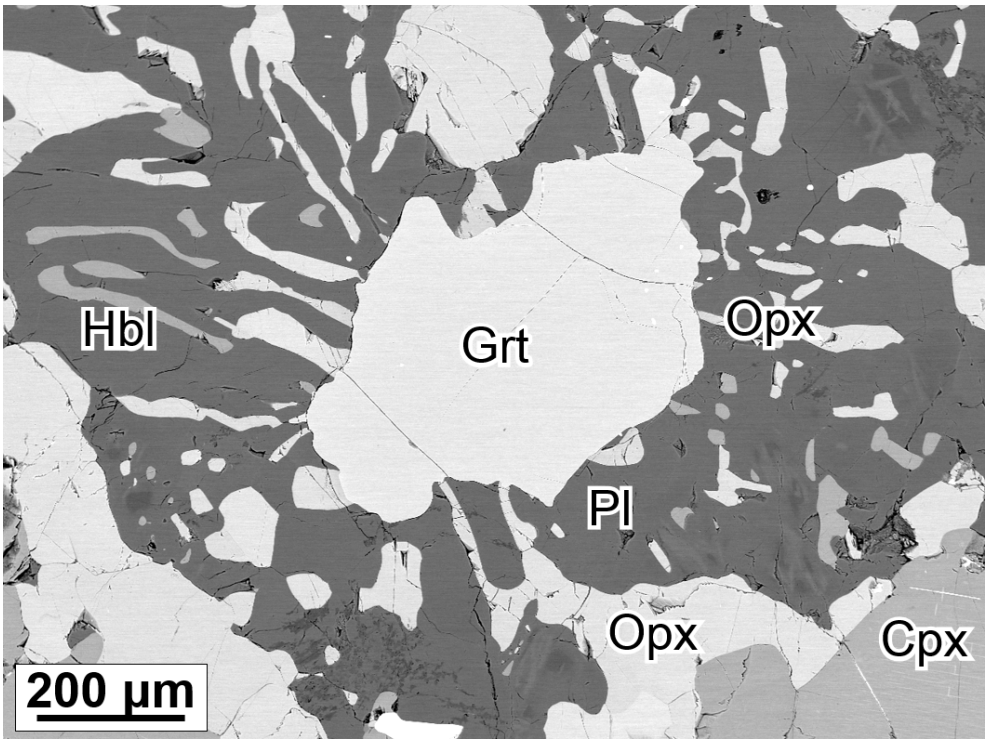

Figure 4-21. BSE image of representative texture of sample 93012301C from Austhovde.

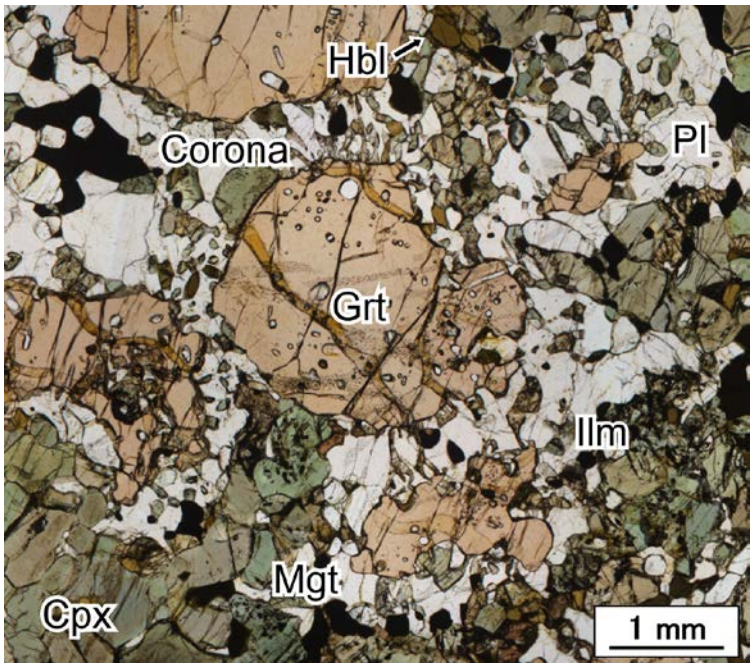

Figure 4-22. Photomicrograph of representative texture of sample 84011107(T) from Innhovde.

4.1.2. I-030 from Akarui Point

The studied gneiss (sample no. I-030) was collected by Dr. Takeshi Ikeda from Akarui Point during the 44th Japanese Antarctic Research Expedition (JARE 44). The gneiss is composed mainly of garnet, hornblende, plagioclase, orthopyroxene, biotite, and gedrite (Fig. 4-23).

Petrography

Garnet porphyroblast is large as 2 cm in diameter (Fig. 4-23). The rim of the garnet locally shows concavo-convex shape.

The matrix plagioclase (up to 1.5 mm) shows strong concentric optical extinction, while that of inclusion plagioclase (up to 1.5 mm) in garnet is weak (Fig. 4-24). Some of these plagioclase exhibits albite twinning. Rounded grain of plagioclase also included in matrix hornblende.

The matrix hornblende (up to 2 mm) exhibits pleochroism from bluish-green to brownish-green (Fig. 4-24). Similar shaped and colored hornblende is included in garnet porphyroblast. Rounded hornblende is rarely included in matrix plagioclase. Some inclusion hornblende in rim of garnet porphyroblast is partially exposed from the host garnet and in contact with corona (Fig. 4-24).

The matrix orthopyroxene shows rounded to elongated shape (1 mm long) (Fig. 4-24). Similar shaped and sized orthopyroxene is rarely included in the garnet porphyroblast (Fig. 4-24). They show pleochroism from reddish-brown to pale blown.

The matrix biotite is up to 3 mm long (Fig. 4-24). It shows pleochroism from

bluish-green to brownish-yellow (Fig. 4-24).

Gedrite (up to 3 mm) is present as inclusion in garnet (Fig. 4-23).

Corona of intergrowth of gedrite and plagioclase develops between garnet porphyroblast and matrix (Fig. 4-23). Thickness of the corona is about 8 mm. The corona is divided into several domains regarded as area of simultaneous optical extinction of gedrite or plagioclase (Fig. 4-24). The boundaries of the domains are almost perpendicular to the garnet porphyroblast. The coronal gedrite shows pleochroism from bluish-green to brownish-yellow. The coronal plagioclase is partially altered to potassium-rich fine-grained aggregate that is observed as brownish cloud under a polarizing microscope.

Felsite-nanogranite Inclusion in Garnet

The numerous FNIs (10 – 700 μm) are distributed in entire garnet. The positions of analyzed 20 FNIs are shown in Figure 4-23. Representative texture of the FNIs are shown in Figure 4-25. They show polygonal shape that is considered to be negative crystal shape of garnet, and cuspate or spear-shaped structures are commonly observed. Quartz, biotite, plagioclase, magnetite, andalusite, sillimanite, scapolite, apatite, cordierite, talc, chlorite, hornblende, and gedrite are found as constituent minerals of the FNIs. The major mineral assemblage is quartz + plagioclase + biotite, but the constituent minerals of the FNIs are different among all the analyzed FNIs. The mineral assemblages are summarized in Table 4-2. The constituent minerals of the FNIs represent anhedral shape except for magnetite showing euhedral shape. The FNIs shows granitic texture rather than felsitic texture which shows dendritic textures or contains glass as a constituent phase. Andalusite is

abundant phase as aluminosilicate, whereas sillimanite is also found in a FNI. Scapolite found in two FNIs is directly in contact with andalusite. Hornblende is separated from quartz by sillimanite, apatite, and biotite. Gedrite shows lath-like or irregular shapes.

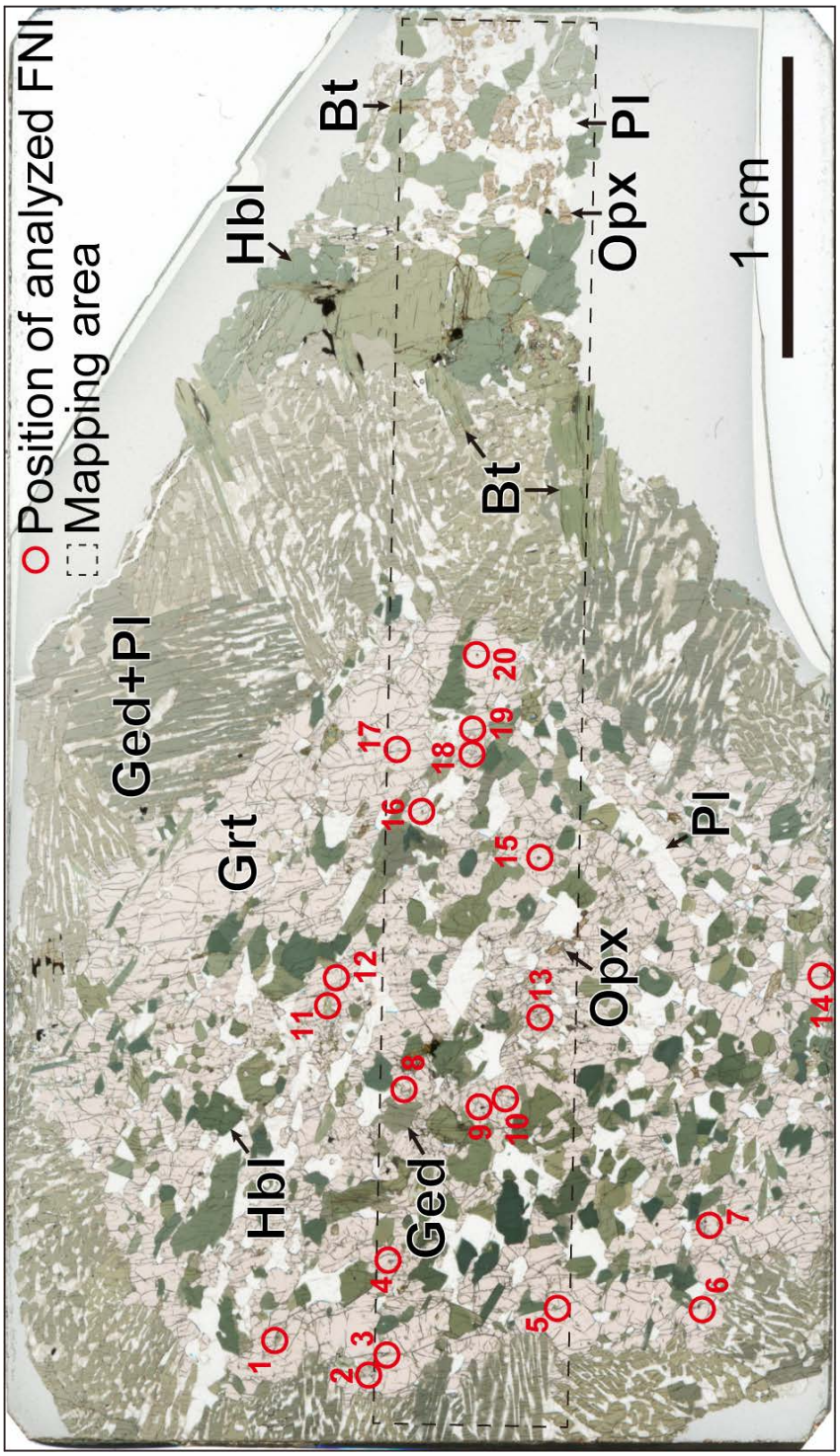

Figure 4-23. Photograph of thin section showing whole texture of I-030.

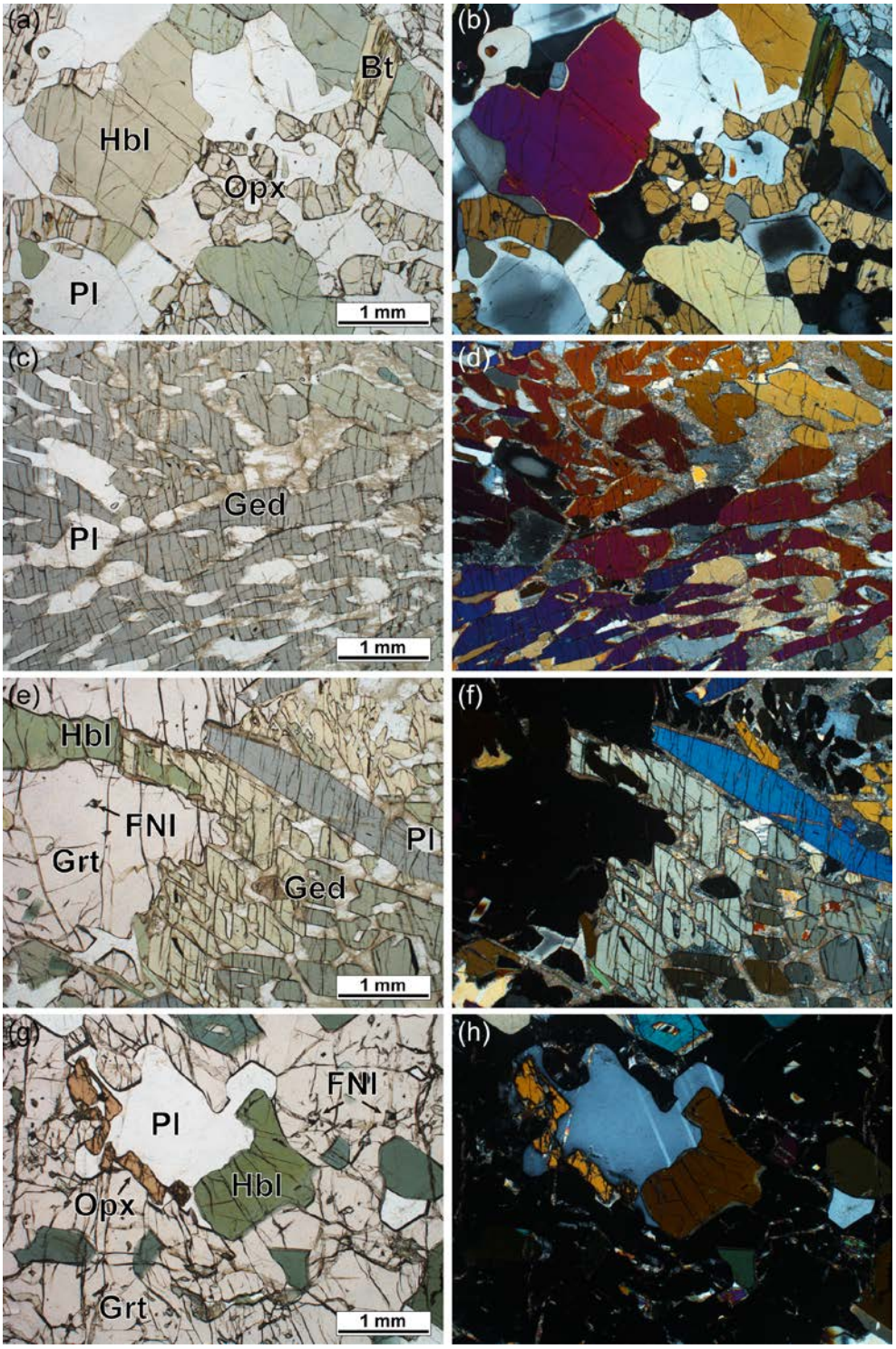

Figure 4-24. Photomicrographs showing representative textures of I-030. (a, b) Matrix. (c, d) Corona. (e, f) Boundary between corona and garnet. Inclusion hornblende is partially exposed to corona. (g, h) Inclusion minerals in garnet.

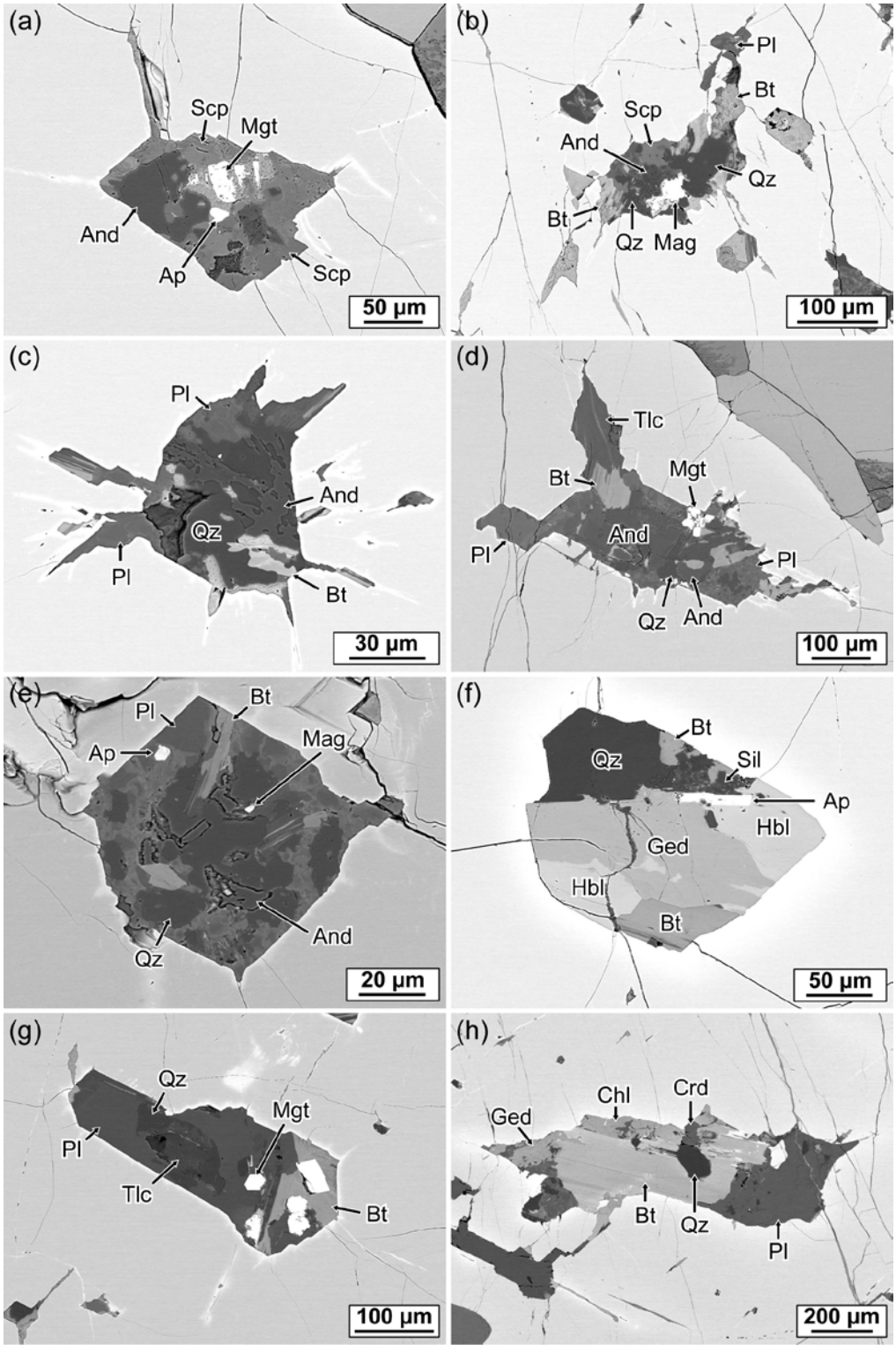

Figure 4-25. BSE images showing representative textures of felsite-nanogranite inclusions. Note that scapolite and andalusite are directly in contact each other. FNI numbers: (a), 6; (b), 13; (c), 8; (d), 7; (e), 3; (f), 5; (g), 10; (h), 11.

Table 4-2. Mineral assemblages in felsite-nanogranite inclusion

No.	Qz	Bt	Pl	Mag	And	Sil	Scp	Ap	Crd	Tlc	Chl	Hbl	Ged
1	○	○	○		○								○
2		○	○										
3	○	○	○	○	○			○					
4	○		○										
5	○	○				○		○				○	○
6	○			○	○		○						
7	○	○	○	○	○					○			
8	○	○	○		○								
9	○	○	○	○						○			
10	○	○	○	○						○			
11	○	○	○						○		○		○
12	○	○	○	○							○		
13	○	○	○	○	○		○						
14	○	○	○							○			
15	○	○	○		○			○					
16	○	○		○	○					○			
17	○	○	○								○		
18			○										
19	○	○	○										
20	○	○		○									

4.1.3. Pelitic Gneiss from Niban Rock

The studied pelitic gneiss (sample no. TM11020702A) was collected from Niban-higashi rock by Dr. Tomoharu Miyamoto during the 52nd Japanese Antarctic Research Expedition (JARE 52). The constituent minerals are quartz, garnet, biotite, sillimanite, plagioclase with minor amounts of ilmenite, kyanite, zircon, rutile, apatite, monazite, and xenotime (Fig. 4-26). Garnet porphyroblast is about 1.5 mm in diameter. Rim of garnet is partially replaced by plagioclase, biotite, and sillimanite. Garnet contains many tiny inclusions of quartz, plagioclase, kyanite, sillimanite, ilmenite, rutile, zircon, monazite, and xenotime. In garnet, inclusion kyanite is present in core (Fig. 4-27), whereas inclusion sillimanite is present in rim. Quartz, kyanite, and rutile are directly in contact with each other in the core of garnet (Fig. 4-27). Sillimanite is abundant phase as aluminosilicate in the matrix rather than kyanite. Kyanite in the matrix is rimmed by plagioclase and is not in contact with quartz directly. Rutile occurs only as inclusion in garnet or quartz in the matrix. Ilmenite occurs both in the matrix and as inclusion in garnet. Zircon occurs in the matrix and as inclusion in garnet, plagioclase, and quartz.

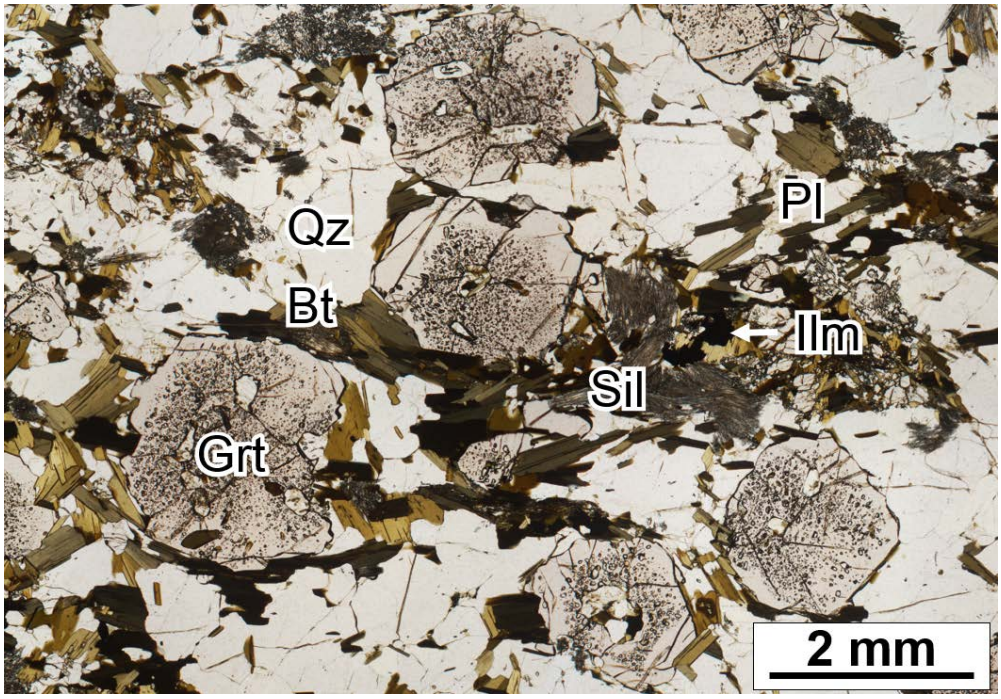

Figure 4-26. Photomicrograph showing texture of pelitic gneiss from Niban Rock.

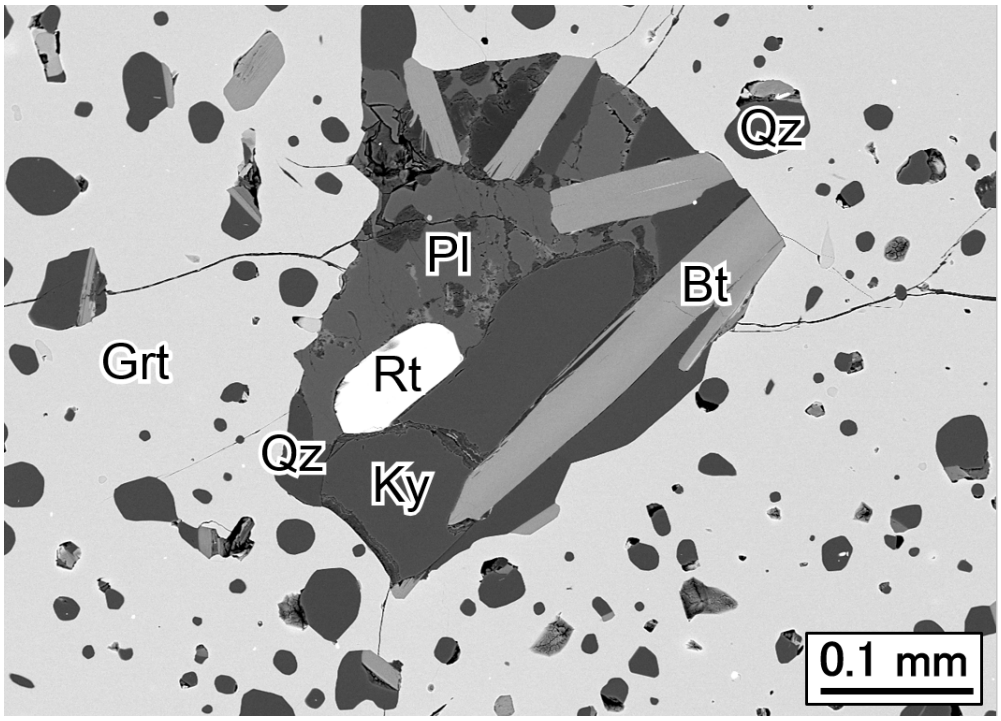

Figure 4-27. Photomicrograph showing direct contact between kyanite and rutile.

4.2. Chemical composition

4.2.1. Garnet in All Samples

All the results of garnet analyses are shown in Figure 4-28 – 4-48. Prograde zoning of Mn-rich and Fe-poor core is observed in garnet from Akebono Rock only (Figure 4-29). Garnet from Niban Rock was almost chemically homogeneous, while retrograde zoning of Fe-rich and Mg-poor composition is observed at rim only (Figure 4-30). Garnets from the other localities have retrograde zoning of Mg-rich and Fe-poor core. I could not identify core-rim structure of garnet from Cape Ryugu and Berrodden because the garnet is irregular shape (Figures 4-28, 4-42). Most garnet is rich in almandine content [= $Fe^{2+}/(Fe^{2+}+Mg+Ca+Mn)$], whereas garnets from Akarui Point and Rundvagshetta are rich in pyrope content [= $Mg/(Fe^{2+}+Mg+Ca+Mn)$]. Compositional range of grossular content [= $Ca/(Fe^{2+}+Mg+Ca+Mn)$] of most garnet is 0.1 – 0.3. Some garnet (e.g., from Austhovde) shows irregular compositional profile in terms of Ca.

Cr mapping was performed for garnet in I-122 from Rundvågshetta. The polygonal-shaped oscillatory zoning of Cr in the garnet was observed, and the zoning is partially cut by symplectitic corona of orthopyroxene and plagioclase (Figure 4-49).

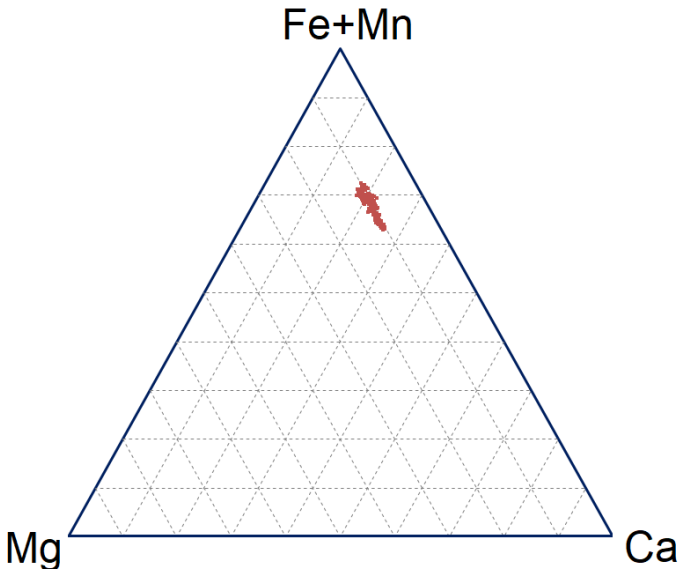

Figure 4-28. Fe-Mn-Ca-Mg ternary diagram showing variation in chemical composition of garnet in YN78010312 (Cape Ryugu).

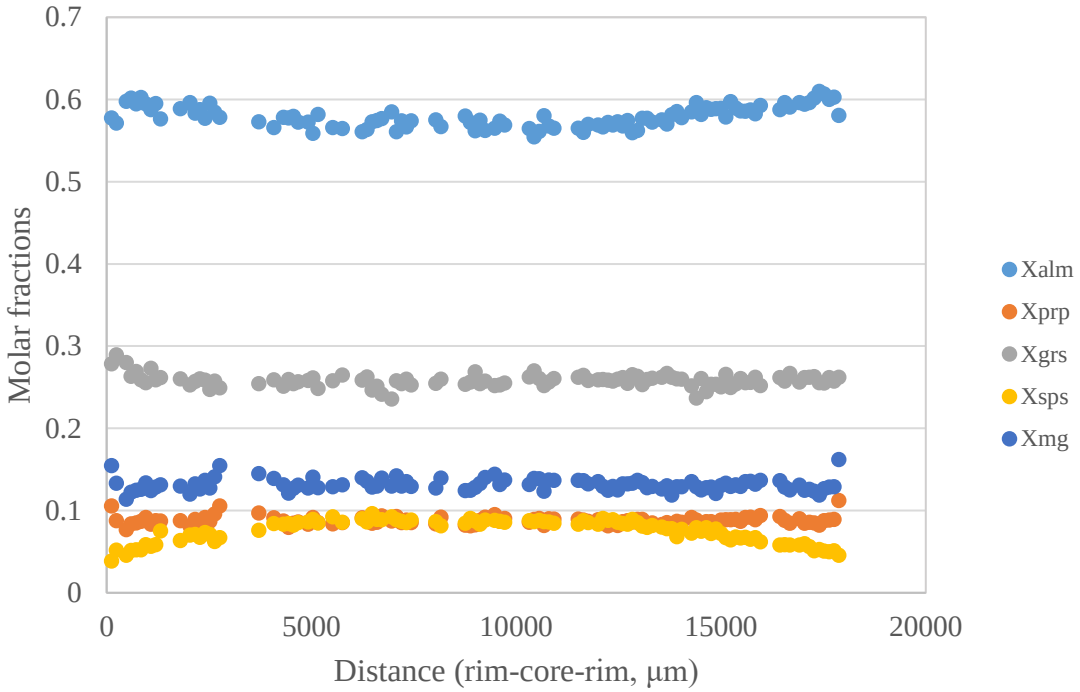

Figure 4-29. Zoning prolife of garnet inYH81012016 from Akebono rock (rim to core to rim).

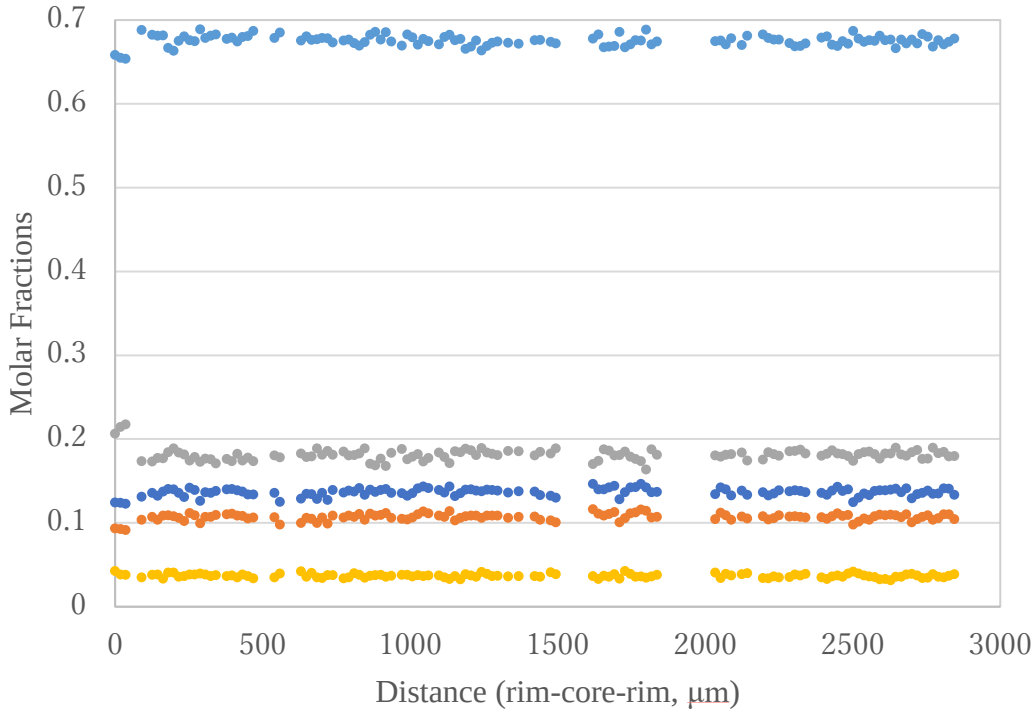

Figure 4-30. Zoning prolife of garnet in TM11020803A from Niban rock (rim to core to rim).

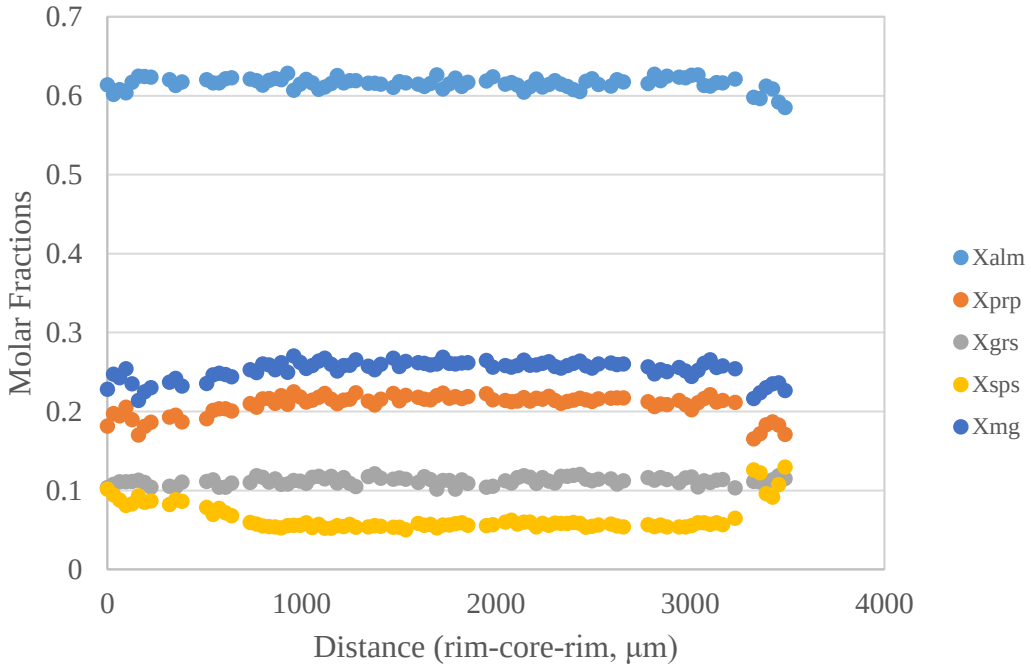

Figure 4-31. Zoning prolife of garnet in I-554 from Kasumi rock (rim to core to rim).

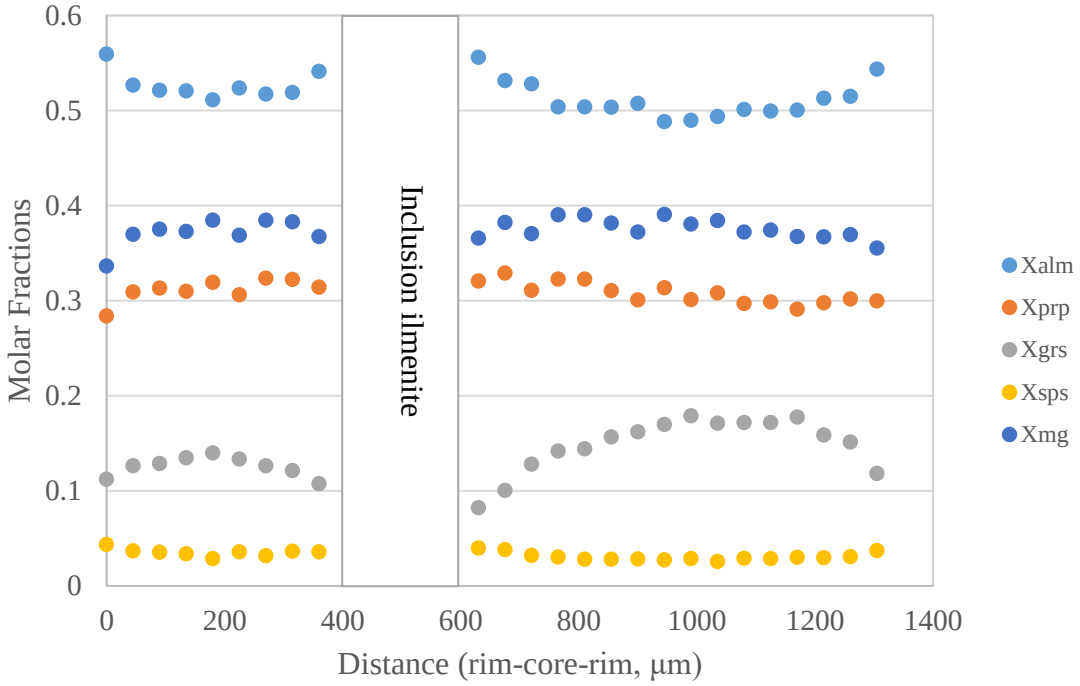

Figure 4-32. Zoning prolife of garnet in TM11021006A from Tenmondai rock (rim to core to rim).

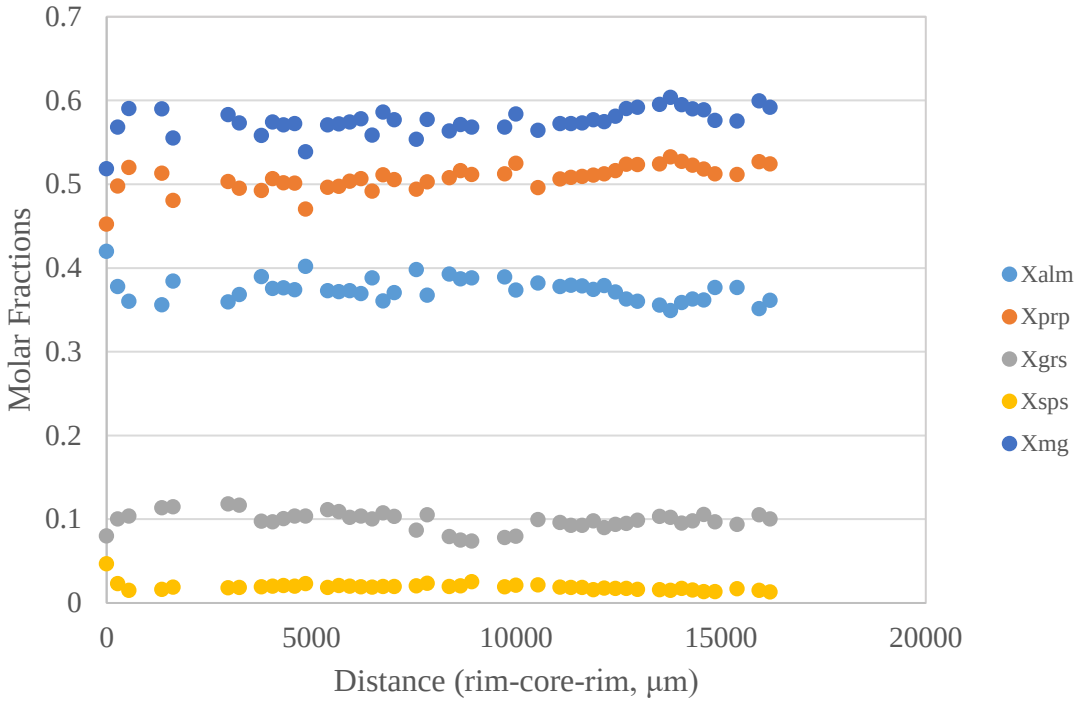

Figure 4-33. Zoning prolife of garnet in I-008 from Akarui Point (rim to core to rim).

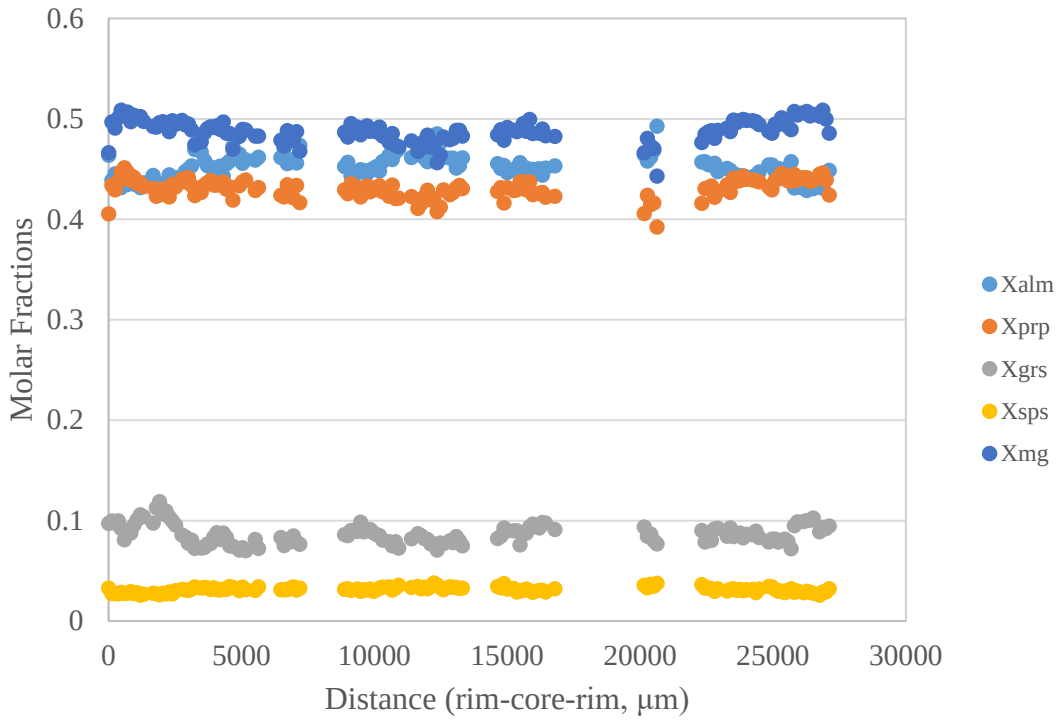

Figure 4-34. Zoning prolife of garnet in I-030 from Akarui Point (rim to core to rim).

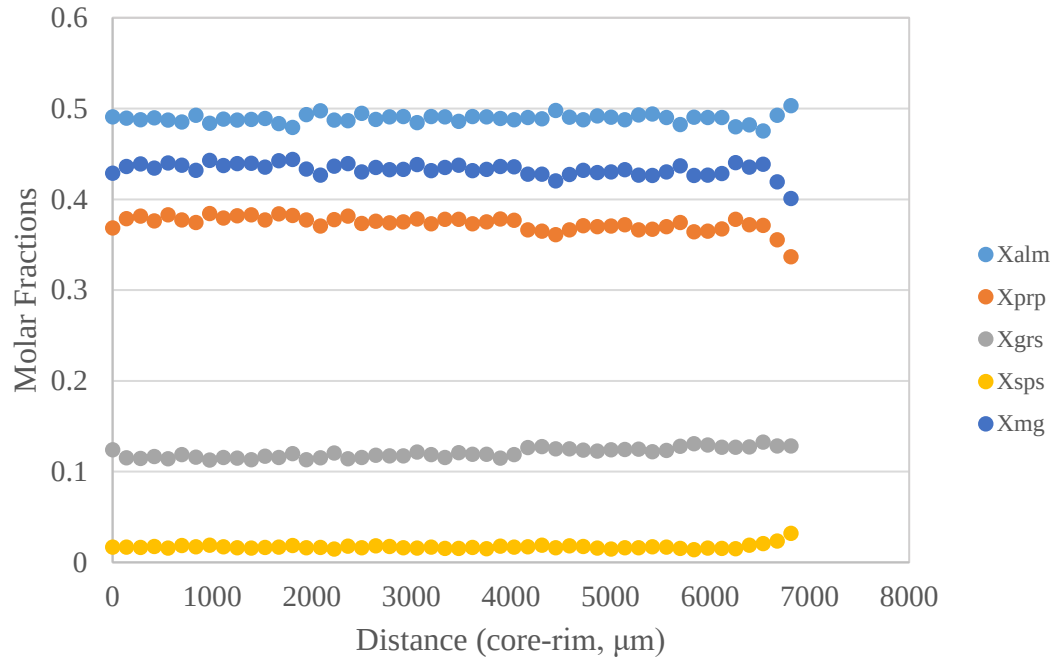

Figure 4-35. Zoning prolife of garnet in I-518 from East Ongul Island (core to rim).

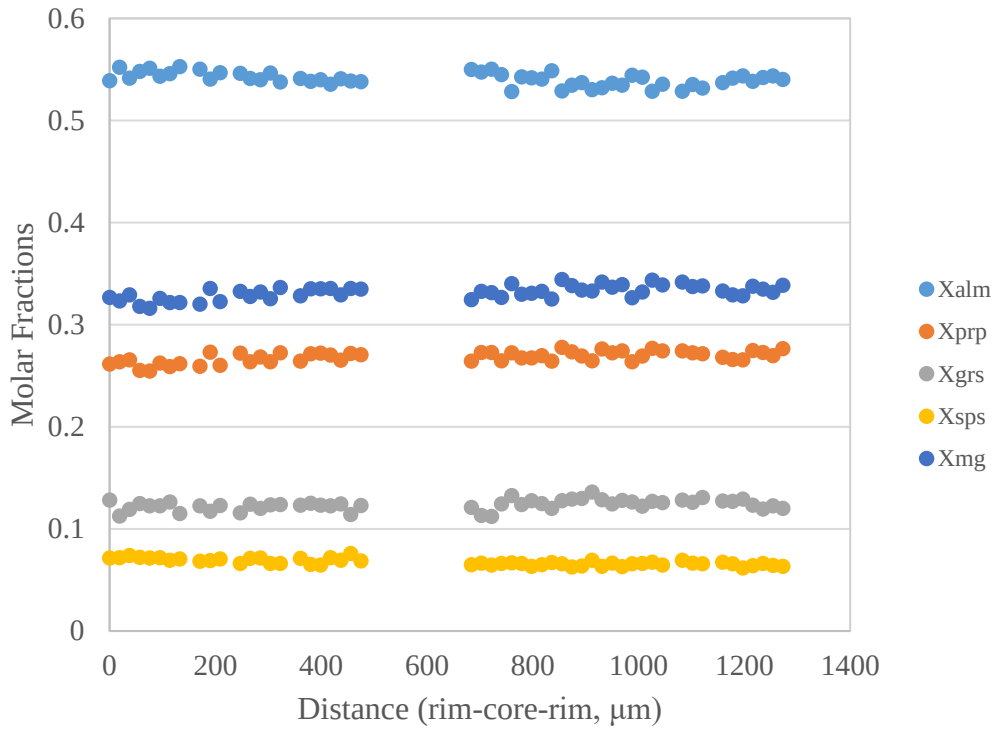

Figure 4-36. Zoning prolife of garnet in TM11021501E from Langhovde (rim to core to rim).

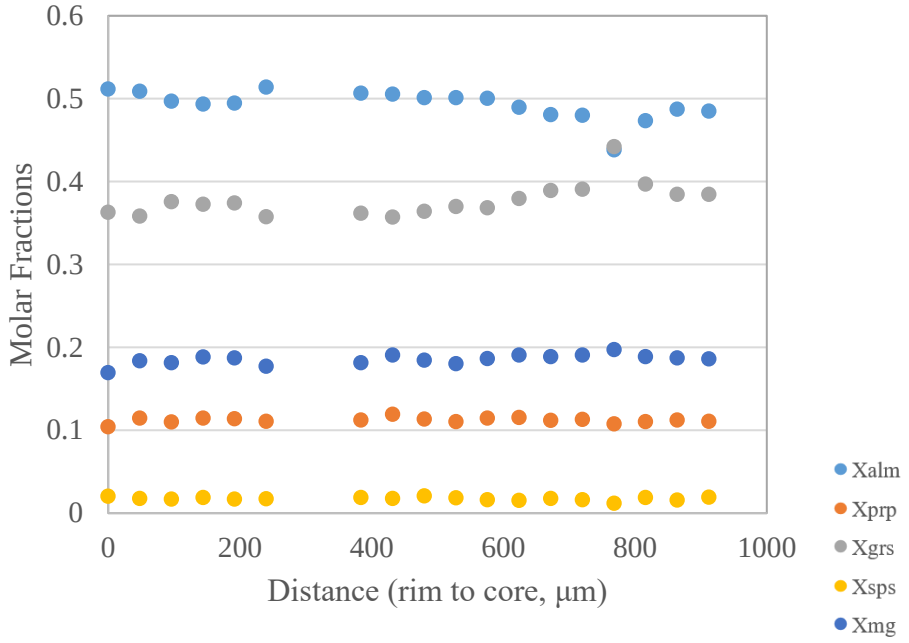

Figure 4-37. Zoning prolife of garnet in 92010203A from Skarvsnes (rim to core).

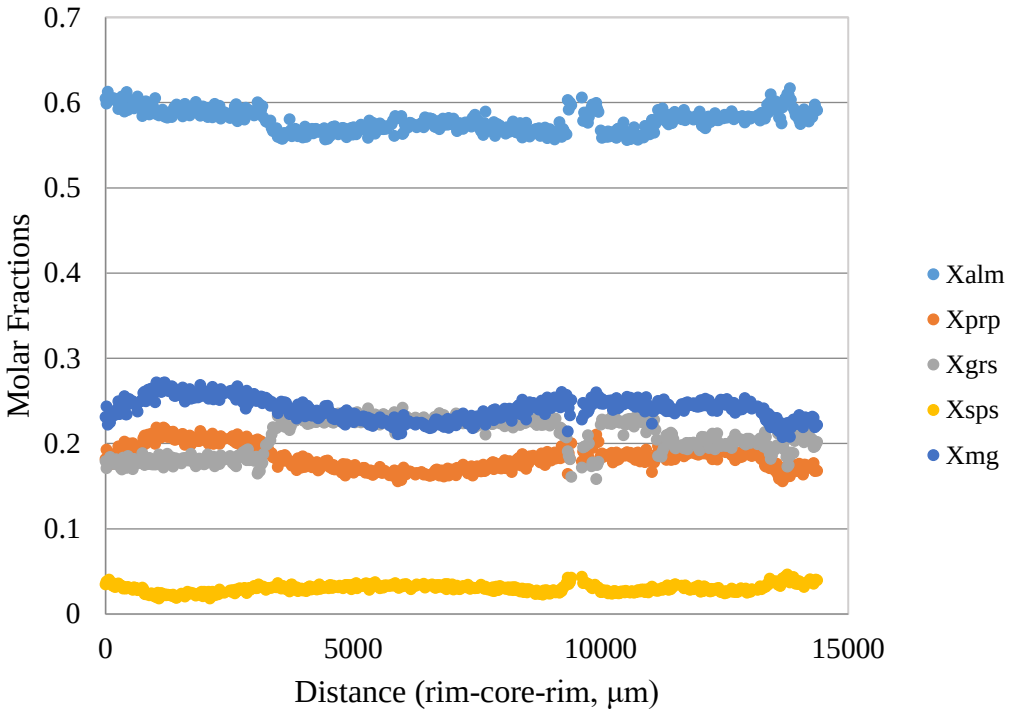

Figure 4-38. Zoning prolife of garnet in I-223 from Skallen (rim to core to rim).

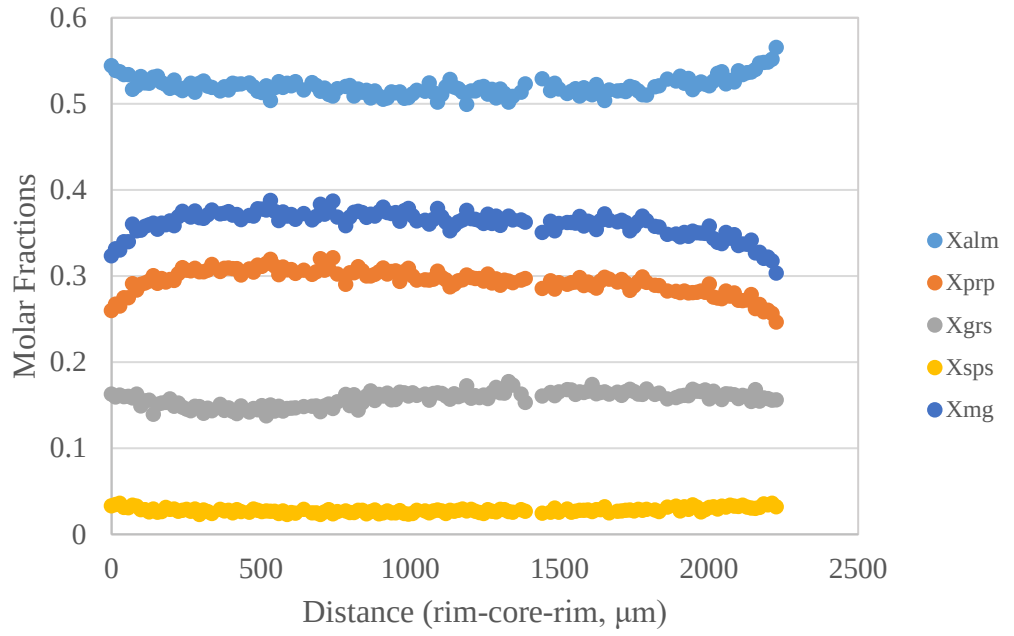

Figure 4-39. Zoning prolife of garnet in I-232 from Skallen (rim to core to rim).

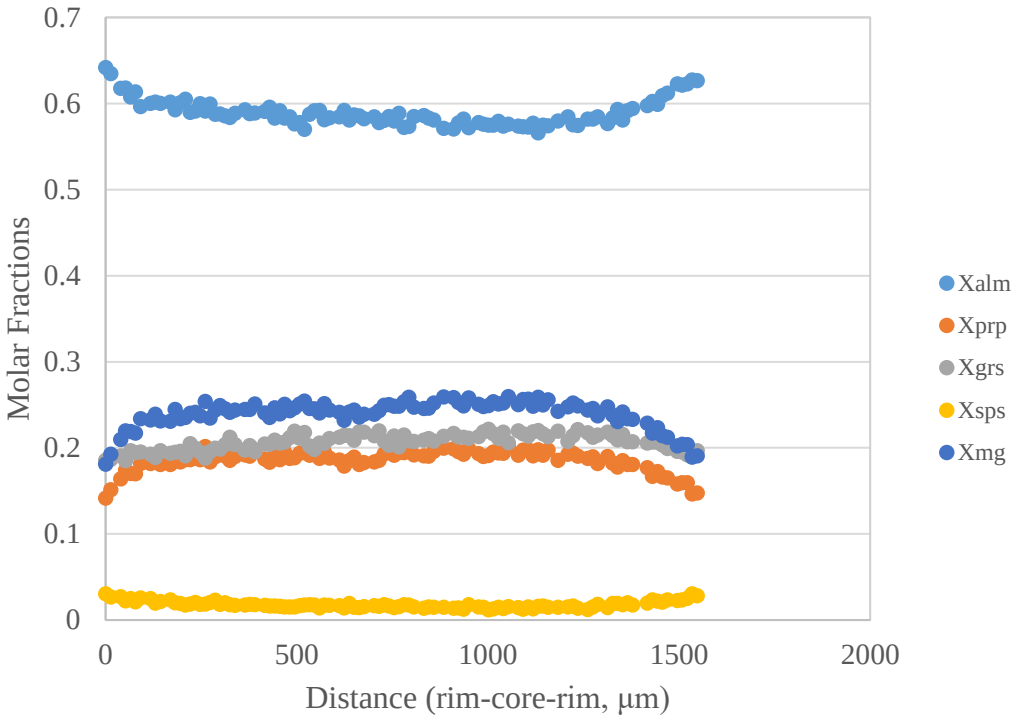

Figure 4-40. Zoning prolife of garnet in I-293 from Skallevikshalsen (rim to core to rim).

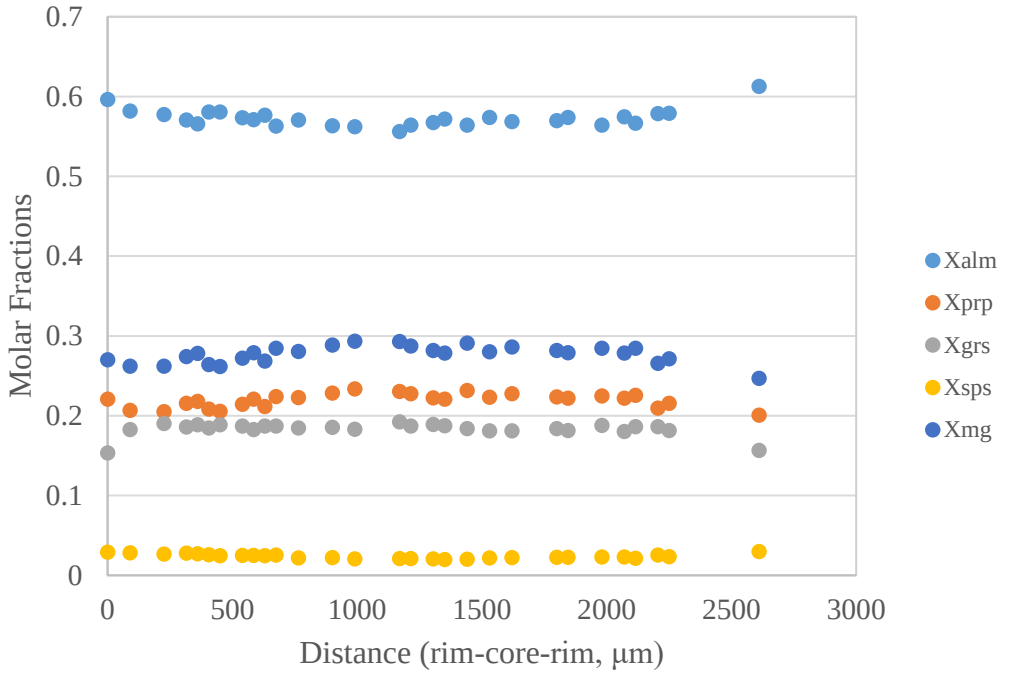

Figure 4-41. Zoning prolife of garnet in TM11010503E from Sudare Rock (rim to core to rim).

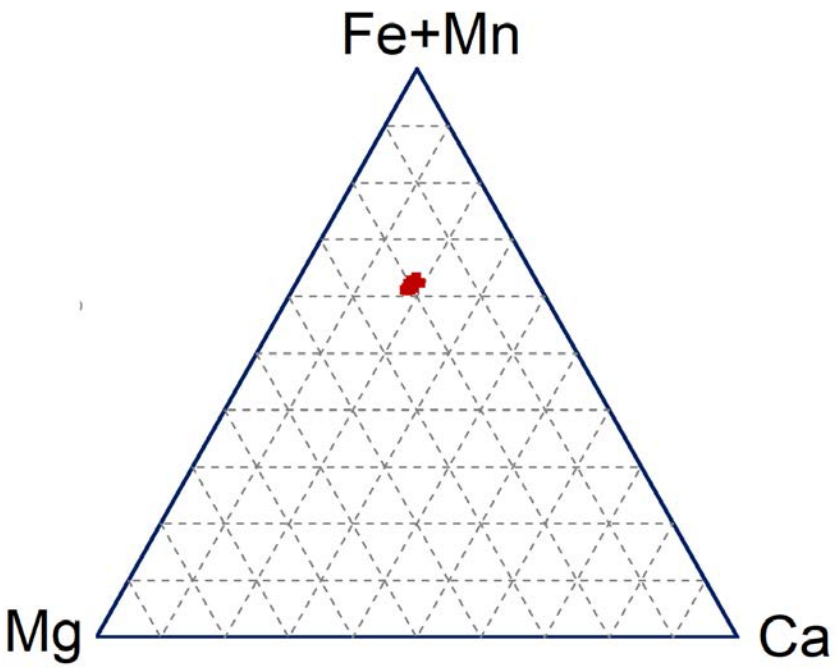

Figure 4-42. Fe-Mn-Mg-Ca diagram showing composition of garnet from Berrodden

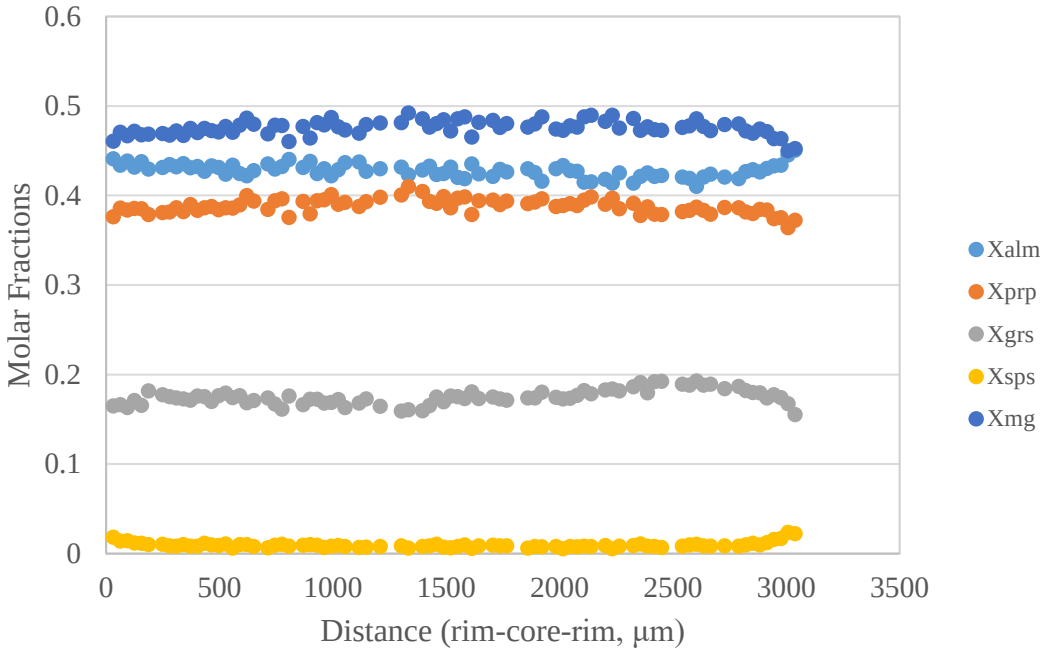

Figure 4-43. Zoning prolife of garnet in I-122 from Rundvågshetta (rim to core to rim)

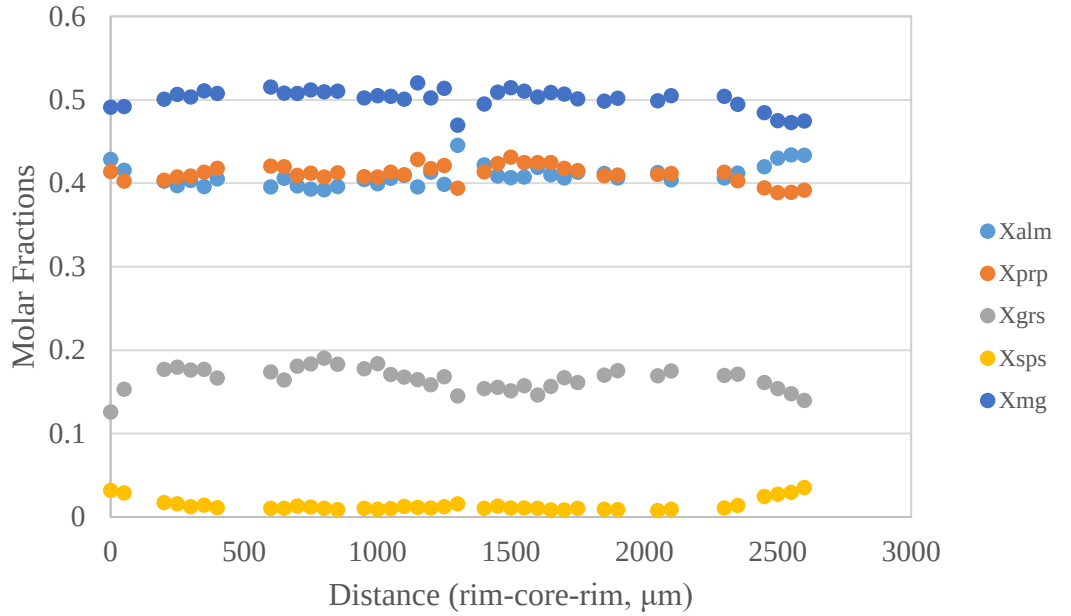

Figure 4-44. Zoning prolife of garnet in 93010701C from Rundvågshetta (rim to core to rim).

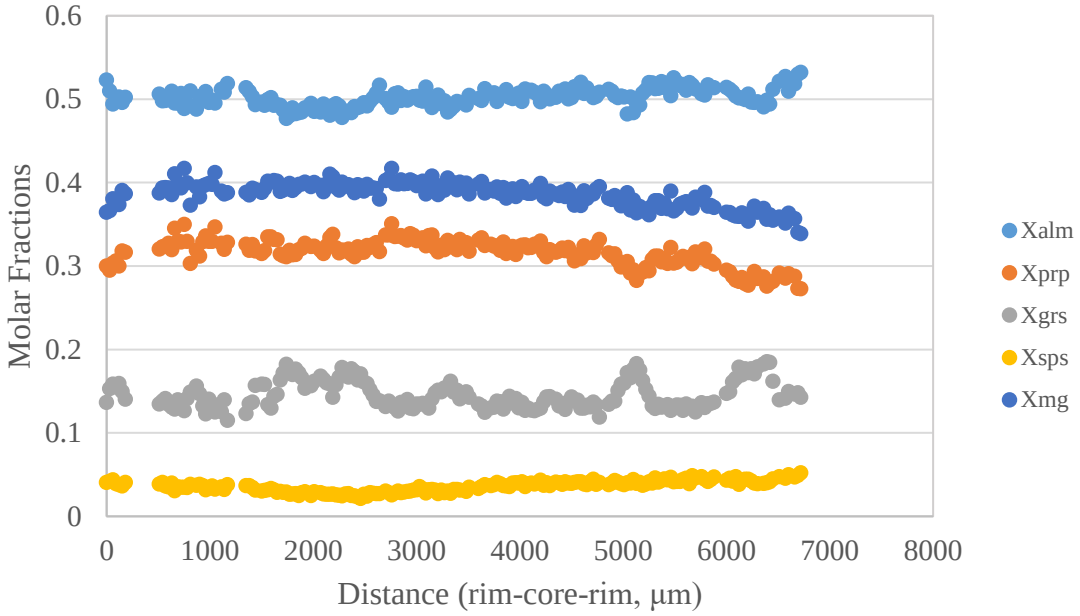

Figure 4-45. Zoning prolife of garnet in 93012411B from Austhovde (rim to core to rim).

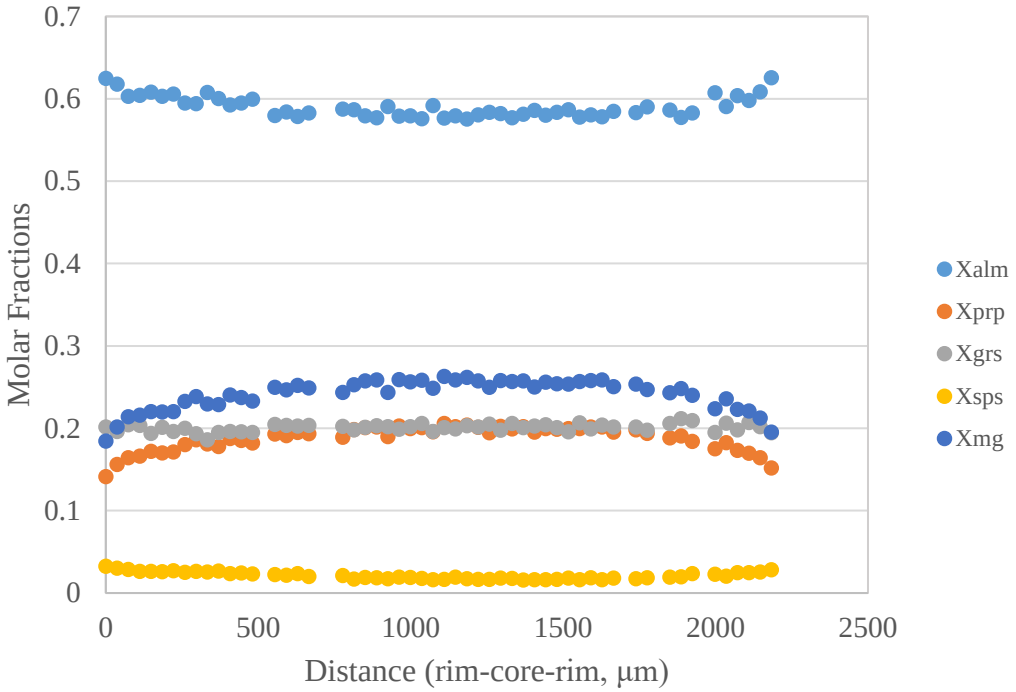

Figure 4-46. Zoning prolife of garnet in 93012301B from Austhovde (rim to core to rim).

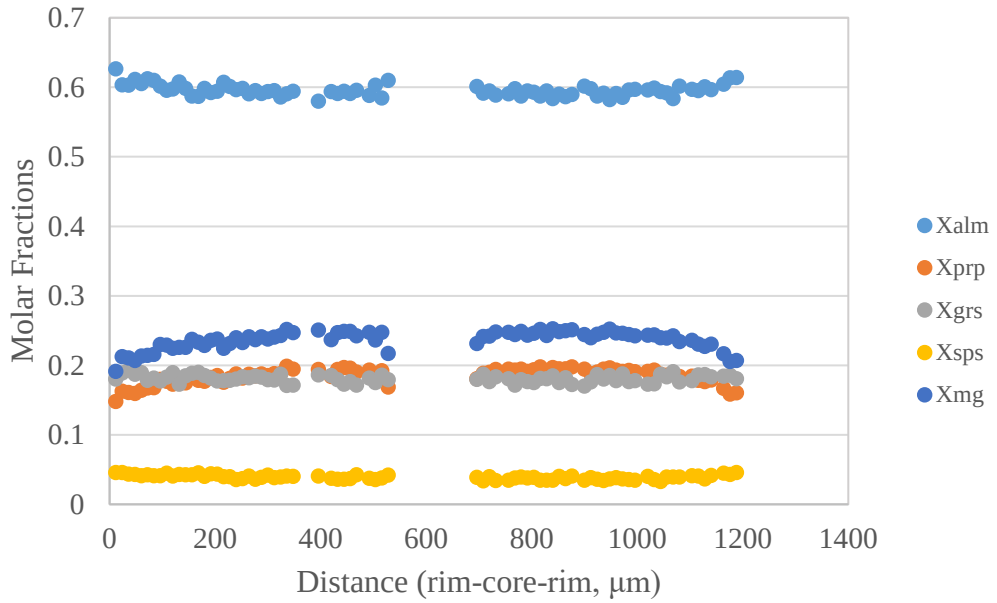

Figure 4-47. Zoning prolife of garnet in 93012301C from Austhovde (rim to core to rim).

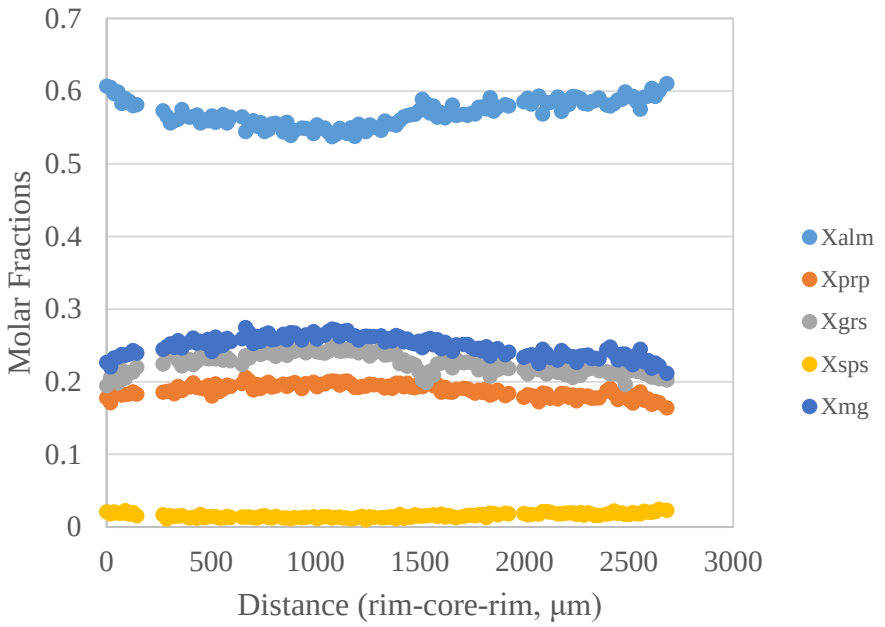

Figure 4-48. Zoning prolife of garnet in 84011107(T) from Innhovde (rim to core to rim).

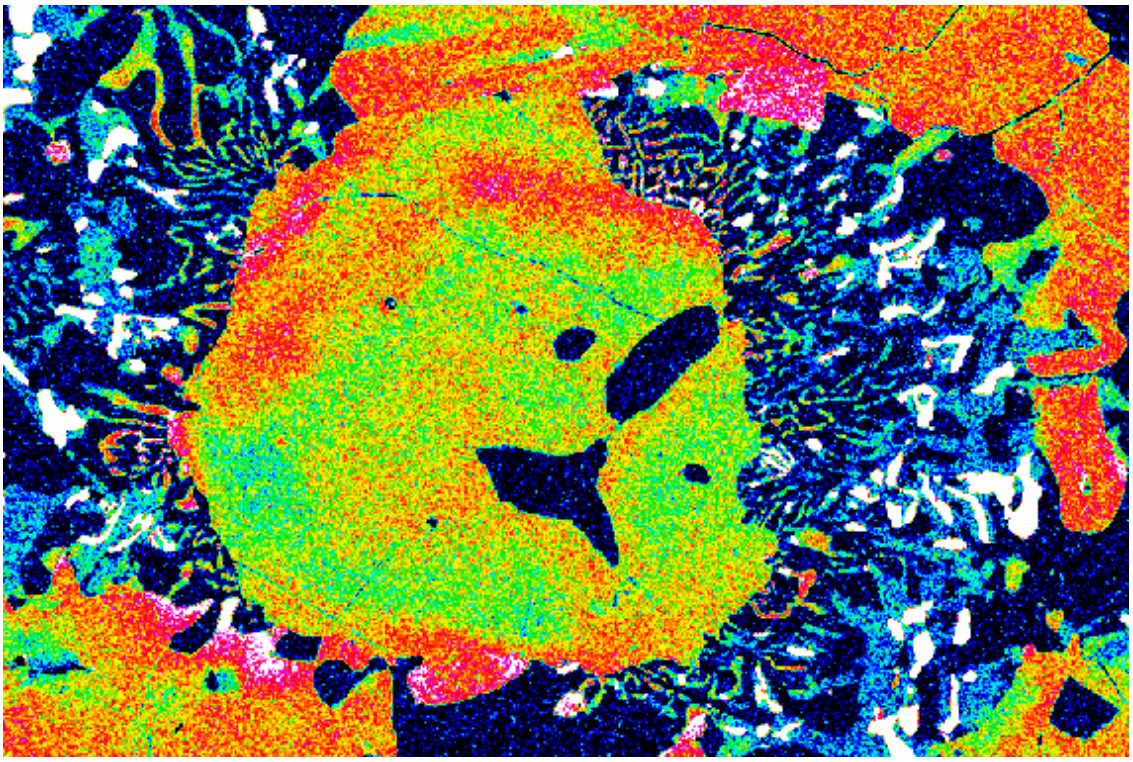

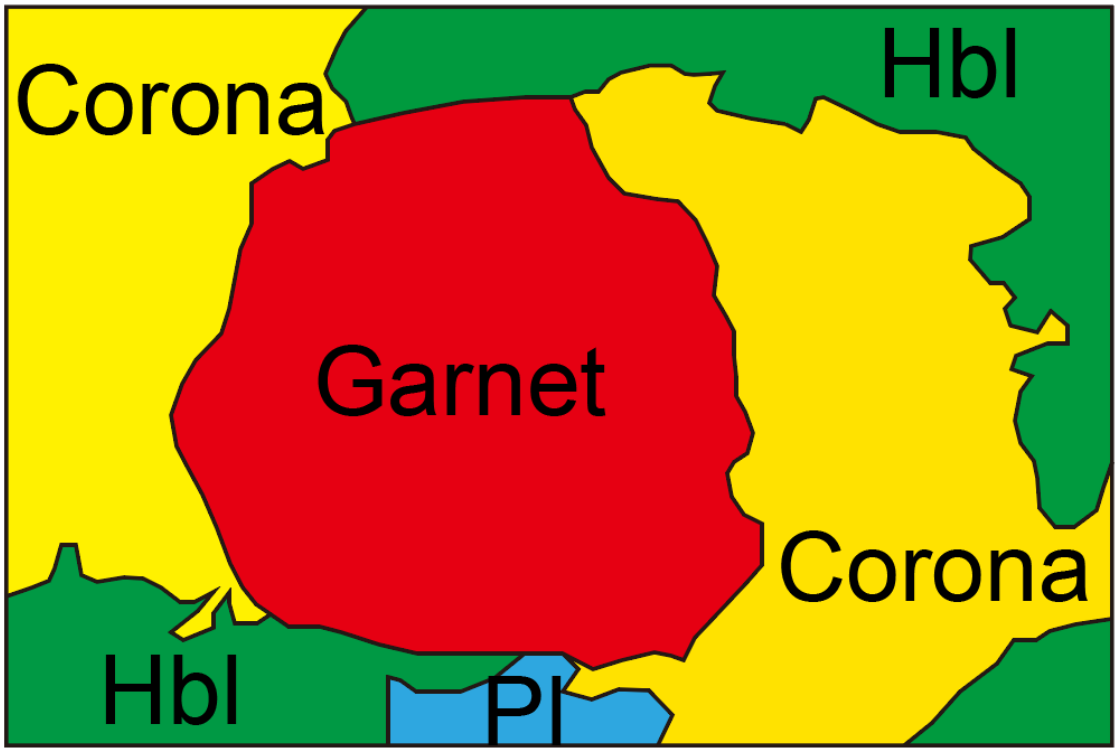

Figure 4-49. Cr mapping of a corona-bearing sample I-122 from Rundvågshetta. Distribution of minerals is illustrated in the bottom figure.

4.2.2. Calcic Amphibole in All Samples

Various compositions of calcic amphibole are observed in the studied samples. Representative ten analyses of matrix amphibole in each sample are shown in Table 4-3 – 4-23. Compositions of amphibole in corona-free and corona-bearing samples does not distinguish each other even if all elements are considered.

Compositions of amphiboles can be roughly categorized according to location of exposure in the LHC. Si in amphibole in studied samples from amphibolite-facies zone is higher than that from transitional and granulite-facies zones (Figure 4-50). Amphiboles from Akarui Point and all northeastern exposures of Akarui Point are poor in Na[A] + K (mostly < 0.5 apfu), whereas amphiboles from all exposures which locate southwestern than Akarui Point are rich in Na[A] + K (mostly >0.5 apfu) (Figure 4-51). X_{Mg} [=Mg/(Mg+Fe^{2+})] is highest at Akarui Point and is second highest at Rundvågshetta (Figure 4-52). Samples from transitional and granulite-facies zones are basically rich in F or Cl (Figures 4-53, 4-54). Amphibole from Akebono Rock is rich in F exceptionally as an exposure in amphibolite-facies zones (Figure 4-54). Cl content largely varies even in one exposure. Mg-Cl avoidance are observed in amphiboles in most samples that contain Cl (Figure 4-53).

As mentioned in the introduction section, I focus on the Cl content as a tracer of mass transfer which occurs if amphibole is consumed by formation of corona. To investigate the relation between Cl-zoning in amphiboles and corona-bearing or corona-free samples, appropriate samples should be selected from all samples to make more detailed chemical analysis. In this study, the following three types of samples should be used.

(1) Cl-rich amphibole in corona-bearing samples.

(2) Cl-rich amphibole in corona-free samples.

(3) Cl-free amphibole in corona-bearing samples.

The Cl-rich amphiboles in corona-bearing samples are used for investigation of amphibole for coronal formation. The Cl-rich amphiboles in corona-free samples are also required to confirm that the Cl in amphiboles shows opposite tendency of Cl in amphibole in corona-bearing samples. In addition, Cl-free amphiboles in corona-bearing samples should be checked the possibility of the Mg-Cl avoidance controlled by Mg content. Therefore, I selected the following six samples.

(1) I-008 from Akarui Point, I-030 from Akarui Point, I-518 from East Ongul Island, and 93012301B from Austhovde

(2) 93012301C from Austhovde

(3) I-122 from Rundvågshetta

I performed X-ray elemental mapping for the six samples. The results are shown in Figures 4-55 – 4-62. Elemental mapping of 93012301C from Austhovde was accidentally stored only Na and Mg due to machine problem. Line profiles of Cl in amphibole grains that is in contact with garnet or corona is also shown.

Cl-bearing amphibole in corona-bearing samples show a common feature of core-rim structure in terms of Cl. The rims are rich in Cl, and the cores are poor in Cl. The Cl content of rims decrease with distance from corona. Cl-rich compositions of amphibole show Fe^{2+}-, Al-, and K-rich and Si- and Mg- poor composition. This compositional variation of amphibole is explained by Mg-Cl avoidance (Figures 4-55, 4-56, 4-57, 4-61, 4-62).

Cl-bearing amphibole in corona-free sample does not show core-rim structure in terms of Cl (Figure 4-59). The Cl content is almost constant in one grain irrespective of

distance from garnet. Mg content is locally high and does not show correlation with Cl content. This can be explained by Fe-Mg exchange with contacting minerals.

Cl-free amphibole in corona-free samples does not show core-rim structure in terms of all elements. Mg content is locally high, and this can be explained by Fe-Mg exchange with contacting minerals (Figure 4-60).

Table 4-3. Representative analyses of matrix amphibole in YN78010312 from Cape Ryugu

Exposure	Cape Ryugu	Cape Ryugu	Cape Ryugu	Cape Ryugu	Cape Ryugu	Cape Ryugu	Cape Ryugu	Cape Ryugu	Cape Ryugu	Cape Ryugu
Corona	Free	Free	Free	Free	Free	Free	Free	Free	Free	Free
Sample	YN78010312	YN78010312	YN78010312	YN78010312	YN78010312	YN78010312	YN78010312	YN78010312	YN78010312	YN78010312
Analysis Point	Ryugu_amp002	Ryugu_amp018	Ryugu_amp020	Ryugu_amp033	Ryugu_amp039	Ryugu_amp141	Ryugu_amp057	Ryugu_amp063	Ryugu_amp130	Ryugu_amp133
SiO_2	41.95	42.11	41.31	42.17	42.28	41.52	42.25	42.38	41.79	41.95
TiO_2	1.35	1.36	1.63	1.37	1.36	1.49	1.57	1.59	1.43	1.58
Al_2O_3	12.16	12.00	11.98	12.20	11.72	12.21	11.24	11.84	12.16	12.02
Cr_2O_3	0.01	0.05	0.09	0.08	0.08	0.00	0.03	0.00	0.00	0.02
FeO	20.62	20.51	19.91	19.97	20.44	20.16	20.29	20.24	19.85	19.93
MnO	0.22	0.27	0.25	0.23	0.25	0.19	0.21	0.15	0.28	0.25
MgO	7.89	7.82	7.33	8.04	7.88	7.22	7.88	7.72	7.59	7.70
CaO	10.77	11.04	10.73	10.68	11.09	10.69	10.74	10.70	10.51	11.21
Na_2O	1.55	1.54	1.39	1.51	1.42	1.44	1.54	1.41	1.47	1.62
K_2O	0.91	0.79	1.01	0.90	0.82	1.00	0.84	0.85	0.85	1.00
F	0.00	0.00	0.00	0.06	0.00	0.00	0.10	0.03	0.15	0.00
Cl	0.00	0.02	0.03	0.00	0.00	0.04	0.04	0.03	0.01	0.01
Total (Inc. F & Cl)	97.42	97.49	95.66	97.20	97.36	95.94	96.73	96.94	96.07	97.27
O=-F	0.00	0.00	0.00	-0.02	0.00	0.00	-0.04	-0.01	-0.06	0.00
O=-Cl	0.00	0.00	-0.01	0.00	0.00	-0.01	-0.01	-0.01	0.00	0.00
Total	97.42	97.49	95.65	97.17	97.36	95.93	96.68	96.92	96.00	97.27
Si	6.36	6.38	6.39	6.39	6.41	6.41	6.47	6.45	6.42	6.40
Ti	0.15	0.15	0.19	0.16	0.16	0.17	0.18	0.18	0.16	0.18
Al	2.17	2.14	2.19	2.18	2.10	2.22	2.03	2.12	2.20	2.16
Cr	0.00	0.01	0.01	0.01	0.01	0.00	0.00	0.00	0.00	0.00
Fe^{3+}	0.47	0.44	0.29	0.41	0.43	0.30	0.34	0.34	0.37	0.22
Fe^{2+}	2.14	2.16	2.29	2.12	2.16	2.31	2.26	2.23	2.18	2.32
Mn	0.03	0.04	0.03	0.03	0.03	0.02	0.03	0.02	0.04	0.03
Mg	1.78	1.77	1.69	1.82	1.78	1.66	1.80	1.75	1.74	1.75
Ca	1.75	1.79	1.78	1.73	1.80	1.77	1.76	1.75	1.73	1.83
Na	0.46	0.45	0.42	0.44	0.42	0.43	0.46	0.42	0.44	0.48
K	0.17	0.15	0.20	0.17	0.16	0.20	0.16	0.17	0.17	0.19
Cation Total	15.48	15.48	15.48	15.46	15.46	15.48	15.48	15.43	15.44	15.57
F	0.00	0.00	0.00	0.03	0.00	0.00	0.05	0.01	0.07	0.00
Cl	0.00	0.00	0.01	0.00	0.00	0.01	0.01	0.01	0.00	0.00
X_{Mg}	0.45	0.45	0.43	0.46	0.45	0.42	0.44	0.44	0.44	0.43

Table 4-4. Representative analyses of matrix amphibole in YH81012016 from Akebono Rock

Exposure	Akebono Rock	Akebono Rock	Akebono Rock	Akebono Rock	Akebono Rock	Akebono Rock	Akebono Rock	Akebono Rock	Akebono Rock	Akebono Rock
Corona	Free	Free	Free	Free	Free	Free	Free	Free	Free	Free
Sample	YH81012016	YH81012016	YH81012016	YH81012016	YH81012016	YH81012016	YH81012016	YH81012016	YH81012016	YH81012016
Analysis Point	Akebono_amp015	Akebono_amp016	Akebono_amp017	Akebono_amp018	Akebono_amp028	Akebono_amp029	Akebono_amp030	Akebono_amp036	Akebono_amp037	Akebono_amp038
SiO_2	42.21	42.75	42.32	42.12	42.13	42.71	42.89	42.49	42.17	42.28
TiO_2	1.30	0.95	1.18	0.97	0.79	0.82	0.77	0.67	0.92	0.67
Al_2O_3	12.07	11.72	13.02	12.74	13.69	12.80	12.38	13.09	13.27	13.42
Cr_2O_3	0.06	0.00	0.00	0.00	0.00	0.00	0.05	0.03	0.00	0.00
FeO	17.01	16.99	16.98	16.58	16.04	16.61	16.69	16.71	16.61	17.18
MnO	0.22	0.13	0.09	0.13	0.16	0.13	0.13	0.12	0.10	0.20
MgO	8.80	9.16	8.97	8.91	8.46	9.12	9.17	9.21	9.07	8.64
CaO	11.72	11.67	11.42	12.07	11.61	11.57	11.75	11.94	11.73	11.52
Na_2O	1.23	1.03	1.23	1.07	1.14	1.16	1.07	1.17	1.19	1.24
K_2O	1.13	1.08	1.26	1.14	1.04	1.01	0.98	1.06	1.08	0.93
F	0.43	0.16	0.04	0.37	0.19	0.39	0.33	0.39	0.41	0.57
Cl	0.03	0.02	0.05	0.02	0.02	0.00	0.05	0.04	0.02	0.02
Total (Inc. F & Cl)	96.21	95.65	96.56	96.13	95.26	96.32	96.25	96.91	96.56	96.66
O=-F	-0.18	-0.07	-0.02	-0.16	-0.08	-0.16	-0.14	-0.16	-0.17	-0.24
O=-Cl	-0.01	0.00	-0.01	0.00	0.00	0.00	-0.01	-0.01	0.00	0.00
Total	96.03	95.58	96.53	95.96	95.17	96.15	96.10	96.74	96.38	96.41
Si	6.47	6.54	6.41	6.43	6.45	6.48	6.51	6.42	6.39	6.41
Ti	0.15	0.11	0.13	0.11	0.09	0.09	0.09	0.08	0.10	0.08
Al	2.18	2.11	2.32	2.29	2.47	2.29	2.21	2.33	2.37	2.40
Cr	0.01	0.00	0.00	0.00	0.00	0.00	0.01	0.00	0.00	0.00
Fe^{3+}	0.10	0.19	0.18	0.12	0.06	0.17	0.18	0.22	0.19	0.24
Fe^{2+}	2.08	1.98	1.97	2.00	1.99	1.93	1.94	1.89	1.92	1.94
Mn	0.03	0.02	0.01	0.02	0.02	0.02	0.02	0.02	0.01	0.03
Mg	2.01	2.09	2.02	2.03	1.93	2.06	2.08	2.07	2.05	1.95
Ca	1.92	1.91	1.85	1.98	1.90	1.88	1.91	1.93	1.91	1.87
Na	0.37	0.30	0.36	0.32	0.34	0.34	0.31	0.34	0.35	0.36
K	0.22	0.21	0.24	0.22	0.20	0.20	0.19	0.20	0.21	0.18
Cation Total	15.53	15.46	15.51	15.52	15.46	15.46	15.45	15.50	15.50	15.46
F	0.21	0.08	0.02	0.18	0.09	0.19	0.16	0.19	0.20	0.27
Cl	0.01	0.01	0.01	0.00	0.00	0.00	0.01	0.01	0.01	0.01
X_{Mg}	0.49	0.51	0.51	0.50	0.49	0.52	0.52	0.52	0.52	0.50

Table 4-5. Representative analyses of matrix amphibole in TM11020803A from Niban Rock

Exposure	Niban Rock	Niban Rock	Niban Rock	Niban Rock	Niban Rock	Niban Rock	Niban Rock	Niban Rock	Niban Rock	Niban Rock
Corona	Free	Free	Free	Free	Free	Free	Free	Free	Free	Free
Sample	TM11020803A	TM11020803A	TM11020803A	TM11020803A	TM11020803A	TM11020803A	TM11020803A	TM11020803A	TM11020803A	TM11020803A
Analysis Point	TM11020803A_amp005	TM11020803A_amp007	TM11020803A_amp008	TM11020803A_amp013	TM11020803A_amp015	TM11020803A_amp021	TM11020803A_amp068	TM11020803A_amp075	TM11020803A_amp093	TM11020803A_amp097
SiO_2	42.51	41.74	41.29	41.14	41.54	41.76	42.36	41.96	42.20	42.30
TiO_2	0.91	1.07	1.34	0.98	0.99	1.01	0.66	0.97	1.00	0.86
Al_2O_3	13.15	12.75	12.59	13.06	13.43	13.07	12.94	12.97	13.08	13.31
Cr_2O_3	0.00	0.00	0.04	0.03	0.02	0.02	0.01	0.02	0.00	0.00
FeO	20.88	20.85	20.91	20.79	21.01	20.41	20.73	21.51	20.64	21.07
MnO	0.15	0.17	0.10	0.17	0.18	0.20	0.13	0.13	0.18	0.13
MgO	7.05	7.32	7.18	7.19	7.44	7.33	7.73	7.22	7.33	7.44
CaO	11.32	11.00	10.87	11.63	11.88	10.83	11.47	10.62	11.18	10.53
Na_2O	1.26	1.25	1.46	1.40	1.45	1.37	1.25	1.24	1.38	1.36
K_2O	0.82	0.81	0.91	0.63	0.58	0.86	0.76	0.71	0.80	0.69
F	0.04	0.03	0.01	0.00	0.09	0.00	0.16	0.09	0.00	0.00
Cl	0.04	0.07	0.04	0.03	0.00	0.02	0.06	0.02	0.00	0.06
Total (Inc. F & Cl)	98.12	97.05	96.75	97.04	98.60	96.89	98.25	97.44	97.79	97.75
O=-F	-0.02	-0.01	-0.01	0.00	-0.04	0.00	-0.07	-0.04	0.00	0.00
O=-Cl	-0.01	-0.02	-0.01	-0.01	0.00	0.00	-0.01	0.00	0.00	-0.01
Total	98.09	97.02	96.73	97.03	98.56	96.89	98.17	97.40	97.79	97.74
Si	6.40	6.35	6.33	6.27	6.23	6.35	6.36	6.34	6.37	6.35
Ti	0.10	0.12	0.15	0.11	0.11	0.12	0.07	0.11	0.11	0.10
Al	2.33	2.29	2.27	2.35	2.37	2.34	2.29	2.31	2.33	2.36
Cr	0.00	0.00	0.01	0.00	0.00	0.00	0.00	0.00	0.00	0.00
Fe^{3+}	0.33	0.49	0.39	0.48	0.54	0.42	0.52	0.60	0.38	0.55
Fe^{2+}	2.30	2.16	2.29	2.17	2.10	2.18	2.08	2.12	2.22	2.10
Mn	0.02	0.02	0.01	0.02	0.02	0.03	0.02	0.02	0.02	0.02
Mg	1.58	1.66	1.64	1.63	1.66	1.66	1.73	1.63	1.65	1.67
Ca	1.83	1.79	1.78	1.90	1.91	1.76	1.84	1.72	1.81	1.69
Na	0.37	0.37	0.43	0.41	0.42	0.40	0.36	0.36	0.40	0.40
K	0.16	0.16	0.18	0.12	0.11	0.17	0.15	0.14	0.15	0.13
Cation Total	15.42	15.40	15.49	15.47	15.47	15.43	15.42	15.34	15.45	15.36
F	0.02	0.01	0.01	0.00	0.04	0.00	0.08	0.04	0.00	0.00
Cl	0.01	0.02	0.01	0.01	0.00	0.00	0.02	0.00	0.00	0.01
X_{Mg}	0.41	0.43	0.42	0.43	0.44	0.43	0.45	0.43	0.43	0.44

Table 4-6. Representative analyses of matrix amphibole in I-554 from Kasumi Rock

Exposure	Kasumi Rock	Kasumi Rock	Kasumi Rock	Kasumi Rock	Kasumi Rock	Kasumi Rock	Kasumi Rock	Kasumi Rock	Kasumi Rock	Kasumi Rock
Corona	Free	Free	Free	Free	Free	Free	Free	Free	Free	Free
Sample	I-554	I-554	I-554	I-554	I-554	I-554	I-554	I-554	I-554	I-554
Analysis Point	I554A1_amp026	I554A1_amp028	I554A1_amp032	I554A1_amp037	I554A1_amp038	I554A1_amp041	I554A1_amp047	I554A1_amp050	I554A1_amp055	I554A1_amp058
SiO_2	43.12	43.21	42.51	43.11	43.70	43.45	42.98	42.16	42.16	42.40
TiO_2	1.05	1.12	1.23	1.28	0.99	0.93	1.20	1.09	0.85	1.24
Al_2O_3	11.41	11.07	11.26	10.72	10.68	10.56	11.03	11.28	12.00	11.92
Cr_2O_3	0.02	0.07	0.00	0.01	0.00	0.00	0.00	0.03	0.07	0.00
FeO	17.57	17.51	17.65	17.01	18.07	17.68	18.34	17.39	16.62	17.44
MnO	0.58	0.59	0.40	0.32	0.34	0.29	0.32	0.31	0.30	0.29
MgO	10.44	10.72	10.29	10.30	10.81	10.63	10.74	10.24	9.96	10.06
CaO	9.65	9.41	10.59	10.63	9.79	9.70	9.75	10.71	11.03	10.82
Na_2O	1.63	1.52	1.72	1.53	1.53	1.63	1.45	1.58	1.82	1.77
K_2O	0.52	0.45	0.60	0.51	0.45	0.47	0.49	0.51	0.51	0.45
F	0.06	0.00	0.00	0.00	0.00	0.02	0.04	0.24	0.00	0.02
Cl	0.04	0.10	0.05	0.03	0.04	0.00	0.02	0.01	0.05	0.03
Total (Inc. F & Cl)	96.08	95.78	96.30	95.45	96.38	95.36	96.36	95.54	95.39	96.42
O=-F	-0.03	0.00	0.00	0.00	0.00	-0.01	-0.02	-0.10	0.00	-0.01
O=-Cl	-0.01	-0.02	-0.01	-0.01	-0.01	0.00	0.00	0.00	-0.01	-0.01
Total	96.04	95.76	96.29	95.44	96.37	95.35	96.34	95.44	95.37	96.41
Si	6.45	6.48	6.40	6.53	6.51	6.55	6.42	6.40	6.41	6.37
Ti	0.12	0.13	0.14	0.15	0.11	0.11	0.14	0.12	0.10	0.14
Al	2.01	1.96	2.00	1.91	1.88	1.88	1.94	2.02	2.15	2.11
Cr	0.00	0.01	0.00	0.00	0.00	0.00	0.00	0.00	0.01	0.00
Fe^{3+}	0.82	0.82	0.67	0.52	0.83	0.74	0.90	0.69	0.44	0.57
Fe^{2+}	1.38	1.38	1.55	1.63	1.43	1.49	1.39	1.52	1.67	1.62
Mn	0.07	0.08	0.05	0.04	0.04	0.04	0.04	0.04	0.04	0.04
Mg	2.33	2.40	2.31	2.32	2.40	2.39	2.39	2.32	2.26	2.25
Ca	1.55	1.51	1.71	1.72	1.56	1.57	1.56	1.74	1.80	1.74
Na	0.47	0.44	0.50	0.45	0.44	0.48	0.42	0.47	0.54	0.51
K	0.10	0.09	0.11	0.10	0.08	0.09	0.09	0.10	0.10	0.09
Cation Total	15.30	15.27	15.44	15.38	15.29	15.32	15.28	15.41	15.51	15.45
F	0.03	0.00	0.00	0.00	0.00	0.01	0.02	0.12	0.00	0.01
Cl	0.01	0.03	0.01	0.01	0.01	0.00	0.01	0.00	0.01	0.01
X_{Mg}	0.63	0.63	0.60	0.59	0.63	0.62	0.63	0.60	0.57	0.58

Table 4-7. Representative analyses of matrix amphibole in TM11021006A from Tenmondai Rock.

Exposure	Tenmondai Rock	Tenmondai Rock	Tenmondai Rock	Tenmondai Rock	Tenmondai Rock	Tenmondai Rock	Tenmondai Rock	Tenmondai Rock	Tenmondai Rock	Tenmondai Rock
Corona	Free	Free	Free	Free	Free	Free	Free	Free	Free	Free
Sample	TM11021006A	TM11021006A	TM11021006A	TM11021006A	TM11021006A	TM11021006A	TM11021006A	TM11021006A	TM11021006A	TM11021006A
Analysis Point	Tenmon_amp024	Tenmon_amp025	Tenmon_amp038	Tenmon_amp042	Tenmon_amp047	Tenmon_amp057	Tenmon_amp069	Tenmon_amp075	Tenmon_amp077	Tenmon_amp084
SiO_2	41.16	41.26	41.36	41.75	41.66	41.51	40.84	41.41	41.45	41.24
TiO_2	1.80	1.33	1.83	1.60	1.87	1.63	2.14	2.11	1.89	1.91
Al_2O_3	13.89	14.12	14.15	13.96	13.78	13.88	14.15	14.06	13.70	13.77
Cr_2O_3	0.02	0.01	0.00	0.07	0.01	0.10	0.05	0.04	0.02	0.00
FeO	14.55	14.34	14.02	14.10	14.74	13.42	14.03	13.77	13.74	13.81
MnO	0.21	0.23	0.26	0.25	0.23	0.25	0.23	0.30	0.20	0.36
MgO	12.06	12.12	11.92	11.84	11.98	11.81	11.33	11.80	11.56	11.22
CaO	9.98	10.21	10.30	10.32	10.62	10.20	10.70	10.28	10.52	10.66
Na_2O	2.28	2.23	2.28	2.18	2.15	2.29	2.28	2.39	2.17	2.03
K_2O	0.79	0.63	0.59	0.77	0.73	0.58	0.79	0.75	0.71	0.66
F	0.14	0.00	0.07	0.13	0.04	0.11	0.09	0.11	0.00	0.04
Cl	0.09	0.05	0.07	0.05	0.11	0.06	0.04	0.10	0.07	0.03
Total (Inc. F & Cl)	96.97	96.53	96.85	97.04	97.97	95.83	96.77	97.13	96.21	95.72
O=-F	-0.06	0.00	-0.03	-0.05	-0.02	-0.05	-0.04	-0.05	0.00	-0.02
O=-Cl	-0.02	-0.01	-0.02	-0.01	-0.02	-0.01	-0.01	-0.02	-0.01	-0.01
Total	96.89	96.52	96.80	96.98	97.93	95.77	96.72	97.06	96.19	95.69
Si	6.08	6.09	6.11	6.16	6.10	6.19	6.08	6.12	6.18	6.18
Ti	0.20	0.15	0.20	0.18	0.21	0.18	0.24	0.23	0.21	0.22
Al	2.42	2.46	2.46	2.43	2.38	2.44	2.48	2.45	2.41	2.43
Cr	0.00	0.00	0.00	0.01	0.00	0.01	0.01	0.01	0.00	0.00
Fe^{3+}	0.68	0.74	0.57	0.54	0.64	0.50	0.41	0.49	0.44	0.41
Fe^{2+}	1.12	1.03	1.16	1.20	1.17	1.17	1.34	1.22	1.28	1.33
Mn	0.03	0.03	0.03	0.03	0.03	0.03	0.03	0.04	0.03	0.05
Mg	2.66	2.67	2.62	2.60	2.61	2.62	2.52	2.60	2.57	2.51
Ca	1.58	1.62	1.63	1.63	1.67	1.63	1.71	1.63	1.68	1.71
Na	0.65	0.64	0.65	0.62	0.61	0.66	0.66	0.69	0.63	0.59
K	0.15	0.12	0.11	0.14	0.14	0.11	0.15	0.14	0.13	0.13
Cation Total	15.57	15.54	15.55	15.56	15.56	15.54	15.63	15.59	15.57	15.54
F	0.07	0.00	0.03	0.06	0.02	0.05	0.04	0.05	0.00	0.02
Cl	0.02	0.01	0.02	0.01	0.03	0.02	0.01	0.03	0.02	0.01
X_{Mg}	0.70	0.72	0.69	0.68	0.69	0.69	0.65	0.68	0.67	0.65

Table 4-8. Representative analyses of matrix amphibole in I-008 from Akarui Point.

Exposure	Akarui Point	Akarui Point	Akarui Point	Akarui Point	Akarui Point	Akarui Point	Akarui Point	Akarui Point	Akarui Point	Akarui Point
Corona	Bearing	Bearing	Bearing	Bearing	Bearing	Bearing	Bearing	Bearing	Bearing	Bearing
Sample	I-008	I-008	I-008	I-008	I-008	I-008	I-008	I-008	I-008	I-008
Analysis Point	I008_amp001 Line 010	I008_amp001 Line 014	I008_amp001 Line 018	I008_amp001 Line 020	I008_amp001 Line 034	I008_amp001 Line 042	I008_amp001 Line 046	I008_amp001 Line 071	I008_amp001 Line 077	I008_amp001 Line 080
SiO_2	42.81	42.65	43.03	43.46	43.14	43.64	43.17	43.72	43.26	43.95
TiO_2	0.12	0.12	0.11	0.16	0.11	0.15	0.14	0.20	0.16	0.21
Al_2O_3	15.84	15.96	15.83	16.03	15.71	15.94	15.83	15.99	15.84	14.91
Cr_2O_3	0.06	0.03	0.06	0.10	0.14	0.03	0.09	0.14	0.13	0.07
FeO	7.37	7.43	7.05	7.35	6.81	6.84	6.74	5.89	5.65	5.61
MnO	0.20	0.16	0.15	0.15	0.21	0.12	0.12	0.10	0.07	0.13
MgO	15.91	16.05	16.23	16.22	16.21	16.54	16.74	16.60	17.02	17.64
CaO	11.26	11.00	10.64	11.17	10.95	10.97	11.01	11.38	11.08	11.54
Na_2O	2.05	2.10	1.92	2.13	2.38	2.14	2.10	2.18	2.23	2.12
K_2O	0.32	0.33	0.33	0.38	0.31	0.37	0.40	0.34	0.34	0.28
F	0.20	0.21	0.15	0.16	0.14	0.19	0.12	0.22	0.20	0.22
Cl	0.14	0.14	0.11	0.11	0.10	0.09	0.10	0.07	0.07	0.07
Total (Inc. F & Cl)	96.25	96.18	95.60	97.42	96.20	97.01	96.57	96.84	96.06	96.73
O=-F	-0.08	-0.09	-0.06	-0.07	-0.06	-0.08	-0.05	-0.09	-0.08	-0.09
O=-Cl	-0.03	-0.03	-0.03	-0.02	-0.02	-0.02	-0.02	-0.02	-0.02	-0.02
Total	96.14	96.06	95.51	97.33	96.12	96.91	96.50	96.73	95.96	96.62
Si	6.14	6.13	6.19	6.16	6.19	6.20	6.16	6.21	6.19	6.24
Ti	0.01	0.01	0.01	0.02	0.01	0.02	0.01	0.02	0.02	0.02
Al	2.68	2.70	2.68	2.68	2.66	2.67	2.66	2.68	2.67	2.49
Cr	0.01	0.00	0.01	0.01	0.02	0.00	0.01	0.02	0.02	0.01
Fe^{3+}	0.60	0.60	0.54	0.55	0.48	0.49	0.53	0.40	0.41	0.49
Fe^{2+}	0.28	0.29	0.31	0.32	0.34	0.33	0.27	0.30	0.27	0.18
Mn	0.02	0.02	0.02	0.02	0.03	0.01	0.01	0.01	0.01	0.02
Mg	3.40	3.44	3.48	3.43	3.47	3.50	3.56	3.52	3.63	3.73
Ca	1.73	1.69	1.64	1.70	1.68	1.67	1.68	1.73	1.70	1.75
Na	0.57	0.59	0.54	0.58	0.66	0.59	0.58	0.60	0.62	0.58
K	0.06	0.06	0.06	0.07	0.06	0.07	0.07	0.06	0.06	0.05
Cation Total	15.51	15.53	15.48	15.53	15.58	15.54	15.55	15.55	15.59	15.56
F	0.09	0.10	0.07	0.07	0.07	0.08	0.05	0.10	0.09	0.10
Cl	0.03	0.03	0.03	0.03	0.02	0.02	0.02	0.02	0.02	0.02
X_{Mg}	0.92	0.92	0.92	0.91	0.91	0.91	0.93	0.92	0.93	0.96

Table 4-9. Representative analyses of matrix amphibole in I-030 from Akarui Point.

Exposure	Akarui Point	Akarui Point	Akarui Point	Akarui Point	Akarui Point	Akarui Point	Akarui Point	Akarui Point	Akarui Point	Akarui Point
Corona	Bearing	Bearing	Bearing	Bearing	Bearing	Bearing	Bearing	Bearing	Bearing	Bearing
Sample	I-030	I-030	I-030	I-030	I-030	I-030	I-030	I-030	I-030	I-030
Analysis Point	I030_amp005	I030_amp003 Line 003	I030_amp003 Line 005	I030_amp003 Line 006	I030_amp003 Line 007	I030_amp003 Line 008	I030_amp003 Line 009	I030_amp003 Line 010	I030_amp003 Line 011	I030_amp003 Line 012
SiO_2	43.08	43.65	42.48	43.45	44.12	43.55	43.00	43.28	43.06	43.76
TiO_2	0.40	0.47	0.48	0.51	0.48	0.59	0.56	0.49	0.50	0.55
Al_2O_3	14.69	14.39	14.17	14.59	14.30	14.02	14.16	14.12	14.56	14.38
Cr_2O_3	0.00	0.04	0.03	0.04	0.00	0.00	0.03	0.09	0.05	0.03
FeO	10.84	10.50	10.48	10.50	9.85	10.27	10.48	10.02	10.74	10.36
MnO	0.18	0.21	0.14	0.14	0.14	0.21	0.21	0.13	0.17	0.20
MgO	15.06	14.80	14.89	15.02	14.88	14.97	14.94	14.76	15.17	14.98
CaO	10.12	10.30	10.44	10.31	10.17	10.74	10.43	10.58	10.46	9.91
Na_2O	1.95	2.09	2.07	2.17	2.01	1.95	1.92	1.97	2.13	1.94
K_2O	0.42	0.45	0.48	0.47	0.49	0.38	0.50	0.45	0.39	0.34
F	0.00	0.00	0.00	0.00	0.04	0.02	0.02	0.00	0.03	0.00
Cl	0.35	0.25	0.37	0.37	0.41	0.32	0.26	0.25	0.33	0.30
Total (Inc. F & Cl)	97.18	97.15	96.08	97.73	96.93	97.08	96.62	96.14	97.69	96.77
O=-F	0.00	0.00	0.00	0.00	-0.02	-0.01	-0.01	0.00	-0.01	0.00
O=-Cl	-0.08	-0.06	-0.08	-0.08	-0.09	-0.07	-0.06	-0.06	-0.07	-0.07
Total	97.10	97.10	96.00	97.64	96.82	97.00	96.56	96.09	97.61	96.71
Si	6.18	6.27	6.18	6.22	6.34	6.26	6.21	6.27	6.16	6.29
Ti	0.04	0.05	0.05	0.05	0.05	0.06	0.06	0.05	0.05	0.06
Al	2.48	2.43	2.43	2.46	2.42	2.37	2.41	2.41	2.46	2.44
Cr	0.00	0.00	0.00	0.00	0.00	0.00	0.00	0.01	0.01	0.00
Fe^{3+}	0.81	0.68	0.77	0.70	0.58	0.74	0.78	0.67	0.80	0.67
Fe^{2+}	0.49	0.58	0.50	0.56	0.60	0.49	0.49	0.54	0.49	0.57
Mn	0.02	0.02	0.02	0.02	0.02	0.03	0.03	0.02	0.02	0.02
Mg	3.22	3.17	3.23	3.20	3.19	3.20	3.22	3.19	3.24	3.21
Ca	1.56	1.58	1.63	1.58	1.57	1.65	1.61	1.64	1.60	1.53
Na	0.54	0.58	0.58	0.60	0.56	0.54	0.54	0.55	0.59	0.54
K	0.08	0.08	0.09	0.09	0.09	0.07	0.09	0.08	0.07	0.06
Cation Total	15.44	15.45	15.50	15.49	15.43	15.43	15.45	15.45	15.48	15.40
F	0.00	0.00	0.00	0.00	0.02	0.01	0.01	0.00	0.01	0.00
Cl	0.09	0.06	0.09	0.09	0.10	0.08	0.06	0.06	0.08	0.07
X_{Mg}	0.87	0.85	0.87	0.85	0.84	0.87	0.87	0.85	0.87	0.85

Table 4-10. Representative analyses of matrix amphibole in I-518 from East Ongul Island.

Exposure	Ongul Island	Ongul Island	Ongul Island	Ongul Island	Ongul Island	Ongul Island	Ongul Island	Ongul Island	Ongul Island	Ongul Island
Corona	Bearing	Bearing	Bearing	Bearing	Bearing	Bearing	Bearing	Bearing	Bearing	Bearing
Sample	I-518	I-518	I-518	I-518	I-518	I-518	I-518	I-518	I-518	I-518
Analysis Point	I518_amp001 Line 006	I518_amp001 Line 022	I518_amp001 Line 023	I518_amp001 Line 025	I518_amp001 Line 050	I518_amp001 Line 051	I518_amp001 Line 073	I518_amp001 Line 074	I518_amp001 Line 095	I518_amp001 Line 096
SiO_2	41.00	41.02	40.42	40.01	41.08	41.18	40.67	40.58	40.23	40.25
TiO_2	0.12	0.14	0.09	0.15	0.20	0.20	0.19	0.12	0.18	0.14
Al_2O_3	14.89	15.55	15.67	15.71	15.19	15.31	15.21	15.52	15.53	15.33
Cr_2O_3	0.00	0.00	0.00	0.01	0.06	0.00	0.02	0.03	0.00	0.00
FeO	12.38	12.50	12.46	12.42	12.25	12.27	12.49	12.12	12.45	12.31
MnO	0.18	0.16	0.23	0.15	0.21	0.15	0.23	0.21	0.12	0.13
MgO	12.33	11.99	11.90	12.31	12.55	12.41	12.37	12.04	11.92	12.38
CaO	11.06	10.75	10.87	11.26	10.98	10.52	10.78	11.17	11.23	10.97
Na_2O	2.05	2.00	1.99	2.12	1.99	1.83	1.97	2.00	1.86	1.94
K_2O	1.29	1.42	1.17	1.22	1.39	1.36	1.26	1.17	1.33	1.32
F	0.33	0.29	0.34	0.31	0.38	0.29	0.35	0.34	0.36	0.39
Cl	1.05	1.15	1.13	1.12	1.09	1.12	1.10	1.17	1.17	1.15
Total (Inc. F & Cl)	96.68	96.94	96.25	96.78	97.36	96.63	96.63	96.47	96.37	96.30
O=-F	-0.14	-0.12	-0.14	-0.13	-0.16	-0.12	-0.15	-0.14	-0.15	-0.16
O=-Cl	-0.24	-0.26	-0.25	-0.25	-0.25	-0.25	-0.25	-0.26	-0.26	-0.26
Total	96.30	96.56	95.85	96.40	96.96	96.25	96.23	96.07	95.95	95.87
Si	6.13	6.12	6.07	5.98	6.10	6.13	6.07	6.08	6.05	6.04
Ti	0.01	0.02	0.01	0.02	0.02	0.02	0.02	0.01	0.02	0.02
Al	2.63	2.74	2.77	2.77	2.66	2.69	2.68	2.74	2.75	2.71
Cr	0.00	0.00	0.00	0.00	0.01	0.00	0.00	0.00	0.00	0.00
Fe^{3+}	0.50	0.46	0.57	0.61	0.56	0.58	0.64	0.50	0.52	0.62
Fe^{2+}	1.05	1.10	1.00	0.94	0.96	0.95	0.92	1.02	1.05	0.92
Mn	0.02	0.02	0.03	0.02	0.03	0.02	0.03	0.03	0.01	0.02
Mg	2.75	2.67	2.66	2.74	2.78	2.75	2.75	2.69	2.67	2.77
Ca	1.77	1.72	1.75	1.80	1.75	1.68	1.72	1.79	1.81	1.76
Na	0.60	0.58	0.58	0.61	0.57	0.53	0.57	0.58	0.54	0.56
K	0.25	0.27	0.22	0.23	0.26	0.26	0.24	0.22	0.25	0.25
Cation Total	15.71	15.69	15.65	15.73	15.69	15.61	15.65	15.68	15.69	15.68
F	0.16	0.14	0.16	0.15	0.18	0.14	0.17	0.16	0.17	0.19
Cl	0.27	0.29	0.29	0.29	0.28	0.29	0.28	0.30	0.30	0.30
X_{Mg}	0.72	0.71	0.73	0.74	0.74	0.74	0.75	0.72	0.72	0.75

Table 4-11. Representative analyses of matrix amphibole in TM11021501E from Langhovde.

Exposure	Langhovde	Langhovde	Langhovde	Langhovde	Langhovde	Langhovde	Langhovde	Langhovde	Langhovde	Langhovde
Corona	Free	Free	Free	Free	Free	Free	Free	Free	Free	Free
Sample	TM11021501E	TM11021501E	TM11021501E	TM11021501E	TM11021501E	TM11021501E	TM11021501E	TM11021501E	TM11021501E	TM11021501E
Analysis Point	Lang_amp001 Line 005	Lang_amp001 Line 010	Lang_amp001 Line 015	Lang_amp002 Line 009	Lang_amp002 Line 013	Lang_amp002 Line 018	Lang_amp003 Line 007	Lang_amp003 Line 011	Lang_amp003 Line 013	Lang_amp003 Line 016
SiO_2	38.32	38.12	38.49	38.54	38.63	38.83	38.74	38.31	37.51	38.55
TiO_2	1.58	1.79	1.61	1.81	1.82	1.73	1.64	1.56	1.65	1.44
Al_2O_3	14.58	14.60	14.86	14.66	14.64	14.55	14.46	14.54	14.69	14.92
Cr_2O_3	0.00	0.02	0.04	0.02	0.02	0.05	0.00	0.02	0.04	0.00
FeO	17.44	17.22	17.19	17.75	17.11	16.96	16.65	17.43	17.41	17.34
MnO	0.34	0.30	0.29	0.31	0.41	0.29	0.38	0.35	0.40	0.33
MgO	9.26	9.21	9.20	9.29	9.20	9.10	9.17	9.34	9.11	8.88
CaO	10.63	11.05	11.08	10.98	11.16	11.12	11.10	11.03	11.44	11.12
Na_2O	1.86	1.83	1.87	1.95	1.96	1.85	1.80	1.99	1.89	1.84
K_2O	1.53	1.75	1.63	1.62	1.73	1.74	1.72	1.61	1.67	1.71
F	0.35	0.37	0.29	0.40	0.30	0.30	0.33	0.40	0.56	0.37
Cl	1.63	1.62	1.62	1.78	1.51	1.83	1.84	1.64	1.61	1.62
Total (Inc. F & Cl)	97.51	97.88	98.16	99.10	98.50	98.35	97.82	98.22	97.96	98.11
O=-F	-0.15	-0.16	-0.12	-0.17	-0.13	-0.13	-0.14	-0.17	-0.23	-0.16
O=-Cl	-0.37	-0.37	-0.36	-0.40	-0.34	-0.41	-0.41	-0.37	-0.36	-0.37
Total	96.99	97.35	97.68	98.53	98.03	97.81	97.26	97.68	97.36	97.59
Si	5.88	5.86	5.88	5.85	5.89	5.95	5.96	5.86	5.78	5.91
Ti	0.18	0.21	0.19	0.21	0.21	0.20	0.19	0.18	0.19	0.17
Al	2.64	2.64	2.67	2.62	2.63	2.63	2.62	2.62	2.67	2.69
Cr	0.00	0.00	0.00	0.00	0.00	0.01	0.00	0.00	0.01	0.00
Fe^{3+}	0.70	0.58	0.56	0.63	0.49	0.41	0.45	0.64	0.67	0.51
Fe^{2+}	1.54	1.64	1.63	1.62	1.69	1.76	1.70	1.59	1.58	1.72
Mn	0.04	0.04	0.04	0.04	0.05	0.04	0.05	0.04	0.05	0.04
Mg	2.12	2.11	2.09	2.10	2.09	2.08	2.10	2.13	2.09	2.03
Ca	1.75	1.82	1.81	1.79	1.82	1.83	1.83	1.81	1.89	1.83
Na	0.55	0.54	0.55	0.57	0.58	0.55	0.54	0.59	0.56	0.55
K	0.30	0.34	0.32	0.31	0.34	0.34	0.34	0.31	0.33	0.33
Cation Total	15.70	15.77	15.75	15.76	15.80	15.78	15.76	15.78	15.81	15.77
F	0.17	0.18	0.14	0.19	0.15	0.15	0.16	0.20	0.27	0.18
Cl	0.43	0.43	0.42	0.46	0.39	0.48	0.48	0.43	0.43	0.42
X_{Mg}	0.58	0.56	0.56	0.56	0.55	0.54	0.55	0.57	0.57	0.54

Table 4-12. Representative analyses of matrix amphibole in 92010203A from Skarvsnes.

Exposure	Skarvsnes	Skarvsnes	Skarvsnes	Skarvsnes	Skarvsnes	Skarvsnes	Skarvsnes	Skarvsnes	Skarvsnes	Skarvsnes
Corona	Free	Free	Free	Free	Free	Free	Free	Free	Free	Free
Sample	92010203 A	92010203 A	92010203 A	92010203 A	92010203 A	92010203 A	92010203 A	92010203 A	92010203 A	92010203 A
Analysis Point	Skarvsnes_ amp006 Line 013	Skarvsnes_ amp006 Line 022	Skarvsnes_ amp006 Line 023	Skarvsnes_ amp001 Line 002	Skarvsnes_ amp001 Line 003	Skarvsnes_ amp001 Line 008	Skarvsnes_ amp001 Line 009	Skarvsnes_ amp002 Line 006	Skarvsnes_ amp006 Line 022	Skarvsnes_ amp006 Line 047
SiO_2	37.71	37.75	37.75	37.46	38.03	37.74	38.17	37.60	37.75	37.66
TiO_2	2.19	2.47	2.21	2.33	2.09	2.23	2.21	2.02	2.47	2.37
Al_2O_3	15.06	15.40	15.41	14.92	14.75	14.61	14.52	14.64	15.40	14.73
Cr_2O_3	0.01	0.00	0.02	0.10	0.00	0.01	0.00	0.05	0.00	0.00
FeO	18.76	18.74	18.97	19.06	18.58	19.14	19.09	19.13	18.74	18.47
MnO	0.14	0.02	0.11	0.11	0.13	0.12	0.11	0.16	0.02	0.13
MgO	7.02	7.02	6.99	7.38	7.34	6.82	7.38	7.13	7.02	7.18
CaO	11.67	11.84	11.94	11.72	11.89	11.18	11.58	11.32	11.84	11.72
Na_2O	0.75	0.72	0.71	0.79	0.86	0.82	0.82	0.85	0.72	0.67
K_2O	3.49	3.25	3.38	3.40	3.42	3.44	3.59	3.59	3.25	3.48
F	0.20	0.33	0.15	0.32	0.33	0.33	0.40	0.14	0.33	0.38
Cl	0.17	0.16	0.16	0.11	0.11	0.16	0.17	0.14	0.16	0.08
Total (Inc. F & Cl)	97.16	97.70	97.79	97.70	97.54	96.59	98.04	96.77	97.70	96.87
O=-F	-0.09	-0.14	-0.06	-0.13	-0.14	-0.14	-0.17	-0.06	-0.14	-0.16
O=-Cl	-0.04	-0.04	-0.04	-0.03	-0.03	-0.04	-0.04	-0.03	-0.04	-0.02
Total	97.04	97.52	97.70	97.54	97.38	96.41	97.83	96.67	97.52	96.70
Si	5.89	5.86	5.85	5.81	5.92	5.93	5.92	5.89	5.86	5.90
Ti	0.26	0.29	0.26	0.27	0.24	0.26	0.26	0.24	0.29	0.28
Al	2.77	2.82	2.81	2.73	2.70	2.71	2.65	2.70	2.82	2.72
Cr	0.00	0.00	0.00	0.01	0.00	0.00	0.00	0.01	0.00	0.00
Fe^{3+}	0.09	0.08	0.13	0.25	0.07	0.12	0.13	0.18	0.08	0.08
Fe^{2+}	2.36	2.35	2.32	2.22	2.35	2.39	2.35	2.33	2.35	2.34
Mn	0.02	0.00	0.01	0.01	0.02	0.02	0.01	0.02	0.00	0.02
Mg	1.63	1.62	1.61	1.71	1.70	1.60	1.71	1.67	1.62	1.68
Ca	1.95	1.97	1.98	1.95	1.98	1.88	1.92	1.90	1.97	1.97
Na	0.23	0.22	0.21	0.24	0.26	0.25	0.25	0.26	0.22	0.20
K	0.70	0.64	0.67	0.67	0.68	0.69	0.71	0.72	0.64	0.69
Cation Total	15.89	15.84	15.86	15.88	15.92	15.86	15.91	15.91	15.84	15.87
F	0.10	0.16	0.07	0.16	0.16	0.17	0.20	0.07	0.16	0.19
Cl	0.05	0.04	0.04	0.03	0.03	0.04	0.04	0.04	0.04	0.02
X_{Mg}	0.41	0.41	0.41	0.43	0.42	0.40	0.42	0.42	0.41	0.42

Table 4-13. Representative analyses of matrix amphibole in I-232 from Skallen.

Exposure	Skallen	Skallen	Skallen	Skallen	Skallen	Skallen	Skallen	Skallen	Skallen	Skallen
Corona	Free	Free	Free	Free	Free	Free	Free	Free	Free	Free
Sample	I-232	I-232	I-232	I-232	I-232	I-232	I-232	I-232	I-232	I-232
Analysis Point	I232_amp009	I232_amp011	I232_amp015	I232_amp018	I232_amp023	I232_amp029	I232_amp032	I232_amp041	I232_amp044	I232_amp049
SiO_2	41.29	40.59	40.90	41.41	41.49	40.72	40.93	41.44	40.37	41.26
TiO_2	1.92	1.96	1.93	2.06	2.27	2.27	2.30	1.99	2.08	2.19
Al_2O_3	14.52	14.55	14.14	14.06	14.40	14.39	14.45	14.82	14.66	14.33
Cr_2O_3	0.05	0.12	0.00	0.00	0.04	0.03	0.02	0.02	0.00	0.06
FeO	13.94	13.65	13.74	13.26	13.34	13.29	13.26	13.40	13.21	13.64
MnO	0.18	0.19	0.07	0.14	0.19	0.10	0.19	0.10	0.23	0.16
MgO	11.42	11.30	11.64	11.91	11.65	11.66	11.68	11.66	11.76	11.80
CaO	11.60	10.84	10.79	11.29	11.16	11.25	11.08	11.09	10.53	10.78
Na_2O	2.44	2.38	2.33	2.38	2.43	2.47	2.65	2.42	2.45	2.62
K_2O	1.07	1.11	0.96	0.98	1.12	1.10	1.04	1.07	0.97	1.03
F	0.23	0.18	0.21	0.21	0.21	0.00	0.32	0.36	0.16	0.24
Cl	0.25	0.19	0.25	0.17	0.16	0.14	0.17	0.12	0.15	0.22
Total (Inc. F & Cl)	98.88	97.05	96.95	97.87	98.46	97.42	98.09	98.47	96.58	98.33
O=-F	-0.09	-0.08	-0.09	-0.09	-0.09	0.00	-0.14	-0.15	-0.07	-0.10
O=-Cl	-0.06	-0.04	-0.06	-0.04	-0.04	-0.03	-0.04	-0.03	-0.03	-0.05
Total	98.73	96.93	96.81	97.74	98.33	97.39	97.92	98.29	96.47	98.18
Si	6.08	6.06	6.10	6.12	6.10	6.05	6.05	6.08	6.02	6.07
Ti	0.21	0.22	0.22	0.23	0.25	0.25	0.26	0.22	0.23	0.24
Al	2.52	2.56	2.48	2.45	2.50	2.52	2.52	2.56	2.58	2.49
Cr	0.01	0.01	0.00	0.00	0.00	0.00	0.00	0.00	0.00	0.01
Fe^{3+}	0.21	0.32	0.37	0.26	0.24	0.24	0.25	0.28	0.42	0.34
Fe^{2+}	1.50	1.38	1.34	1.37	1.40	1.41	1.39	1.36	1.23	1.34
Mn	0.02	0.02	0.01	0.02	0.02	0.01	0.02	0.01	0.03	0.02
Mg	2.51	2.51	2.59	2.62	2.55	2.58	2.58	2.55	2.61	2.59
Ca	1.83	1.73	1.72	1.79	1.76	1.79	1.76	1.74	1.68	1.70
Na	0.70	0.69	0.67	0.68	0.69	0.71	0.76	0.69	0.71	0.75
K	0.20	0.21	0.18	0.18	0.21	0.21	0.20	0.20	0.19	0.19
Cation Total	15.79	15.72	15.69	15.73	15.73	15.78	15.78	15.71	15.70	15.74
F	0.11	0.09	0.10	0.10	0.10	0.00	0.15	0.17	0.08	0.11
Cl	0.06	0.05	0.06	0.04	0.04	0.03	0.04	0.03	0.04	0.06
X_{Mg}	0.63	0.65	0.66	0.66	0.65	0.65	0.65	0.65	0.68	0.66

Table 4-14. Representative analyses of matrix amphibole in I-223 from Skallen.

Exposure	Skallen	Skallen	Skallen	Skallen	Skallen	Skallen	Skallen	Skallen	Skallen	Skallen
Corona	Bearing	Bearing	Bearing	Bearing	Bearing	Bearing	Bearing	Bearing	Bearing	Bearing
Sample	I-223	I-223	I-223	I-223	I-223	I-223	I-223	I-223	I-223	I-223
Analysis Point	Samp021	Samp024	Samp025	Samp029	Samp030	Samp048	Samp036	Samp037	Samp043	Samp046
SiO_2	40.82	41.11	41.12	41.20	41.32	40.76	41.28	40.63	41.19	40.72
TiO_2	2.56	2.77	2.84	2.98	2.69	2.55	3.19	2.58	2.71	2.91
Al_2O_3	11.72	11.31	11.51	11.26	11.09	11.44	11.11	11.51	10.93	11.41
Cr_2O_3	0.11	0.03	0.02	0.06	0.00	0.04	0.04	0.05	0.06	0.00
FeO	18.95	18.92	18.86	18.97	18.68	19.07	18.92	19.16	18.31	18.26
MnO	0.13	0.13	0.11	0.09	0.16	0.04	0.11	0.22	0.22	0.13
MgO	8.63	8.74	8.82	8.49	8.81	8.55	8.50	8.63	8.81	8.48
CaO	11.08	11.33	10.99	10.51	11.04	11.50	11.35	10.69	11.52	11.31
Na_2O	1.41	1.23	1.23	1.41	1.26	1.25	1.46	1.08	1.04	1.26
K_2O	2.03	1.91	1.93	1.80	1.84	2.02	1.96	1.93	2.01	1.93
F	0.20	0.48	0.32	0.30	0.40	0.13	0.23	0.00	0.22	0.46
Cl	0.17	0.15	0.11	0.13	0.14	0.15	0.16	0.18	0.16	0.16
Total (Inc. F & Cl)	97.82	98.12	97.85	97.20	97.45	97.48	98.29	96.66	97.18	97.03
O=-F	-0.08	-0.20	-0.13	-0.13	-0.17	-0.05	-0.10	0.00	-0.09	-0.19
O=-Cl	-0.04	-0.03	-0.02	-0.03	-0.03	-0.03	-0.04	-0.04	-0.04	-0.04
Total	97.70	97.89	97.69	97.04	97.24	97.39	98.16	96.62	97.05	96.80
Si	6.24	6.28	6.26	6.31	6.33	6.26	6.30	6.24	6.33	6.29
Ti	0.29	0.32	0.33	0.34	0.31	0.29	0.37	0.30	0.31	0.34
Al	2.11	2.04	2.07	2.03	2.00	2.07	2.00	2.08	1.98	2.08
Cr	0.01	0.00	0.00	0.01	0.00	0.01	0.01	0.01	0.01	0.00
Fe^{3+}	0.23	0.21	0.27	0.27	0.23	0.16	0.09	0.41	0.15	0.11
Fe^{2+}	2.19	2.21	2.13	2.16	2.16	2.29	2.32	2.05	2.20	2.25
Mn	0.02	0.02	0.01	0.01	0.02	0.01	0.01	0.03	0.03	0.02
Mg	1.97	1.99	2.00	1.94	2.01	1.96	1.93	1.98	2.02	1.95
Ca	1.81	1.85	1.79	1.73	1.81	1.89	1.86	1.76	1.90	1.87
Na	0.42	0.36	0.36	0.42	0.38	0.37	0.43	0.32	0.31	0.38
K	0.40	0.37	0.37	0.35	0.36	0.40	0.38	0.38	0.39	0.38
Cation Total	15.70	15.65	15.61	15.58	15.61	15.71	15.69	15.56	15.64	15.66
F	0.10	0.23	0.15	0.15	0.20	0.06	0.11	0.00	0.11	0.23
Cl	0.04	0.04	0.03	0.04	0.04	0.04	0.04	0.05	0.04	0.04
X_{Mg}	0.47	0.47	0.48	0.47	0.48	0.46	0.45	0.49	0.48	0.46

Table 4-15. Representative analyses of matrix amphibole in I-293 from Skallevikshalsen.

Exposure	Skallevikshalsen	Skallevikshalsen	Skallevikshalsen	Skallevikshalsen	Skallevikshalsen	Skallevikshalsen	Skallevikshalsen	Skallevikshalsen	Skallevikshalsen	Skallevikshalsen
Corona	Bearing	Bearing	Bearing	Bearing	Bearing	Bearing	Bearing	Bearing	Bearing	Bearing
Sample	I-293	I-293	I-293	I-293	I-293	I-293	I-293	I-293	I-293	I-293
Analysis Point	I293_amp005_mt	I293_amp006_mt	I293_amp008_mt	I293_amp011_mt	I293_amp016_mt	I293_amp018_mt	I293_amp020_mt	I293_amp024_mt	I293_amp027_mt	I293_amp029_mt
SiO_2	41.10	39.83	41.11	41.42	41.06	40.69	41.32	42.04	41.21	41.40
TiO_2	2.07	2.39	2.35	2.58	2.38	2.11	2.37	2.25	2.27	2.37
Al_2O_3	12.22	12.30	12.17	11.96	12.44	12.08	12.66	12.20	12.11	12.49
Cr_2O_3	0.00	0.07	0.00	0.00	0.02	0.00	0.02	0.03	0.02	0.04
FeO	17.46	17.81	17.92	18.10	18.18	17.08	17.46	17.53	17.60	17.39
MnO	0.12	0.17	0.12	0.12	0.09	0.16	0.17	0.16	0.11	0.10
MgO	8.79	8.71	8.71	8.70	8.69	8.69	8.78	9.03	8.99	9.05
CaO	11.63	11.37	11.43	11.55	11.32	11.61	11.56	11.55	11.79	11.89
Na_2O	1.50	1.52	1.46	1.37	1.58	1.30	1.43	1.54	1.48	1.57
K_2O	1.64	1.86	1.55	1.69	1.64	1.44	1.52	1.70	1.77	1.66
F	0.24	0.03	0.35	0.19	0.21	0.27	0.19	0.24	0.40	0.43
Cl	0.33	0.40	0.40	0.46	0.31	0.38	0.44	0.42	0.39	0.36
Total (Inc. F & Cl)	97.10	96.46	97.56	98.13	97.91	95.80	97.90	98.69	98.14	98.75
O=-F	-0.10	-0.01	-0.15	-0.08	-0.09	-0.11	-0.08	-0.10	-0.17	-0.18
O=-Cl	-0.08	-0.09	-0.09	-0.10	-0.07	-0.09	-0.10	-0.09	-0.09	-0.08
Total	96.93	96.35	97.32	97.95	97.75	95.61	97.72	98.49	97.88	98.49
Si	6.31	6.17	6.29	6.30	6.25	6.32	6.27	6.34	6.28	6.26
Ti	0.24	0.28	0.27	0.29	0.27	0.25	0.27	0.26	0.26	0.27
Al	2.21	2.25	2.19	2.14	2.23	2.21	2.26	2.17	2.18	2.23
Cr	0.00	0.01	0.00	0.00	0.00	0.00	0.00	0.00	0.00	0.00
Fe^{3+}	0.07	0.17	0.14	0.11	0.16	0.08	0.11	0.09	0.07	0.05
Fe^{2+}	2.17	2.14	2.15	2.19	2.15	2.13	2.10	2.12	2.18	2.15
Mn	0.01	0.02	0.01	0.02	0.01	0.02	0.02	0.02	0.01	0.01
Mg	2.01	2.01	1.98	1.97	1.97	2.01	1.99	2.03	2.04	2.04
Ca	1.91	1.89	1.87	1.88	1.85	1.93	1.88	1.87	1.93	1.93
Na	0.45	0.46	0.43	0.40	0.47	0.39	0.42	0.45	0.44	0.46
K	0.32	0.37	0.30	0.33	0.32	0.28	0.29	0.33	0.34	0.32
Cation Total	15.70	15.75	15.65	15.64	15.68	15.63	15.63	15.67	15.73	15.72
F	0.11	0.01	0.17	0.09	0.10	0.13	0.09	0.11	0.19	0.20
Cl	0.09	0.11	0.10	0.12	0.08	0.10	0.11	0.11	0.10	0.09
X_{Mg}	0.48	0.48	0.48	0.47	0.48	0.49	0.49	0.49	0.48	0.49

Table 4-16. Representative analyses of matrix amphibole in TM11010503E from Sudare Rock.

Exposure	Sudare Rock	Sudare Rock	Sudare Rock	Sudare Rock	Sudare Rock	Sudare Rock	Sudare Rock	Sudare Rock	Sudare Rock	Sudare Rock
Corona	Bearing	Bearing	Bearing	Bearing	Bearing	Bearing	Bearing	Bearing	Bearing	Bearing
Sample	TM11010503E	TM11010503E	TM11010503E	TM11010503E	TM11010503E	TM11010503E	TM11010503E	TM11010503E	TM11010503E	TM11010503E
Analysis Point	sudare_amp003	sudare_amp004	sudare_amp005	sudare_amp007	sudare_amp008	sudare_amp009	sudare_amp010	sudare_amp020	sudare_amp022	sudare_amp023
SiO_2	37.26	37.71	37.19	36.68	37.48	37.92	38.54	37.80	37.15	37.30
TiO_2	1.87	1.80	2.61	2.42	2.30	2.22	2.02	2.36	2.22	2.38
Al_2O_3	13.12	12.97	13.30	13.86	12.96	12.73	13.36	13.43	13.15	13.80
Cr_2O_3	0.04	0.05	0.11	0.05	0.03	0.05	0.00	0.05	0.12	0.04
FeO	20.03	19.80	20.15	19.97	20.25	19.42	19.23	19.78	21.02	20.64
MnO	0.15	0.14	0.11	0.08	0.02	0.12	0.10	0.09	0.14	0.10
MgO	6.92	7.11	6.91	6.53	6.77	7.17	7.42	6.51	6.12	6.42
CaO	11.42	11.04	11.13	11.41	11.57	11.25	11.33	11.51	11.12	11.26
Na_2O	0.98	1.01	1.10	1.00	0.91	1.12	1.21	1.11	0.89	0.94
K_2O	2.87	2.73	2.81	2.81	3.00	2.41	2.47	2.78	2.97	2.95
F	0.46	0.53	0.46	0.48	0.39	0.53	0.63	0.46	0.44	0.38
Cl	2.92	2.58	2.66	2.69	2.83	2.49	2.27	2.51	3.06	2.77
Total (Inc. F & Cl)	98.03	97.47	98.54	97.97	98.50	97.43	98.58	98.39	98.39	98.98
O=-F	-0.19	-0.22	-0.19	-0.20	-0.16	-0.22	-0.27	-0.20	-0.18	-0.16
O=-Cl	-0.66	-0.58	-0.60	-0.61	-0.64	-0.56	-0.51	-0.57	-0.69	-0.63
Total	97.18	96.67	97.74	97.16	97.70	96.65	97.80	97.63	97.51	98.19
Si	5.96	6.02	5.90	5.87	5.98	6.05	6.05	6.01	5.96	5.91
Ti	0.22	0.22	0.31	0.29	0.28	0.27	0.24	0.28	0.27	0.28
Al	2.47	2.44	2.49	2.61	2.44	2.39	2.47	2.52	2.49	2.58
Cr	0.00	0.01	0.01	0.01	0.00	0.01	0.00	0.01	0.01	0.00
Fe^{3+}	0.33	0.34	0.29	0.24	0.18	0.23	0.20	0.03	0.27	0.26
Fe^{2+}	2.35	2.30	2.39	2.43	2.52	2.36	2.33	2.60	2.55	2.48
Mn	0.02	0.02	0.02	0.01	0.00	0.02	0.01	0.01	0.02	0.01
Mg	1.65	1.69	1.63	1.56	1.61	1.71	1.74	1.54	1.46	1.52
Ca	1.96	1.89	1.89	1.96	1.98	1.92	1.91	1.96	1.91	1.91
Na	0.30	0.31	0.34	0.31	0.28	0.35	0.37	0.34	0.28	0.29
K	0.59	0.56	0.57	0.57	0.61	0.49	0.50	0.56	0.61	0.60
Cation Total	15.86	15.80	15.84	15.85	15.88	15.79	15.81	15.88	15.83	15.83
F	0.23	0.27	0.23	0.25	0.20	0.27	0.32	0.23	0.22	0.19
Cl	0.80	0.70	0.72	0.73	0.77	0.68	0.61	0.68	0.84	0.75
X_{Mg}	0.41	0.42	0.41	0.39	0.39	0.42	0.43	0.37	0.36	0.38

Table 4-17. Representative analyses of matrix amphibole in 93012101C from Berrodden.

Exposure	Berrodden	Berrodden	Berrodden	Berrodden	Berrodden	Berrodden	Berrodden	Berrodden	Berrodden	Berrodden
Corona	Bearing	Bearing	Bearing	Bearing	Bearing	Bearing	Bearing	Bearing	Bearing	Bearing
Sample	93012101 C	93012101 C	93012101 C	93012101 C	93012101 C	93012101 C	93012101 C	93012101 C	93012101 C	93012101 C
Analysis Point	Beru_amp 001	Beru_amp 002	Beru_amp 003	Beru_amp 005	Beru_amp 008	Beru_amp 010	Beru_amp 011	Beru_amp 012	Beru_amp 013	Beru_amp 014
SiO_2	39.89	40.03	39.72	39.65	39.53	39.65	39.36	39.38	39.46	39.70
TiO_2	2.90	2.72	2.64	3.06	3.11	2.90	3.18	3.07	3.17	2.85
Al_2O_3	13.08	13.25	13.10	13.34	13.57	13.30	13.44	13.08	13.28	13.37
Cr_2O_3	0.05	0.02	0.02	0.02	0.03	0.00	0.02	0.04	0.06	0.00
FeO	17.30	17.30	17.51	17.19	17.06	17.24	16.91	16.77	16.97	17.26
MnO	0.08	0.12	0.11	0.09	0.06	0.17	0.07	0.12	0.11	0.06
MgO	8.95	8.77	8.63	8.78	8.68	8.89	8.80	8.50	8.72	8.69
CaO	11.58	11.38	11.60	11.21	11.34	11.26	11.63	11.20	11.03	11.34
Na_2O	1.57	1.64	1.64	1.63	1.61	1.70	1.67	1.61	1.74	1.58
K_2O	1.72	1.76	1.80	1.74	1.74	1.89	1.90	1.88	1.91	1.77
F	0.16	0.15	0.09	0.20	0.18	0.18	0.13	0.15	0.16	0.18
Cl	0.38	0.40	0.39	0.40	0.37	0.39	0.40	0.38	0.38	0.41
Total (Inc. F & Cl)	97.64	97.53	97.25	97.31	97.27	97.57	97.51	96.17	97.00	97.20
O=-F	-0.07	-0.06	-0.04	-0.09	-0.08	-0.08	-0.06	-0.06	-0.07	-0.07
O=-Cl	-0.09	-0.09	-0.09	-0.09	-0.08	-0.09	-0.09	-0.09	-0.09	-0.09
Total	97.49	97.37	97.12	97.14	97.11	97.41	97.37	96.02	96.85	97.04
Si	6.09	6.11	6.10	6.07	6.05	6.06	6.03	6.11	6.06	6.09
Ti	0.33	0.31	0.30	0.35	0.36	0.33	0.37	0.36	0.37	0.33
Al	2.35	2.38	2.37	2.41	2.45	2.40	2.43	2.39	2.40	2.42
Cr	0.01	0.00	0.00	0.00	0.00	0.00	0.00	0.00	0.01	0.00
Fe^{3+}	0.13	0.13	0.09	0.16	0.12	0.16	0.05	0.06	0.13	0.13
Fe^{2+}	2.08	2.08	2.16	2.04	2.06	2.05	2.11	2.11	2.05	2.08
Mn	0.01	0.02	0.01	0.01	0.01	0.02	0.01	0.02	0.01	0.01
Mg	2.04	2.00	1.98	2.00	1.98	2.03	2.01	1.97	2.00	1.99
Ca	1.89	1.86	1.91	1.84	1.86	1.84	1.91	1.86	1.82	1.86
Na	0.46	0.49	0.49	0.48	0.48	0.51	0.50	0.48	0.52	0.47
K	0.33	0.34	0.35	0.34	0.34	0.37	0.37	0.37	0.37	0.35
Cation Total	15.73	15.73	15.78	15.71	15.71	15.76	15.79	15.73	15.75	15.72
F	0.08	0.07	0.04	0.10	0.09	0.09	0.06	0.07	0.08	0.09
Cl	0.10	0.10	0.10	0.10	0.10	0.10	0.10	0.10	0.10	0.11
X_{Mg}	0.50	0.49	0.48	0.50	0.49	0.50	0.49	0.48	0.49	0.49

Table 4-18. Representative analyses of matrix amphibole in 93010701C from Rundvågshetta.

Exposure	Rundvågshetta	Rundvågshetta	Rundvågshetta	Rundvågshetta	Rundvågshetta	Rundvågshetta	Rundvågshetta	Rundvågshetta	Rundvågshetta	Rundvågshetta
Corona	Bearing	Bearing	Bearing	Bearing	Bearing	Bearing	Bearing	Bearing	Bearing	Bearing
Sample	93010701C	93010701C	93010701C	93010701C	93010701C	93010701C	93010701C	93010701C	93010701C	93010701C
Analysis Point	Rund_93010701C_amp003	Rund_93010701C_amp007	Rund_93010701C_amp008	Rund_93010701C_amp011	Rund_93010701C_amp013	Rund_93010701C_amp017	Rund_93010701C_amp020	Rund_93010701C_amp021	Rund_93010701C_amp025	Rund_93010701C_amp029
SiO_2	41.13	41.48	41.14	41.13	41.45	40.29	41.48	40.79	41.02	40.60
TiO_2	1.36	1.34	1.45	1.39	1.29	1.31	1.24	1.36	1.55	1.65
Al_2O_3	15.03	14.90	15.50	14.93	14.79	14.86	15.25	14.68	14.64	15.17
Cr_2O_3	0.05	0.09	0.00	0.03	0.00	0.02	0.11	0.03	0.00	0.14
FeO	9.41	9.90	9.71	10.12	9.35	9.59	9.87	9.94	11.59	10.81
MnO	0.17	0.12	0.22	0.17	0.09	0.14	0.13	0.24	0.21	0.17
MgO	14.03	14.04	13.91	14.24	13.81	14.15	13.84	13.56	12.97	13.17
CaO	11.43	11.45	11.52	11.51	11.49	11.61	11.45	11.45	11.12	11.61
Na_2O	1.98	1.88	2.00	2.05	1.94	1.90	1.90	1.91	1.87	2.09
K_2O	1.28	1.27	1.34	1.27	1.18	1.20	1.34	1.43	1.36	1.29
F	0.59	0.48	0.53	0.50	0.32	0.55	0.42	0.36	0.48	0.34
Cl	0.05	0.09	0.06	0.05	0.06	0.03	0.03	0.04	0.62	0.41
Total (Inc. F & Cl)	96.51	97.05	97.37	97.39	95.78	95.65	97.04	95.77	97.42	97.44
O=-F	-0.25	-0.20	-0.22	-0.21	-0.13	-0.23	-0.18	-0.15	-0.20	-0.14
O=-Cl	-0.01	-0.02	-0.01	-0.01	-0.01	-0.01	-0.01	-0.01	-0.14	-0.09
Total	96.25	96.83	97.13	97.17	95.63	95.41	96.86	95.61	97.07	97.21
Si	6.06	6.07	6.01	6.00	6.14	5.98	6.07	6.07	6.06	5.98
Ti	0.15	0.15	0.16	0.15	0.14	0.15	0.14	0.15	0.17	0.18
Al	2.61	2.57	2.67	2.57	2.58	2.60	2.63	2.57	2.55	2.63
Cr	0.01	0.01	0.00	0.00	0.00	0.00	0.01	0.00	0.00	0.02
Fe^{3+}	0.39	0.44	0.41	0.53	0.28	0.55	0.40	0.38	0.47	0.37
Fe^{2+}	0.77	0.77	0.77	0.71	0.88	0.64	0.81	0.86	0.96	0.96
Mn	0.02	0.02	0.03	0.02	0.01	0.02	0.02	0.03	0.03	0.02
Mg	3.08	3.06	3.03	3.10	3.05	3.13	3.02	3.01	2.86	2.89
Ca	1.80	1.80	1.80	1.80	1.82	1.85	1.79	1.82	1.76	1.83
Na	0.57	0.53	0.57	0.58	0.56	0.55	0.54	0.55	0.53	0.60
K	0.24	0.24	0.25	0.24	0.22	0.23	0.25	0.27	0.26	0.24
Cation Total	15.69	15.66	15.70	15.70	15.68	15.69	15.67	15.71	15.65	15.74
F	0.28	0.23	0.25	0.24	0.15	0.26	0.20	0.17	0.23	0.16
Cl	0.01	0.02	0.01	0.01	0.02	0.01	0.01	0.01	0.16	0.10
X_{Mg}	0.80	0.80	0.80	0.81	0.78	0.83	0.79	0.78	0.75	0.75

Table 4-19. Representative analyses of matrix amphibole in I-122 from Rundvågshetta.

Exposure	Rundvågshetta	Rundvågshetta	Rundvågshetta	Rundvågshetta	Rundvågshetta	Rundvågshetta	Rundvågshetta	Rundvågshetta	Rundvågshetta	Rundvågshetta
Corona	Bearing	Bearing	Bearing	Bearing	Bearing	Bearing	Bearing	Bearing	Bearing	Bearing
Sample	I-122	I-122	I-122	I-122	I-122	I-122	I-122	I-122	I-122	I-122
Analysis Point	Ramp003	Ramp004	Ramp006	Ramp008	I122_amp025_mt Line023	Ramp011	Ramp015	Ramp016	Ramp018	Ramp020
SiO_2	40.57	41.30	41.12	41.17	41.80	41.24	41.37	41.26	41.67	41.40
TiO_2	1.54	1.53	1.52	1.51	1.20	1.40	1.53	1.42	1.49	1.61
Al_2O_3	14.19	14.01	14.27	14.60	13.98	14.24	13.76	14.25	13.96	13.96
Cr_2O_3	0.10	0.06	0.06	0.23	0.08	0.11	0.06	0.11	0.09	0.03
FeO	10.98	11.52	11.46	11.21	10.80	10.76	11.62	10.81	11.31	11.24
MnO	0.11	0.11	0.09	0.12	0.17	0.17	0.15	0.17	0.17	0.13
MgO	13.51	13.65	14.13	13.54	13.94	14.01	13.33	13.15	13.77	12.87
CaO	11.41	11.42	11.68	11.40	11.42	11.54	11.34	11.55	11.31	11.19
Na_2O	1.66	1.82	1.79	1.87	1.80	1.90	1.85	1.84	1.81	1.70
K_2O	1.76	1.75	1.67	1.63	1.55	1.73	1.63	1.75	1.65	1.49
F	0.49	0.66	0.55	0.62	0.55	0.48	0.56	0.52	0.49	0.33
Cl	0.02	0.04	0.04	0.02	0.01	0.00	0.05	0.02	0.02	0.01
Total (Inc. F & Cl)	96.33	97.87	98.37	97.92	97.30	97.57	97.24	96.85	97.72	95.96
O=-F	-0.21	-0.28	-0.23	-0.26	-0.23	-0.20	-0.24	-0.22	-0.21	-0.14
O=-Cl	-0.01	-0.01	-0.01	0.00	0.00	0.00	-0.01	0.00	-0.01	0.00
Total	96.11	97.58	98.13	97.65	97.06	97.37	96.99	96.63	97.51	95.82
Si	6.03	6.07	5.98	6.03	6.13	6.05	6.12	6.13	6.10	6.17
Ti	0.17	0.17	0.17	0.17	0.13	0.15	0.17	0.16	0.16	0.18
Al	2.49	2.43	2.45	2.52	2.42	2.46	2.40	2.49	2.41	2.45
Cr	0.01	0.01	0.01	0.03	0.01	0.01	0.01	0.01	0.01	0.00
Fe^{3+}	0.48	0.48	0.63	0.46	0.48	0.48	0.42	0.26	0.49	0.31
Fe^{2+}	0.88	0.94	0.77	0.92	0.84	0.84	1.02	1.08	0.90	1.09
Mn	0.01	0.01	0.01	0.01	0.02	0.02	0.02	0.02	0.02	0.02
Mg	2.99	2.99	3.07	2.96	3.05	3.06	2.94	2.91	3.00	2.86
Ca	1.82	1.80	1.82	1.79	1.80	1.81	1.80	1.84	1.77	1.79
Na	0.48	0.52	0.51	0.53	0.51	0.54	0.53	0.53	0.51	0.49
K	0.33	0.33	0.31	0.31	0.29	0.32	0.31	0.33	0.31	0.28
Cation Total	15.71	15.73	15.71	15.72	15.68	15.75	15.72	15.76	15.69	15.65
F	0.23	0.31	0.25	0.29	0.26	0.22	0.26	0.25	0.23	0.15
Cl	0.01	0.01	0.01	0.00	0.00	0.00	0.01	0.00	0.01	0.00
X_{Mg}	0.77	0.76	0.80	0.76	0.78	0.79	0.74	0.73	0.77	0.72

Table 4-20. Representative analyses of matrix amphibole in 93012411B from Austhovde.

Exposure	Austhovde	Austhovde	Austhovde	Austhovde	Austhovde	Austhovde	Austhovde	Austhovde	Austhovde	Austhovde
Corona	Bearing	Bearing	Bearing	Bearing	Bearing	Bearing	Bearing	Bearing	Bearing	Bearing
Sample	93012411 B	93012411 B	93012411 B	93012411 B	93012411 B	93012411 B	93012411 B	93012411 B	93012411 B	93012411 B
Analysis Point	93012411 B_amp019	93012411 B_amp024	93012411 B_amp027	93012411 B_amp029	93012411 B_amp030	93012411 B_amp032	93012411 B_amp033	93012411 B_amp035	93012411 B_amp038	93012411 B_amp040
SiO_2	42.23	41.66	42.33	42.88	43.07	41.92	42.82	42.03	41.79	42.16
TiO_2	1.81	1.95	2.03	1.98	1.83	1.92	1.80	2.04	1.91	2.06
Al_2O_3	13.00	13.57	13.40	11.70	11.73	12.43	11.55	12.37	12.45	12.56
Cr_2O_3	0.10	0.07	0.12	0.15	0.07	0.10	0.08	0.09	0.13	0.14
FeO	13.39	13.40	13.67	15.46	15.31	15.78	15.66	16.54	15.87	15.50
MnO	0.13	0.13	0.03	0.15	0.04	0.13	0.15	0.16	0.12	0.16
MgO	12.13	12.30	12.18	11.06	11.20	10.60	10.46	10.35	10.72	11.12
CaO	11.46	11.12	11.48	11.47	11.93	11.40	10.99	10.81	10.99	11.37
Na_2O	1.65	1.58	1.57	1.57	1.48	1.61	1.64	1.56	1.45	1.34
K_2O	1.52	1.41	1.44	1.22	1.27	1.58	1.39	1.48	1.69	1.62
F	0.29	0.32	0.14	0.24	0.27	0.32	0.33	0.33	0.29	0.43
Cl	0.10	0.10	0.19	0.16	0.16	0.13	0.13	0.16	0.11	0.16
Total (Inc. F & Cl)	97.81	97.61	98.59	98.04	98.34	97.91	97.01	97.91	97.51	98.61
O=-F	-0.12	-0.14	-0.06	-0.10	-0.12	-0.13	-0.14	-0.14	-0.12	-0.18
O=-Cl	-0.02	-0.02	-0.04	-0.04	-0.04	-0.03	-0.03	-0.04	-0.03	-0.04
Total	97.66	97.45	98.49	97.90	98.19	97.75	96.85	97.73	97.36	98.40
Si	6.25	6.15	6.20	6.38	6.40	6.28	6.45	6.29	6.27	6.25
Ti	0.20	0.22	0.22	0.22	0.20	0.22	0.20	0.23	0.22	0.23
Al	2.27	2.36	2.31	2.05	2.05	2.19	2.05	2.18	2.20	2.19
Cr	0.01	0.01	0.01	0.02	0.01	0.01	0.01	0.01	0.02	0.02
Fe^{3+}	0.27	0.46	0.32	0.24	0.19	0.23	0.21	0.37	0.35	0.37
Fe^{2+}	1.38	1.19	1.35	1.68	1.71	1.74	1.76	1.70	1.64	1.55
Mn	0.02	0.02	0.00	0.02	0.00	0.02	0.02	0.02	0.01	0.02
Mg	2.68	2.71	2.66	2.45	2.48	2.37	2.35	2.31	2.40	2.46
Ca	1.82	1.76	1.80	1.83	1.90	1.83	1.77	1.73	1.77	1.80
Na	0.47	0.45	0.45	0.45	0.43	0.47	0.48	0.45	0.42	0.39
K	0.29	0.26	0.27	0.23	0.24	0.30	0.27	0.28	0.32	0.31
Cation Total	15.65	15.58	15.61	15.58	15.61	15.67	15.58	15.57	15.61	15.58
F	0.14	0.15	0.06	0.11	0.13	0.15	0.16	0.16	0.14	0.20
Cl	0.02	0.03	0.05	0.04	0.04	0.03	0.03	0.04	0.03	0.04
X_{Mg}	0.66	0.69	0.66	0.59	0.59	0.58	0.57	0.58	0.59	0.61

Table 4-21. Representative analyses of matrix amphibole in 93012301C from Austhovde.

Exposure	Austhovde	Austhovde	Austhovde	Austhovde	Austhovde	Austhovde	Austhovde	Austhovde	Austhovde	Austhovde
Corona	Free	Free	Free	Free	Free	Free	Free	Free	Free	Free
Sample	93012301C	93012301C	93012301C	93012301C	93012301C	93012301C	93012301C	93012301C	93012301C	93012301C
Analysis Point	93012301C_amp012	93012301C_amp019	93012301C_amp026	93012301C_amp037	93012301C_amp043	93012301C_amp049	93012301C_amp052	93012301C_amp079	93012301C_amp086	93012301C_amp089
SiO_2	41.55	40.29	41.30	41.09	40.96	41.19	41.39	40.14	40.68	40.89
TiO_2	2.46	2.59	2.34	2.33	2.29	2.31	2.24	2.43	2.16	2.38
Al_2O_3	12.28	12.80	12.62	12.14	12.72	12.73	12.33	12.23	12.45	12.15
Cr_2O_3	0.09	0.01	0.12	0.05	0.03	0.13	0.09	0.08	0.05	0.07
FeO	18.00	18.17	18.93	18.80	18.15	18.56	17.95	18.11	18.83	19.14
MnO	0.09	0.09	0.11	0.15	0.25	0.22	0.18	0.16	0.20	0.20
MgO	8.92	8.77	8.61	8.72	8.56	8.74	8.72	8.49	7.91	8.01
CaO	11.48	11.16	11.36	10.88	10.89	11.14	11.25	11.24	11.14	10.18
Na_2O	1.60	1.67	1.84	1.82	1.66	1.79	1.69	1.58	1.47	1.76
K_2O	1.47	1.58	1.57	1.48	1.55	1.55	1.68	1.87	1.81	1.76
F	0.34	0.30	0.54	0.56	0.30	0.48	0.63	0.72	0.39	0.46
Cl	0.39	0.54	0.34	0.32	0.35	0.35	0.27	0.33	0.28	0.29
Total (Inc. F & Cl)	98.66	97.96	99.67	98.35	97.71	99.20	98.41	97.39	97.35	97.27
O=-F	-0.14	-0.13	-0.23	-0.24	-0.13	-0.20	-0.26	-0.30	-0.16	-0.19
O=-Cl	-0.09	-0.12	-0.08	-0.07	-0.08	-0.08	-0.06	-0.07	-0.06	-0.06
Total	98.43	97.71	99.37	98.04	97.50	98.92	98.08	97.02	97.13	97.02
Si	6.27	6.14	6.21	6.25	6.23	6.20	6.29	6.20	6.26	6.28
Ti	0.28	0.30	0.27	0.27	0.26	0.26	0.26	0.28	0.25	0.28
Al	2.19	2.30	2.24	2.17	2.28	2.26	2.21	2.23	2.26	2.20
Cr	0.01	0.00	0.01	0.01	0.00	0.02	0.01	0.01	0.01	0.01
Fe^{3+}	0.15	0.23	0.19	0.27	0.24	0.24	0.13	0.14	0.15	0.29
Fe^{2+}	2.13	2.08	2.19	2.12	2.07	2.10	2.15	2.20	2.27	2.17
Mn	0.01	0.01	0.01	0.02	0.03	0.03	0.02	0.02	0.03	0.03
Mg	2.01	1.99	1.93	1.98	1.94	1.96	1.97	1.96	1.81	1.83
Ca	1.86	1.82	1.83	1.77	1.78	1.80	1.83	1.86	1.84	1.67
Na	0.47	0.49	0.54	0.54	0.49	0.52	0.50	0.47	0.44	0.52
K	0.28	0.31	0.30	0.29	0.30	0.30	0.33	0.37	0.35	0.35
Cation Total	15.65	15.69	15.72	15.67	15.64	15.69	15.69	15.75	15.67	15.63
F	0.16	0.14	0.26	0.27	0.14	0.23	0.30	0.35	0.19	0.22
Cl	0.10	0.14	0.09	0.08	0.09	0.09	0.07	0.09	0.07	0.07
X_{Mg}	0.49	0.49	0.47	0.48	0.48	0.48	0.48	0.47	0.44	0.46

Table 4-22. Representative analyses of matrix amphibole in 93012301B from Austhovde.

Exposure	Austhovde	Austhovde	Austhovde	Austhovde	Austhovde	Austhovde	Austhovde	Austhovde	Austhovde	Austhovde
Corona	Bearing	Bearing	Bearing	Bearing	Bearing	Bearing	Bearing	Bearing	Bearing	Bearing
Sample	93012301 B	93012301 B	93012301 B	93012301 B	93012301 B	93012301 B	93012301 B	93012301 B	93012301 B	93012301 B
Analysis Point	93012301 B_amp034 Line 013	93012301 B_amp034 Line 015	93012301 B_amp034 Line 017	93012301 B_amp034 Line 018	93012301 B_amp034 Line 020	93012301 B_amp036 Line 004	93012301 B_amp036 Line 006	93012301 B_amp036 Line 007	93012301 B_amp036 Line 009	93012301 B_amp036 Line 010
SiO_2	38.33	39.18	39.84	39.92	39.94	38.47	38.57	38.78	38.53	38.33
TiO_2	3.00	2.86	3.06	2.84	3.08	2.64	2.65	2.80	2.74	2.53
Al_2O_3	12.00	11.65	11.01	10.71	11.07	12.14	12.11	12.06	12.24	11.83
Cr_2O_3	0.04	0.00	0.00	0.07	0.03	0.10	0.13	0.12	0.07	0.13
FeO	19.62	18.65	18.35	17.78	18.54	18.26	18.53	18.02	18.73	18.52
MnO	0.07	0.13	0.16	0.11	0.09	0.14	0.05	0.13	0.07	0.20
MgO	6.85	7.52	8.21	8.22	7.85	7.67	7.69	7.44	7.47	7.48
CaO	12.09	11.49	12.04	11.87	12.03	11.59	11.51	11.38	11.81	11.79
Na_2O	0.98	1.06	0.99	1.07	1.02	0.93	0.95	0.91	0.90	0.96
K_2O	3.07	2.81	2.84	2.75	2.85	3.00	2.97	2.83	3.10	2.77
F	0.27	0.40	0.44	0.40	0.40	0.39	0.36	0.32	0.37	0.33
Cl	2.65	2.34	2.04	2.00	2.03	2.53	2.57	2.54	2.55	2.59
Total (Inc. F & Cl)	98.96	98.08	98.97	97.74	98.93	97.85	98.07	97.32	98.58	97.46
O=-F	-0.11	-0.17	-0.18	-0.17	-0.17	-0.17	-0.15	-0.13	-0.15	-0.14
O=-Cl	-0.60	-0.53	-0.46	-0.45	-0.46	-0.57	-0.58	-0.57	-0.58	-0.58
Total	98.25	97.38	98.33	97.12	98.30	97.11	97.34	96.62	97.85	96.74
Si	6.02	6.21	6.21	6.30	6.24	6.12	6.12	6.18	6.10	6.11
Ti	0.35	0.34	0.36	0.34	0.36	0.32	0.32	0.34	0.33	0.30
Al	2.22	2.17	2.02	1.99	2.04	2.28	2.27	2.27	2.28	2.22
Cr	0.00	0.00	0.00	0.01	0.00	0.01	0.02	0.01	0.01	0.02
Fe^{3+}	0.47	-0.04	0.10	-0.07	0.03	-0.01	0.02	-0.04	-0.02	0.22
Fe^{2+}	2.11	2.51	2.30	2.42	2.39	2.44	2.44	2.44	2.50	2.24
Mn	0.01	0.02	0.02	0.01	0.01	0.02	0.01	0.02	0.01	0.03
Mg	1.60	1.78	1.91	1.94	1.83	1.82	1.82	1.77	1.76	1.78
Ca	2.03	1.95	2.01	2.01	2.01	1.98	1.96	1.94	2.00	2.01
Na	0.30	0.33	0.30	0.33	0.31	0.29	0.29	0.28	0.28	0.30
K	0.61	0.57	0.57	0.55	0.57	0.61	0.60	0.58	0.63	0.56
Cation Total	15.74	15.83	15.80	15.83	15.80	15.87	15.86	15.79	15.88	15.79
F	0.14	0.20	0.22	0.20	0.20	0.20	0.18	0.16	0.18	0.17
Cl	0.71	0.63	0.54	0.53	0.54	0.68	0.69	0.68	0.68	0.70
X_{Mg}	0.43	0.41	0.45	0.44	0.43	0.43	0.43	0.42	0.41	0.44

Table 4-23. Representative analyses of matrix amphibole in 84011107(T) from Innhovde.

Exposure	Innhovde	Innhovde	Innhovde	Innhovde	Innhovde	Innhovde	Innhovde	Innhovde	Innhovde	Innhovde
Corona	Bearing	Bearing	Bearing	Bearing	Bearing	Bearing	Bearing	Bearing	Bearing	Bearing
Sample	84011107(T)	84011107(T)	84011107(T)	84011107(T)	84011107(T)	84011107(T)	84011107(T)	84011107(T)	84011107(T)	84011107(T)
Analysis Point	Inn_amp001 Line 006	Inn_amp005	Inn_amp007	Inn_amp009	Inn_amp010	Inn_amp016	Inn_amp018	Inn_amp019	Inn_amp020	Inn_amp021
SiO_2	38.90	39.22	39.16	38.86	38.70	38.56	39.33	39.45	39.39	38.08
TiO_2	2.62	2.31	2.20	2.51	2.49	2.45	2.46	2.29	2.33	2.42
Al_2O_3	12.63	12.86	12.72	12.57	12.80	13.18	12.67	12.74	13.02	12.69
Cr_2O_3	0.00	0.00	0.00	0.01	0.00	0.06	0.01	0.00	0.01	0.07
FeO	20.07	19.68	19.29	20.12	19.85	19.35	19.84	19.74	20.51	19.38
MnO	0.03	0.00	0.20	0.12	0.12	0.03	0.11	0.05	0.09	0.09
MgO	7.27	7.62	7.32	7.43	7.82	7.30	7.73	7.73	7.27	7.61
CaO	11.20	10.95	11.27	11.21	11.36	11.70	11.26	11.49	11.34	11.11
Na_2O	1.09	1.20	1.21	1.11	1.09	1.18	1.13	0.91	1.01	1.07
K_2O	2.93	2.58	2.20	2.84	2.53	2.72	2.60	2.86	2.77	2.70
F	0.00	0.07	0.27	0.24	0.24	0.26	0.21	0.19	0.03	0.06
Cl	0.80	0.63	0.62	0.70	0.67	0.74	0.77	0.85	0.86	0.92
Total (Inc. F & Cl)	97.54	97.12	96.46	97.72	97.66	97.53	98.11	98.30	98.63	96.19
O=-F	0.00	-0.03	-0.11	-0.10	-0.10	-0.11	-0.09	-0.08	-0.01	-0.02
O=-Cl	-0.18	-0.14	-0.14	-0.16	-0.15	-0.17	-0.17	-0.19	-0.19	-0.21
Total	97.36	96.95	96.21	97.46	97.41	97.25	97.85	98.03	98.42	95.95
Si	6.08	6.11	6.15	6.07	6.01	6.04	6.09	6.10	6.08	6.02
Ti	0.31	0.27	0.26	0.30	0.29	0.29	0.29	0.27	0.27	0.29
Al	2.33	2.36	2.35	2.31	2.34	2.43	2.31	2.32	2.37	2.36
Cr	0.00	0.00	0.00	0.00	0.00	0.01	0.00	0.00	0.00	0.01
Fe^{3+}	0.14	0.23	0.16	0.21	0.37	0.05	0.24	0.21	0.22	0.28
Fe^{2+}	2.48	2.33	2.38	2.42	2.21	2.49	2.33	2.35	2.42	2.29
Mn	0.00	0.00	0.03	0.02	0.02	0.00	0.01	0.01	0.01	0.01
Mg	1.70	1.77	1.71	1.73	1.81	1.71	1.78	1.78	1.67	1.79
Ca	1.88	1.83	1.90	1.88	1.89	1.96	1.87	1.90	1.88	1.88
Na	0.33	0.36	0.37	0.34	0.33	0.36	0.34	0.27	0.30	0.33
K	0.58	0.51	0.44	0.57	0.50	0.54	0.51	0.57	0.54	0.54
Cation Total	15.83	15.77	15.74	15.83	15.76	15.88	15.78	15.78	15.78	15.80
F	0.00	0.04	0.14	0.12	0.12	0.13	0.11	0.09	0.01	0.03
Cl	0.21	0.17	0.16	0.19	0.18	0.20	0.20	0.22	0.23	0.25
X_{Mg}	0.41	0.43	0.42	0.42	0.45	0.41	0.43	0.43	0.41	0.44

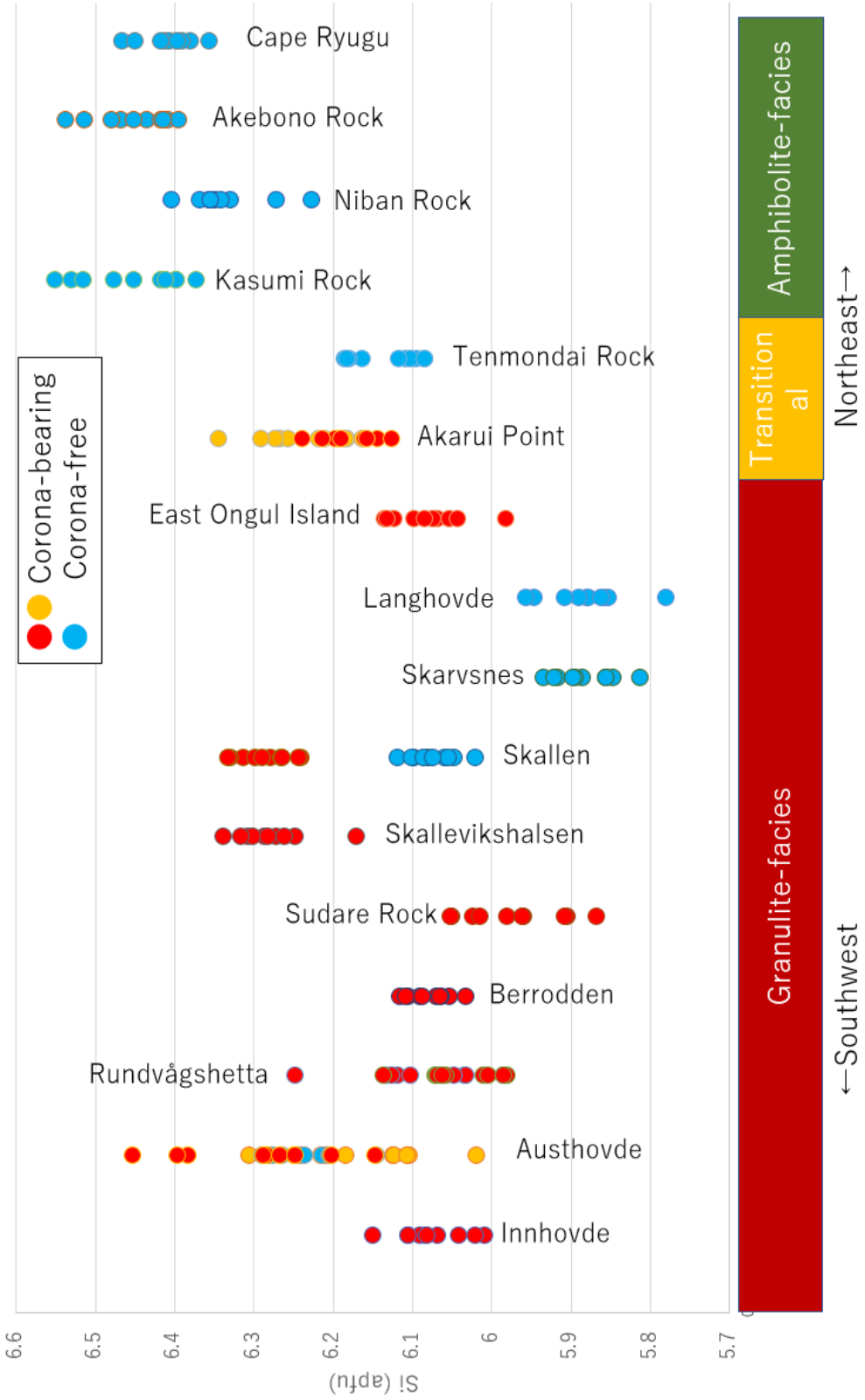

Figure 4-50. Diagram showing amounts of Si in calcic amphiboles

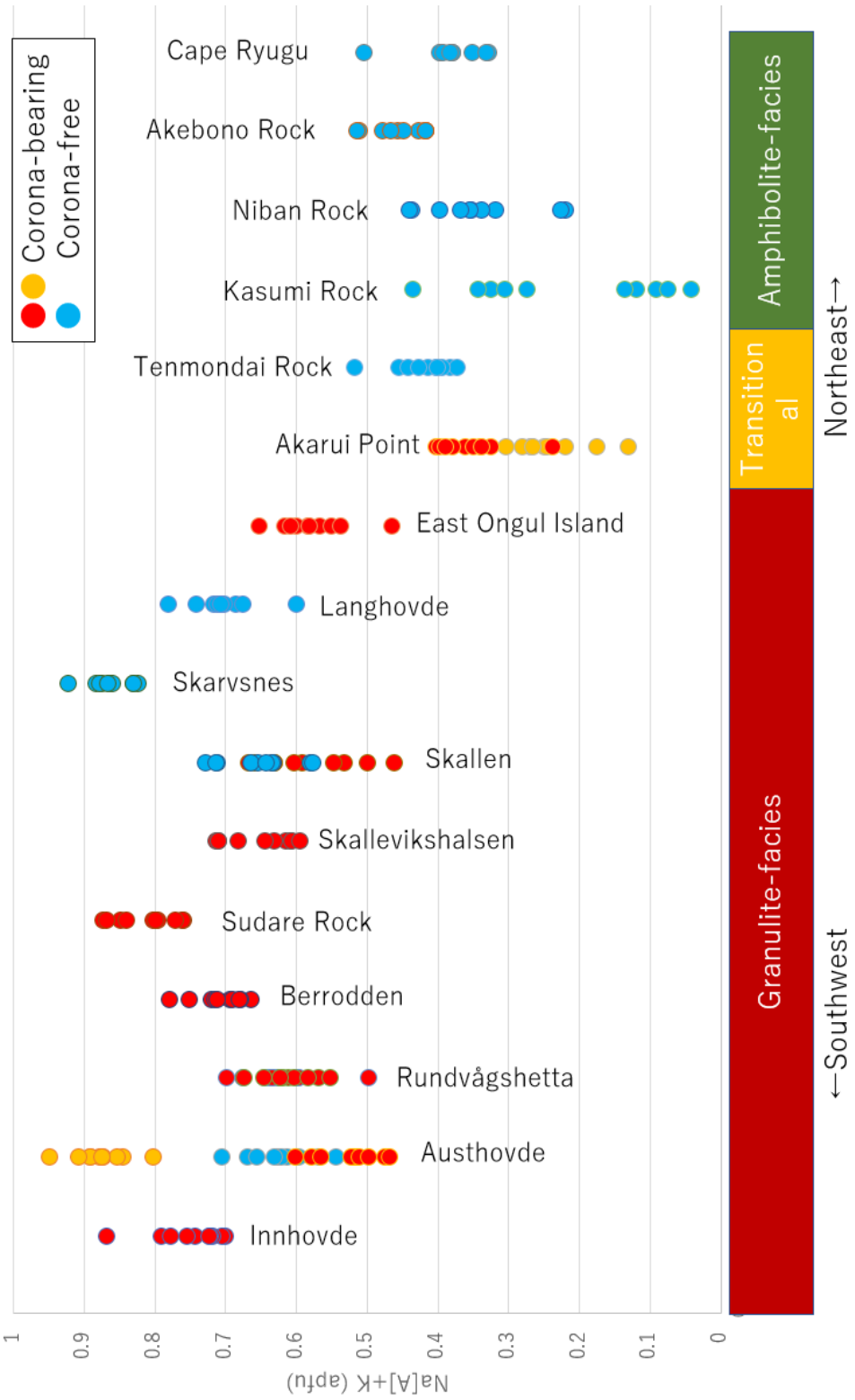

Figure 4-51. Diagram showing amounts of Na[A]+K in calcic amphiboles

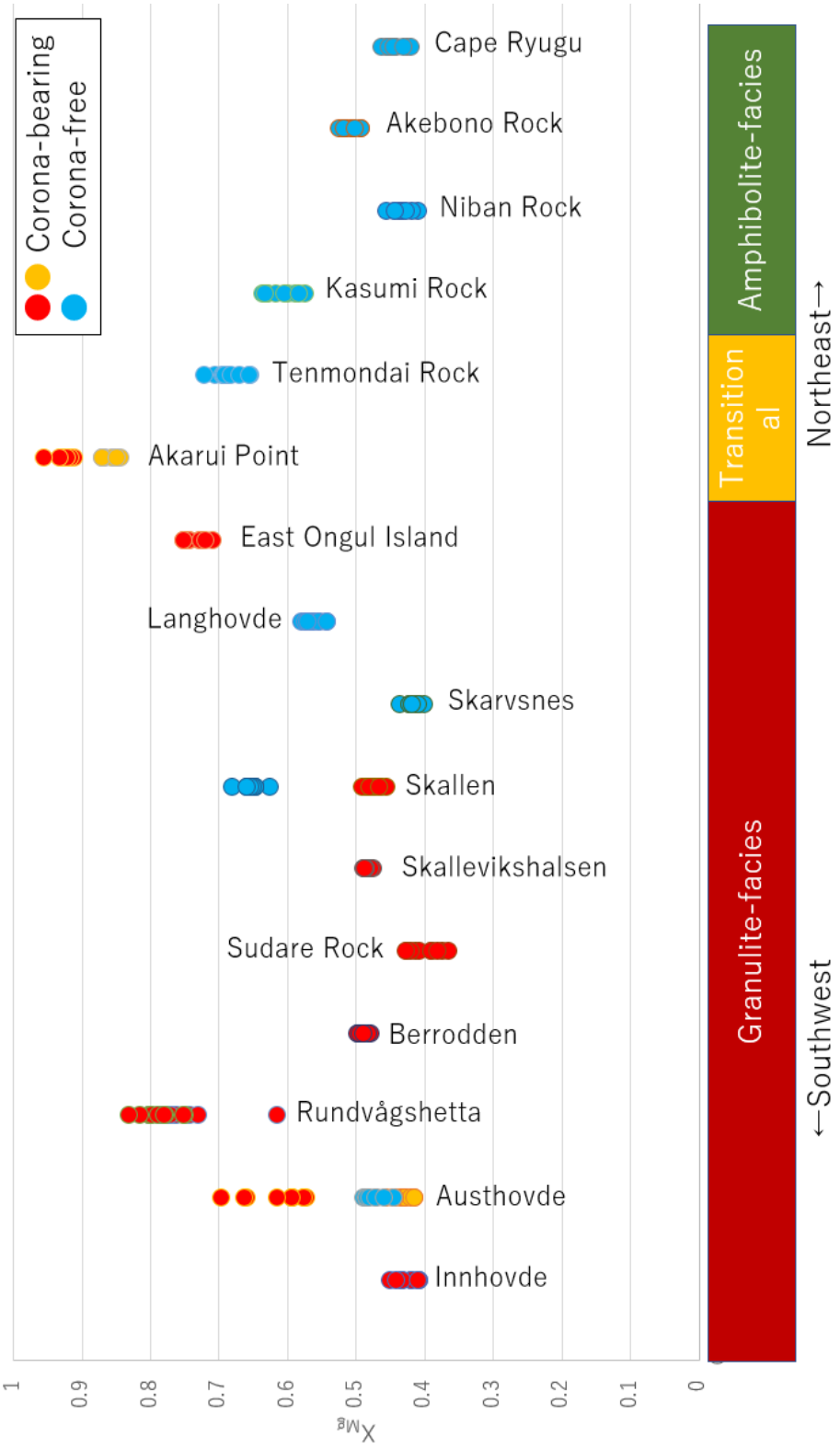

Figure 4-52. Diagram showing amounts of XMg in calcic amphiboles

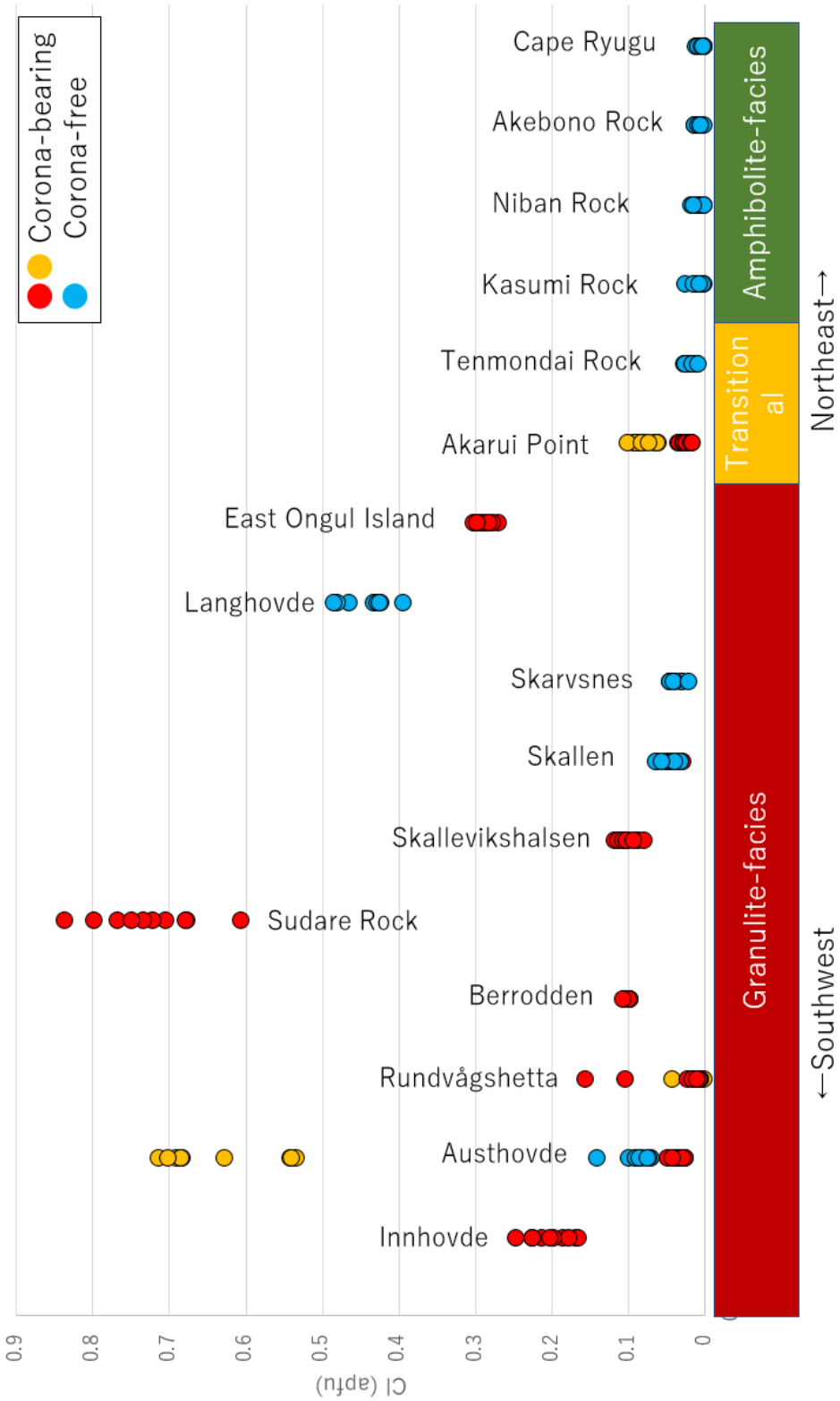

Figure 4-53. Diagram showing amounts of Cl in calcic amphiboles

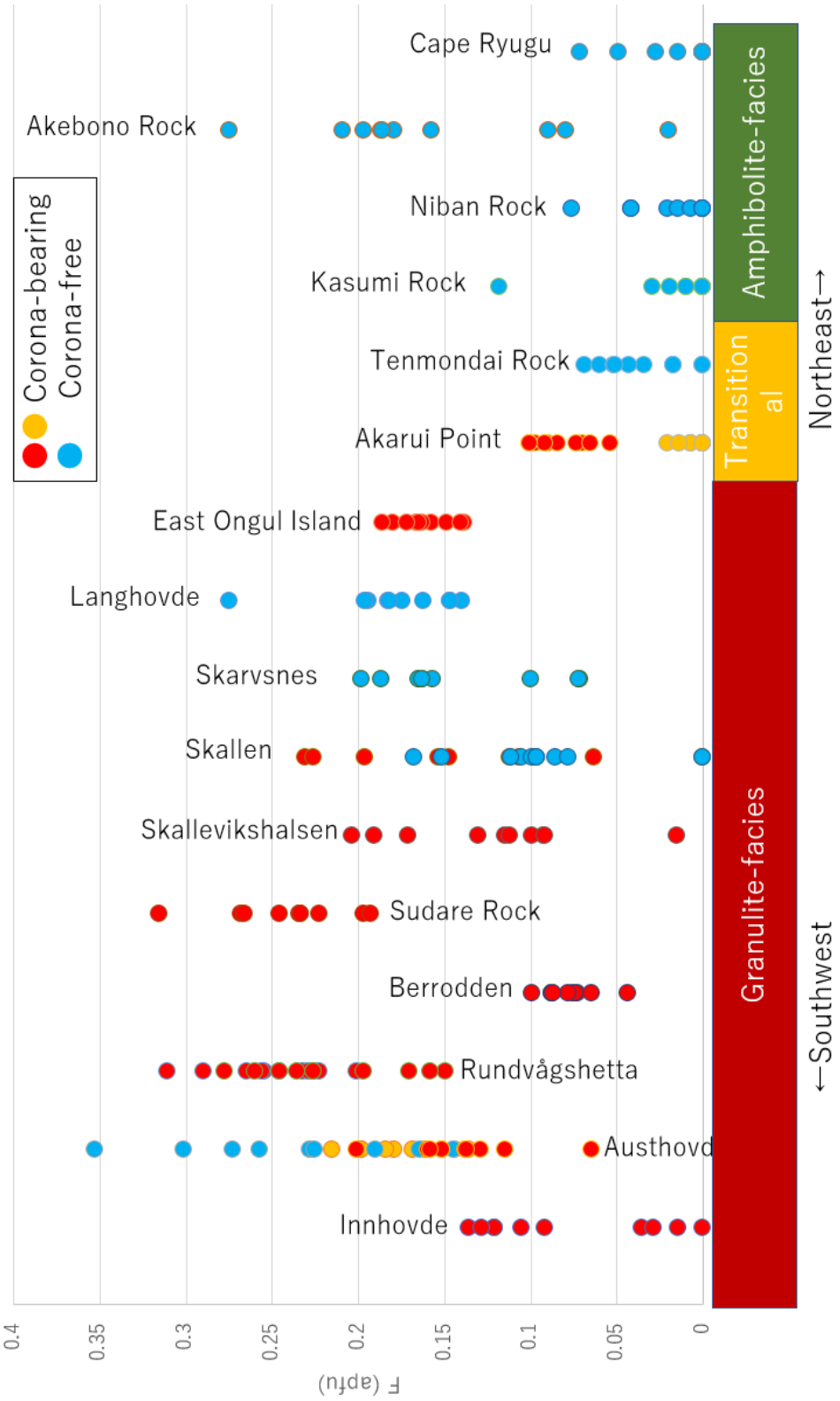

Figure 4-54. Diagram showing amounts of F in calcic amphiboles

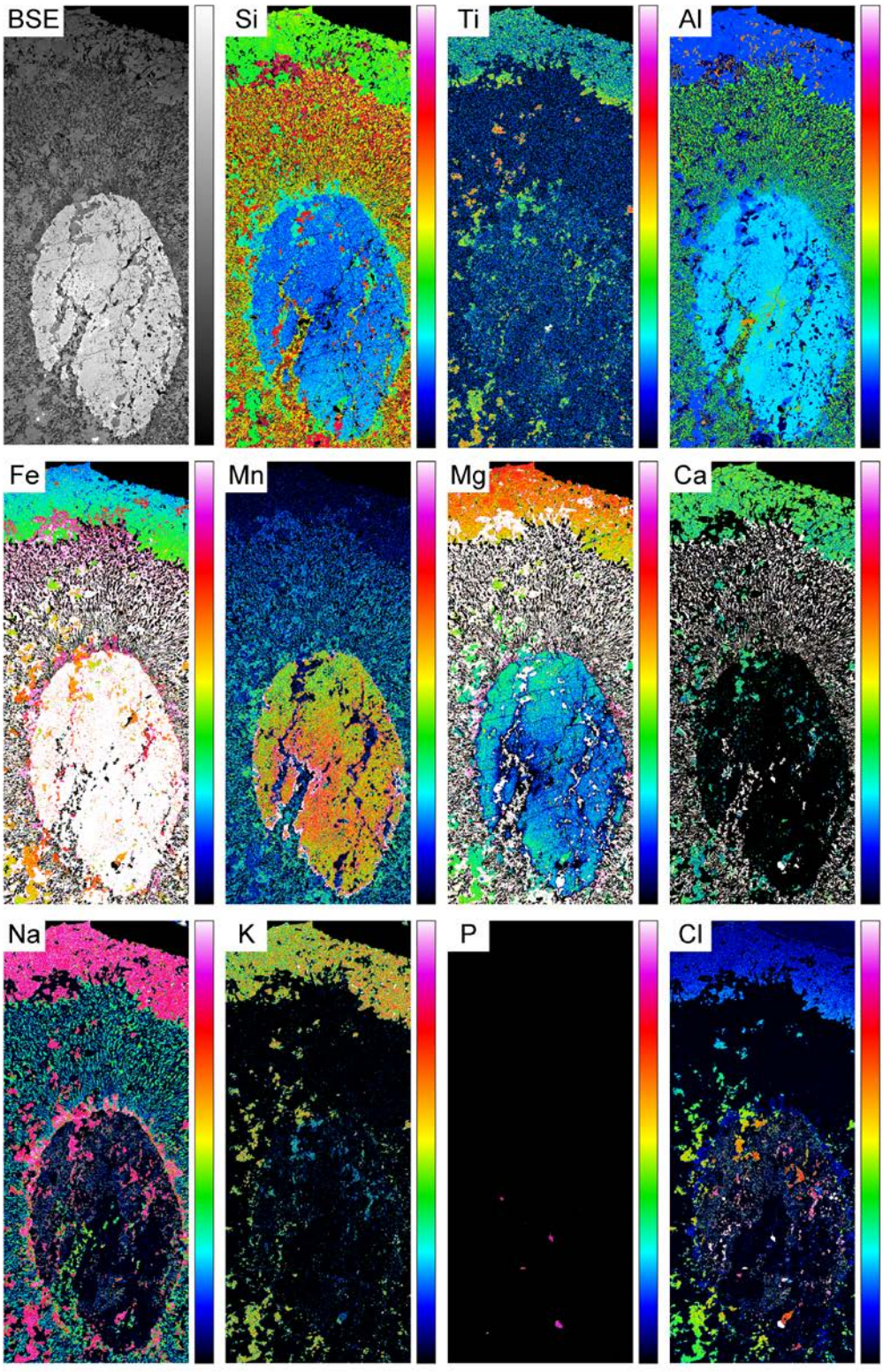

Figure 4-55. Elemental mapping of I-008 from Akarui Point. Note that Cl shows outward decrease.

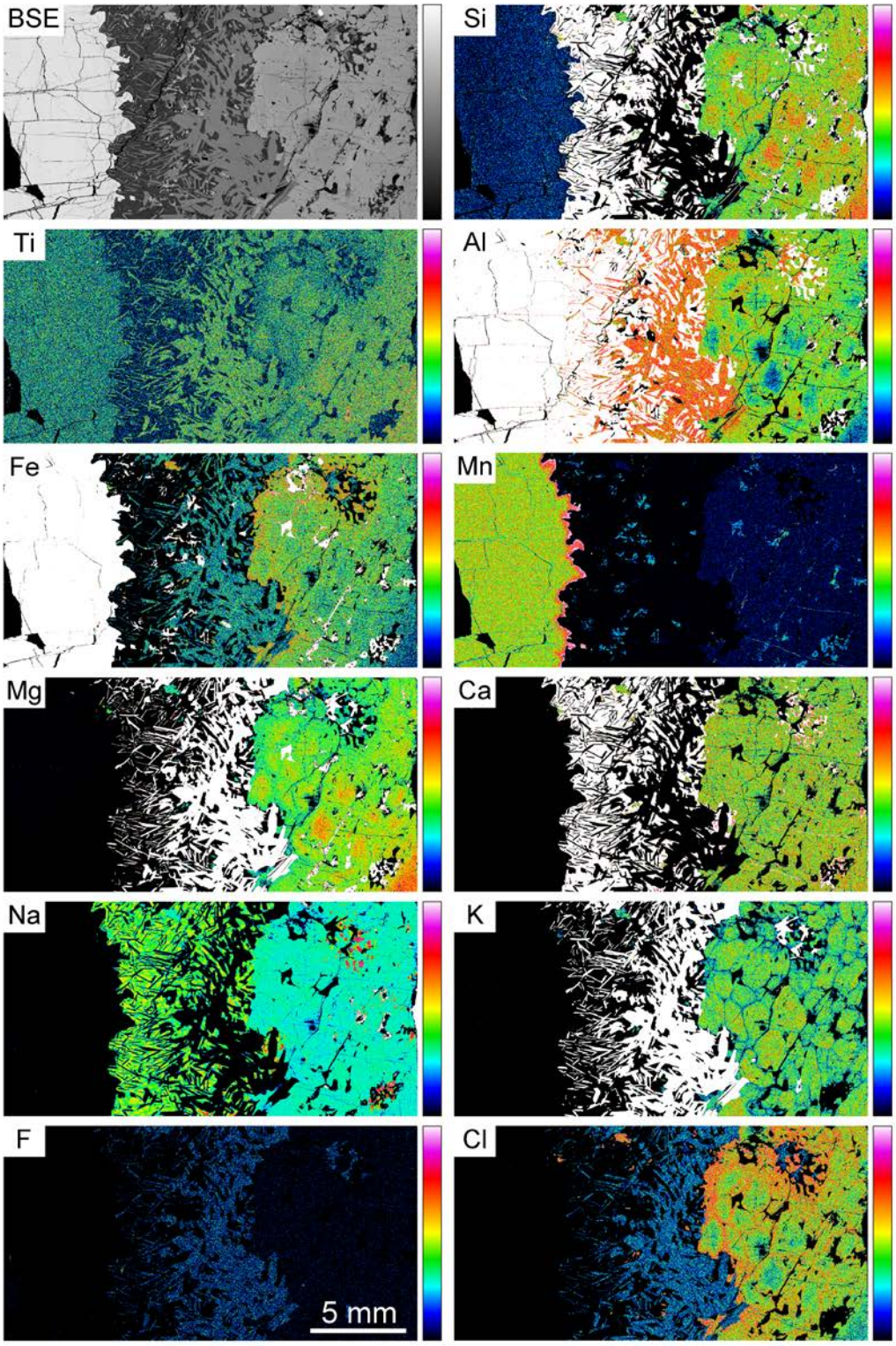

Figure 4-56. Elemental mapping of I-518 from East Ongul Island. Note that Cl in matrix hornblende shows outward decrease and core-rim structure.

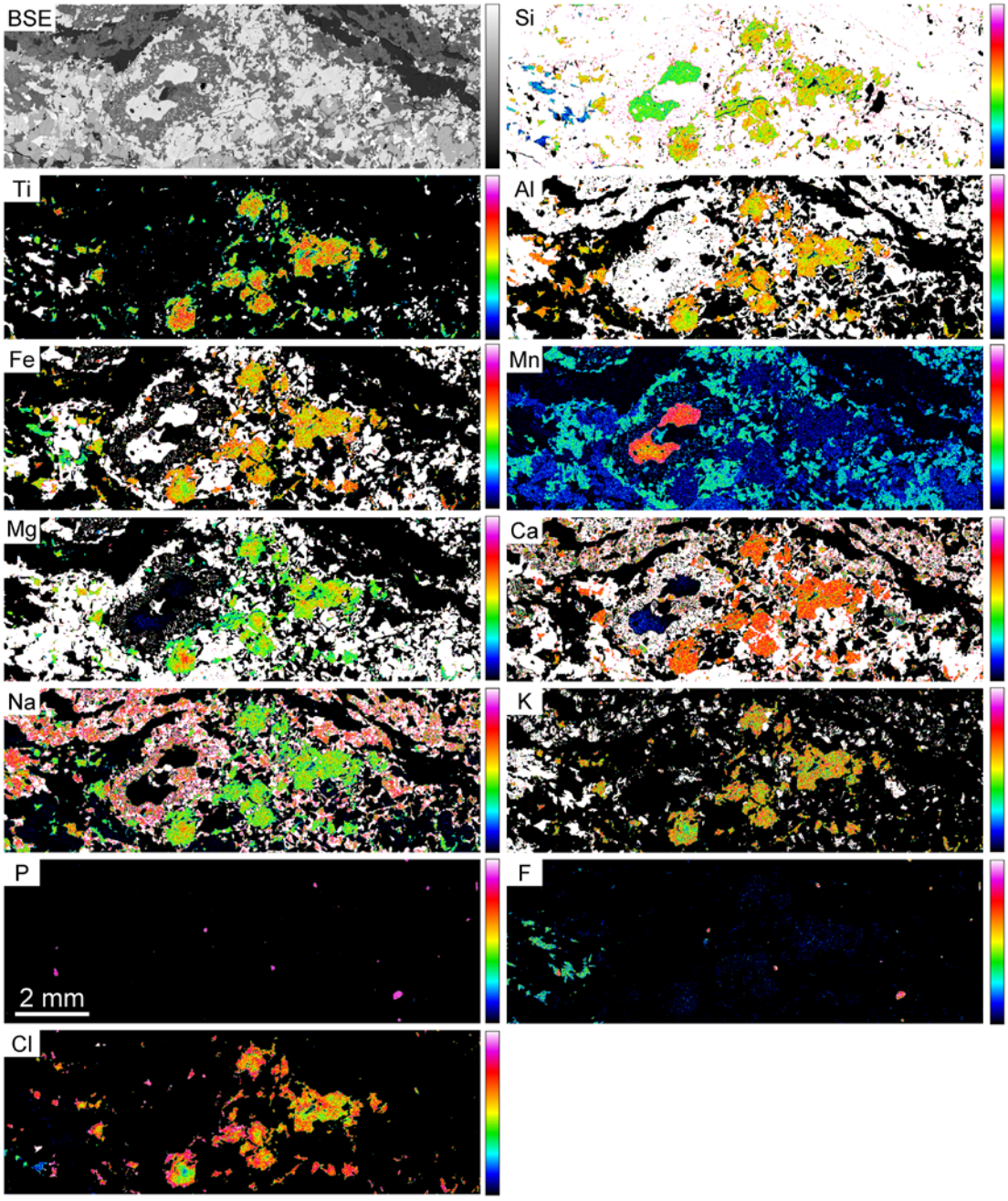

Figure 4-57. Elemental mapping of 93012301B from Austhovde. Note that Cl in the matrix hornblende shows outward decrease and core-rim structure.

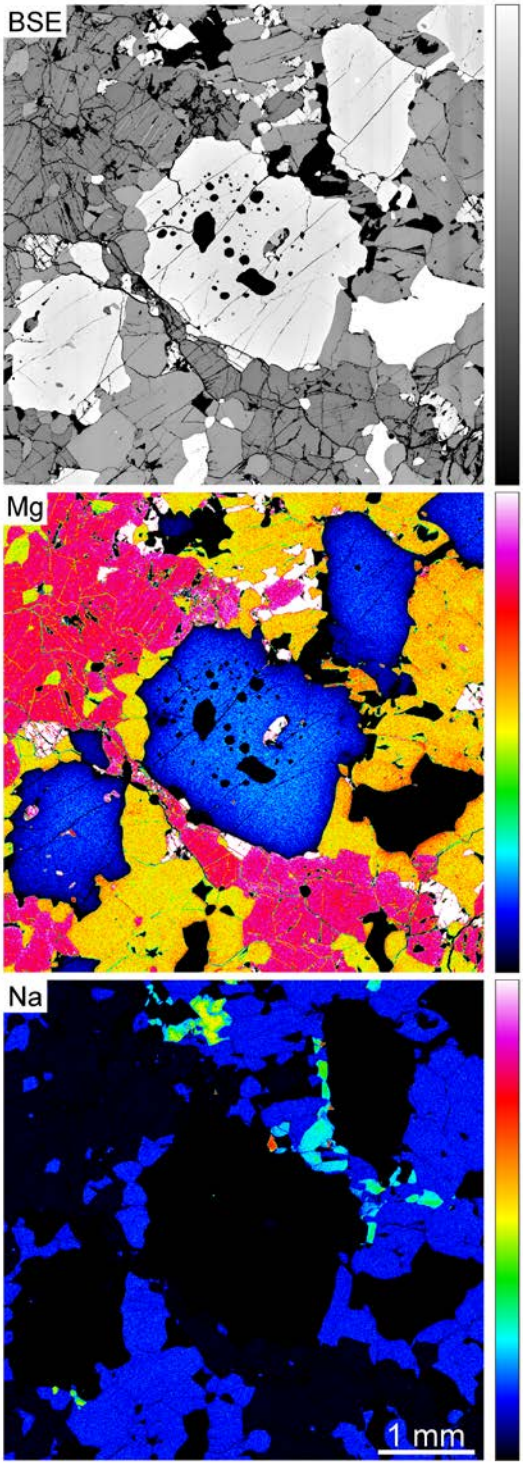

Figure 4-58. Elemental mapping of 93012301C from Austhovde. The other elements are accidentally not obtained due to machine problem. Hornblende that is in contact with ilmenite is Mg-rich, but does not show core-rim structure.

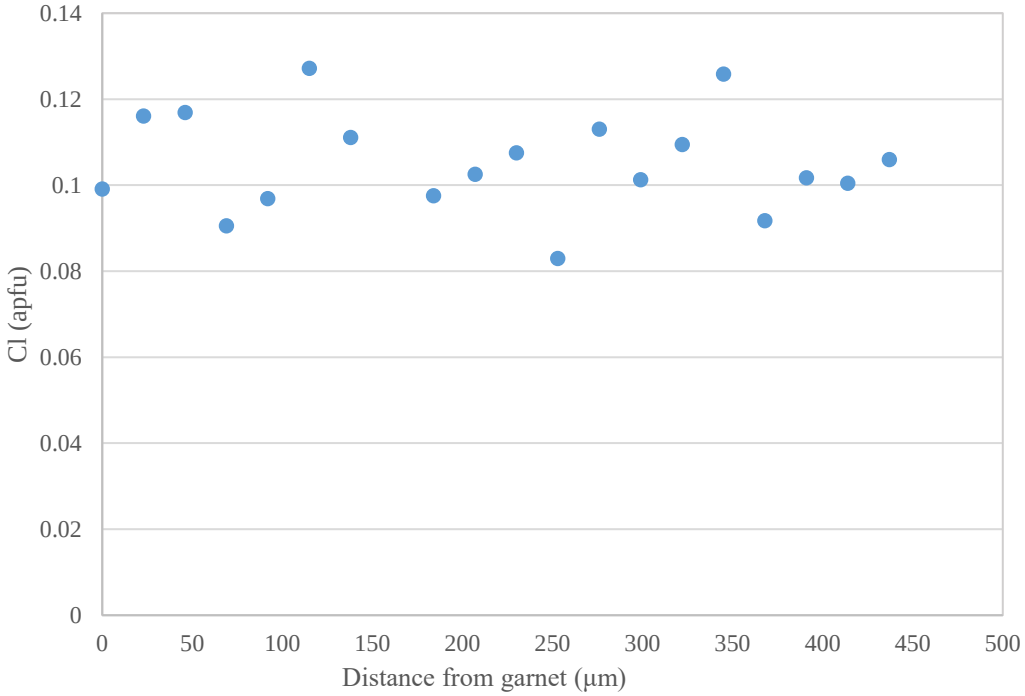

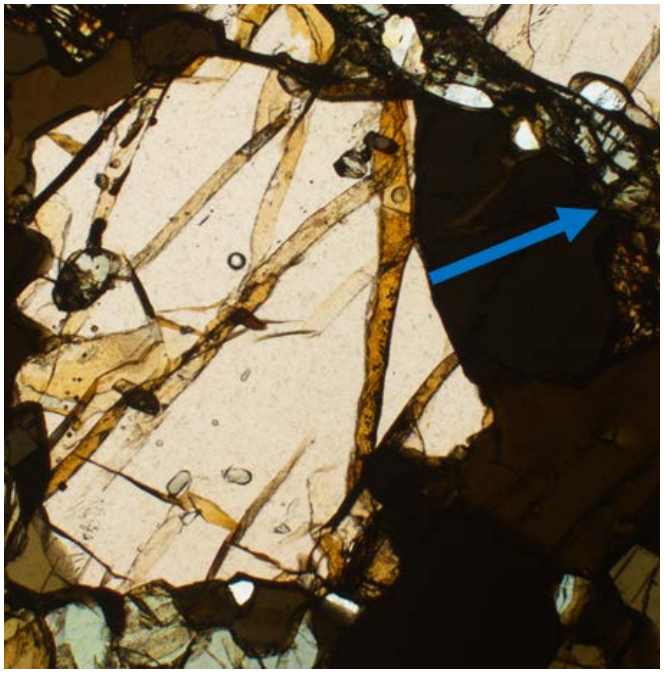

Figure 4-59. Diagram showing Cl versus distance from garnet (93012301C from Austhovde). Analysis was performed along the arrow in the bottom photomicrograph. Note that Cl is constant irrespective of distance from garnet.

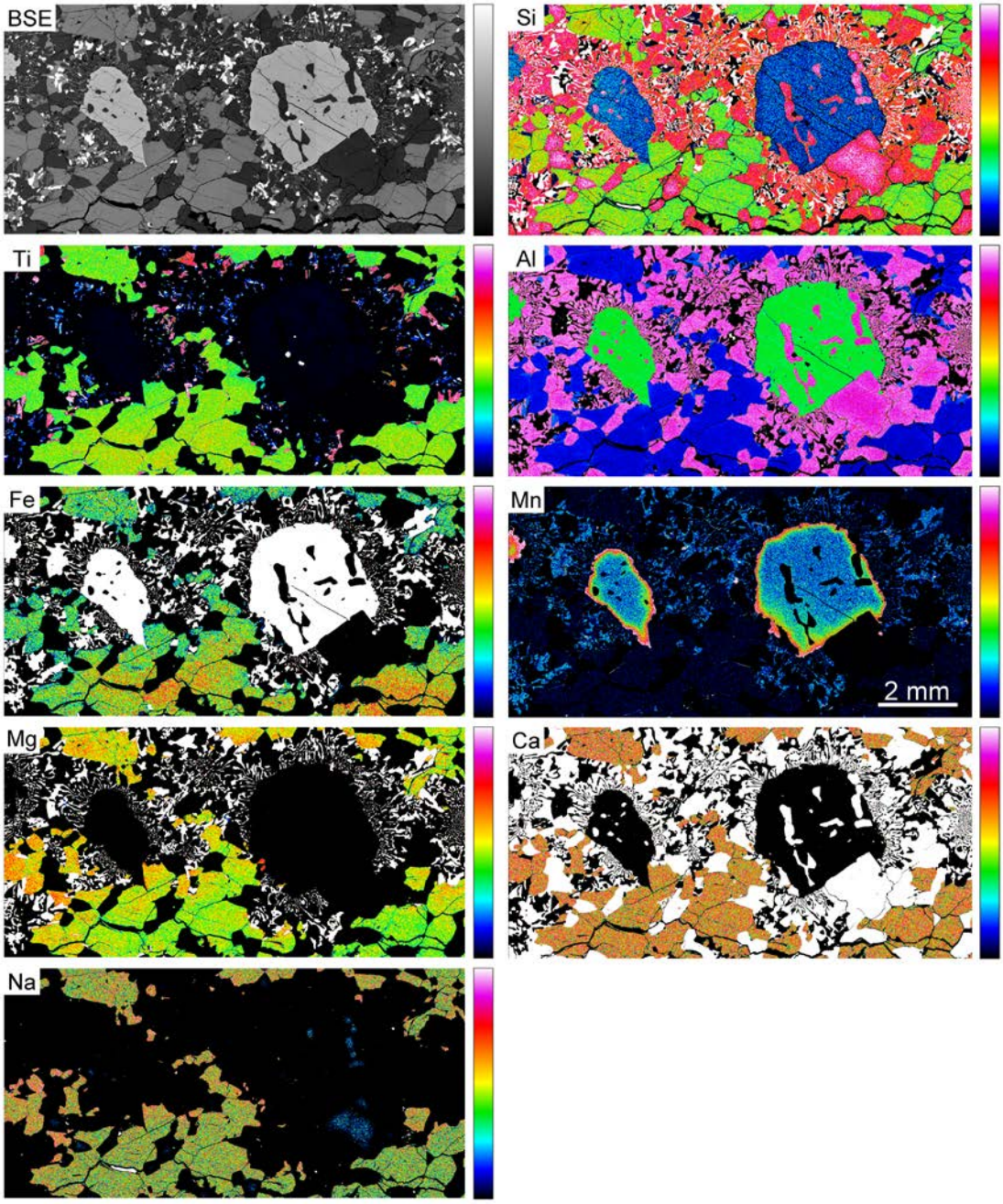

Figure 4-60. Elemental mapping of I-122 from Rundvågshetta. Note that hornblende directly in contact with garnet is Mg-rich, but does not show core-rim structure.

4.2.3. I-030 from Akarui Point

Ferric content in amphiboles was calculated following Holland and Blundy (1994) and Dale et al. (2000). All iron in aluminosilicate was treated as ferric. All iron content in garnet, plagioclase, biotite, apatite, orthopyroxene, scapolite, talc, cordierite, and chlorite was treated as ferrous. The ferric and ferrous content in magnetite was calculated on the basis of the stoichiometry and cation number (cf. Droop, 1987). Mineral compositions of scapolite were normalized to a sum of 16 cations following Kullerud & Erambert (1999). The representative analyses are shown in Table 1. $X_{alm} = Fe^{2+}/(Fe^{2+} + Mg + Ca + Mn)$, $X_{prp} = Mg/(Fe^{2+} + Mg + Ca + Mn)$, $X_{grs} = Ca/(Fe^{2+} + Mg + Ca + Mn)$, $X_{sps} = Mn/(Fe^{2+} + Mg + Ca + Mn)$, $X_{Mg} = Mg/(Mg + Fe^{2+})$, Anorthite content (An) = 100[Ca/(Ca + Na + K)].

Garnet

The composition of garnet porphyroblast is roughly $X_{alm}0.45X_{prp}0.43X_{grs}0.09X_{sps}0.03$. The core is almost homogeneous, while low-Xalm and -Xsps and high-Xgrs patches are present in the rim (Figure 4-61).

Hornblende

Ti or Ca in inclusion hornblende in garnet is lower than that in matrix hornblende. Fe^{2+} in inclusion hornblende in garnet is higher than that in matrix hornblende. In matrix hornblende, Ti increase with distance from corona, while Fe^{2+} shows opposite nature. Matrix hornblende have Cl-rich rim and Cl-poor core (Figure 4-62). In the rim composition, Cl content decreases with distance from corona. Inclusion hornblende also

have Cl-rich rim and Cl-poor core. Rim of inclusion hornblende that locate at garnet rim and is partially exposed from garnet to corona has richer composition in Cl than complete inclusion in garnet (Figure 4-61). Focusing on one grain of inclusion hornblende in garnet, the amounts of Al, Ca, Na, or K have positive correlation to that of Cl, whereas the amounts of Si or Mg have negative correlation to that of Cl (Figure 4-62). Correlations between the amount of Cl and that of Fe^{2+}, Fe^{3+}, Mn, or Ti were not detected. The negative correlation between Cl and Mg in amphibole is explained by Mg-Cl avoidance.

Gedrite

Gedrite composing corona shows compositional variation with distance from garnet. Si, Ti, and Mg increase and Al, Fe^{2+}, Mn, and Na decrease with distance from garnet. Gedrite composing FNIs varies among grains composing even in one FNI (Table 4-24). The difference in composition of gedrite among FNIs is larger than that among one FNI.

Plagioclase

Anorthite content of plagioclase composing corona decreases with distance from garnet (about An88 to 84). Matrix plagioclase shows higher anorthite content rim (An76) and lower anorthite content core (An55). Inclusion plagioclase in garnet shows almost homogeneous composition (An50 – 52) or is slightly rich in anorthite content rim. Anorthite content of plagioclase composing FNIs has a range of 12 – 42 (Table 4-24), which is much lower than that of coronal or matrix plagioclase. Plagioclase composing FNIs shows chemical zoning of An-poor core and An-rich rim, and the compositions of rims in one FNI are almost constant.

Biotite

Matrix biotite distant from corona contains higher TiO_2 (0.88 – 0.98 wt%) than that of near corona (0.47 – 0.74 wt%). In matrix biotite, decrease in Cl and increase in X_{Mg} with distance from corona were observed. Biotite composing FNI contains X_{Mg} of 0.67 – 0.77 and low TiO_2 of 0.01 – 0.20 wt% (Table 4-24). The biotite is rich in Cl (0.39 – 1.16 wt%) (Table 4-24).

Scapolite

Scapolite composing FNI is rich in Cl as 0.44 – 0.96 apfu (based on 16 cations) (Table 4-24). Only a small amount of sulfur was detected (0.00 – 0.03 apfu) in the scapolite. EqAn [=100*(Al-3)/3] varies from 21 to 50. The composition of scapolite varies even in one FNI.

Apatite

Apatite composing FNI is richer in Cl (0.23 – 0.45 apfu, O = 12.5) than that in corona (0.10 – 0.11 apfu) (Table 4-24). F in apatite composing FNI is 0.05 – 0.19 apfu, and that in corona is 0.00 – 0.04 apfu.

Orthopyroxene

X_{Mg} in matrix orthopyroxene increases with distance from corona. Orthopyroxene in matrix and as inclusion in garnet contains Al_2O_3 of 3.91 – 5.29 wt% and 4.87 – 5.27 wt%, respectively.

Other minerals

Andalusite composing FNI contains Fe_2O_3 of 1.66 – 1.86 wt% (Table 4-24). X_{Mg} of talc composing FNI is 0.90 – 0.91 (Table 4-24). X_{Mg} of cordierite composing FNI is 0.78 – 0.86 (Table 4-24).

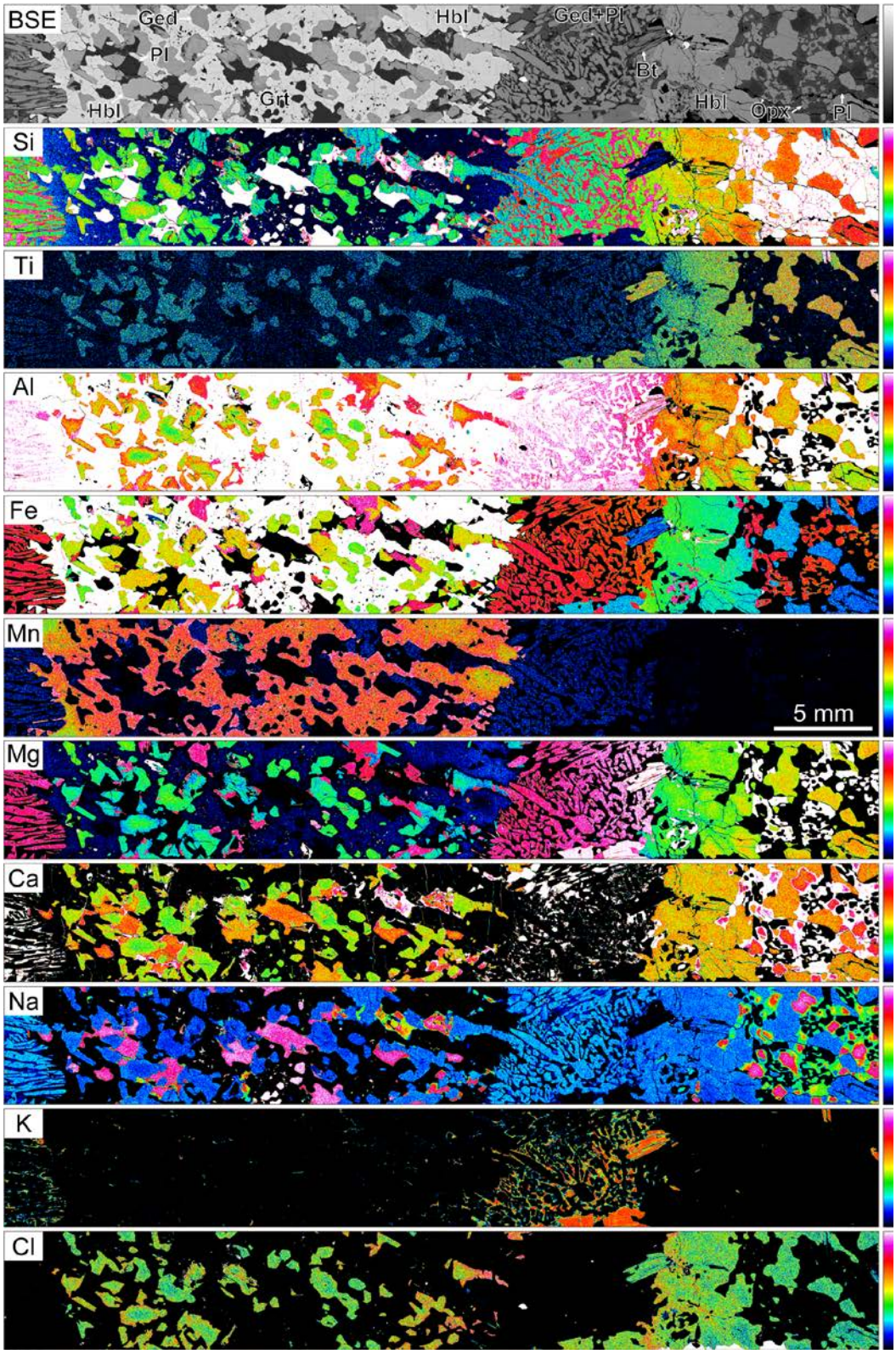

Figure 4-61. Elemental mapping of I-030

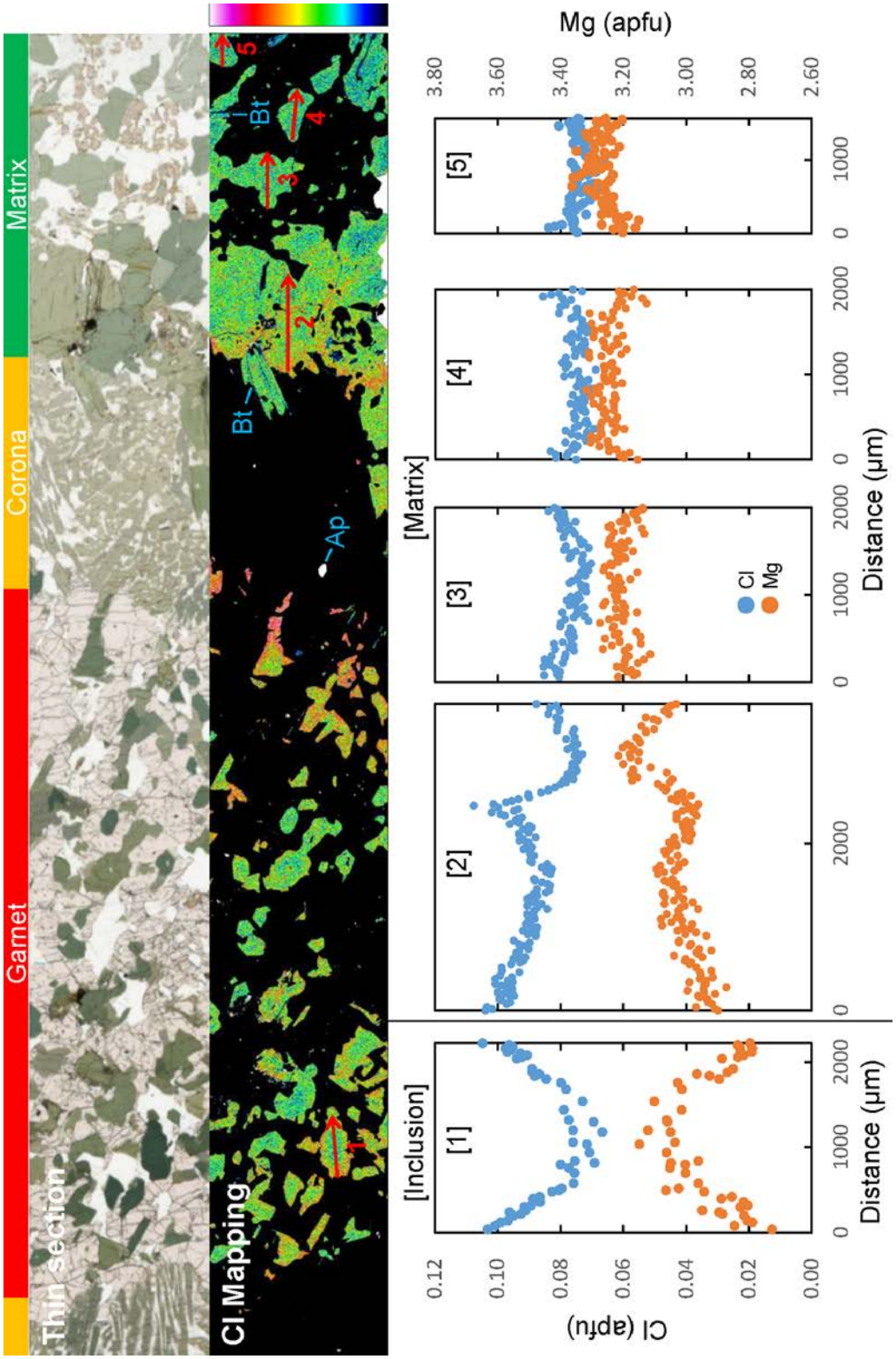

Figure 4-62. Zoning profiles of inclusion and matrix amphiboles. Note that Cl shows opposite zoning pattern to Mg.

Table 4-24. Representative analyses of constituent minerals of felsite-nanogranite inclusion in I-030.

Mineral	Bt	Bt	Bt	Bt	Bt	Bt	Chl	Crd	Ged	Ged	Hbl
FNI no.	11	7	5	5	10	13	11	11	11	5	5
Analysis Point	I030_min065_10nA	I030_min108_10nA	I030_min139	I030_min142	I030_min156	I030_min158	I030_min068_10nA	I030_min069_10nA	I030_min063_10nA	I030_min140	I030_min141
SiO_2	36.48	37.31	36.61	37.17	37.62	36.64	30.22	49.38	45.18	41.62	39.12
TiO_2	0.09	0.10	0.12	0.08	0.04	0.01	0.00	0.00	0.00	0.00	0.00
Al_2O_3	17.62	18.60	19.27	19.77	18.10	18.30	17.86	33.85	14.05	19.74	19.25
Cr_2O_3	0.00	0.02	0.02	0.00	0.01	0.00	0.00	0.00	0.00	0.01	0.00
Fe_2O_3	-	-	-	-	-	-	-	-	-	-	-
FeO	13.84	10.69	10.42	9.76	11.04	11.99	23.12	5.37	15.74	16.09	14.88
MnO	0.09	0.08	0.09	0.08	0.06	0.04	0.18	0.38	0.44	0.43	0.37
MgO	15.91	18.03	18.11	18.03	17.61	17.28	14.44	10.75	18.26	16.16	10.21
CaO	0.04	0.03	0.03	0.02	0.07	0.06	0.19	0.05	0.35	0.43	9.51
ZnO	0.00	0.07	0.00	0.17	0.06	0.11	0.07	0.04	0.00	0.00	0.13
Na_2O	0.06	0.21	0.51	0.40	0.17	0.12	0.02	0.05	1.17	1.79	2.01
K_2O	8.76	8.94	8.18	7.75	8.77	8.78	0.17	0.01	0.02	0.00	0.30
P_2O_5	-	-	-	-	-	-	-	-	-	-	-
SO_3	-	-	-	-	-	-	-	-	-	-	-
F	0.01	0.00	0.00	0.00	0.03	0.00	0.00	0.00	0.00	0.01	0.00
Cl	1.06	0.72	0.48	0.47	0.78	0.91	0.02	0.02	0.08	0.10	0.81
O=-F	0.00	0.00	0.00	0.00	-0.01	0.00	0.00	0.00	0.00	0.00	0.00
O=-Cl	-0.24	-0.16	-0.11	-0.11	-0.18	-0.21	0.00	-0.01	-0.02	-0.02	-0.18
Total	93.72	94.61	93.73	93.62	94.15	94.04	86.27	99.90	95.27	96.35	96.41
Number of O	22	22	22	22	22	22	28	18	23	23	23
Si	5.52	5.49	5.40	5.45	5.57	5.47	6.34	4.95	6.60	6.05	5.89
Ti	0.01	0.01	0.01	0.01	0.00	0.00	0.00	0.00	0.00	0.00	0.00
Al	3.14	3.22	3.35	3.42	3.16	3.22	4.42	4.00	2.42	3.38	3.42
Cr	0.00	0.00	0.00	0.00	0.00	0.00	0.00	0.00	0.00	0.00	0.00
Fe^{3+}	-	-	-	-	-	-	-	-	-	-	-
Fe^{2+}	1.75	1.32	1.29	1.20	1.37	1.50	4.06	0.45	1.92	1.96	1.87
Mn	0.01	0.01	0.01	0.01	0.01	0.00	0.03	0.03	0.05	0.05	0.05
Mg	3.59	3.95	3.99	3.94	3.88	3.85	4.52	1.61	3.98	3.50	2.29
Ca	0.01	0.00	0.01	0.00	0.01	0.01	0.04	0.01	0.05	0.07	1.54
Zn	0.00	0.01	0.00	0.02	0.01	0.01	0.01	0.00	0.00	0.00	0.01
Na	0.02	0.06	0.15	0.11	0.05	0.04	0.01	0.01	0.33	0.50	0.59
K	1.69	1.68	1.54	1.45	1.65	1.67	0.04	0.00	0.00	0.00	0.06
P	0.00	0.00	0.00	0.00	0.00	0.00	0.00	0.00	0.00	0.00	0.00
Total Cation	15.75	15.75	15.75	15.61	15.70	15.77	19.47	11.06	15.36	15.51	15.72
S	-	-	-	-	-	-	-	-	-	-	-
F	0.00	0.00	0.00	0.00	0.02	0.00	0.00	0.00	0.00	0.01	0.00
Cl	0.27	0.18	0.12	0.12	0.20	0.23	0.01	0.00	0.02	0.03	0.21

Continued.

Mineral	Tlc	Tlc	Mgt	Mgt	Pl	Pl	Pl	Pl	Pl
FNI no.	7	10	10	13	11	7	7	10	13
Analysis Point	I030_min107_10nA	I030_min153	I030_min155	I030_min159	I030_min071_10nA	I030_min105_10nA	I030_min106_10nA	I030_min154	I030_min162
SiO_2	58.01	59.23	0.12	0.05	58.50	57.50	64.74	61.77	58.60
TiO_2	0.00	0.04	0.05	0.00	0.00	0.01	0.00	0.00	0.00
Al_2O_3	3.51	3.14	0.10	0.05	25.93	27.16	21.78	23.98	26.35
Cr_2O_3	0.01	0.01	0.00	0.00	0.00	0.01	0.01	0.00	0.00
Fe_2O_3	-	-	-	-	-	-	-	-	-
FeO	5.30	4.58	91.21	91.75	0.47	0.42	0.35	0.24	0.57
MnO	0.07	0.05	0.04	0.00	0.00	0.01	0.09	0.00	0.00
MgO	26.34	27.16	0.02	0.00	0.00	0.02	0.01	0.00	0.02
CaO	0.02	0.06	0.03	0.05	7.37	8.63	2.64	5.31	7.71
ZnO	0.09	0.06	0.00	0.04	0.07	0.00	0.00	0.00	0.10
Na_2O	0.24	0.11	0.01	0.00	7.49	6.45	10.24	8.30	7.17
K_2O	0.02	0.00	0.00	0.00	0.04	0.04	0.01	0.03	0.04
P_2O_5	-	-	-	-	-	-	-	-	-
SO_3	-	-	-	-	-	-	-	-	-
F	0.00	0.00	-	-	-	-	-	-	-
Cl	0.01	0.02	-	-	-	-	-	-	-
O=-F	0.00	0.00	-	-	-	-	-	-	-
O=-Cl	0.00	0.00	-	-	-	-	-	-	-
Total	93.62	94.45	91.57	91.94	99.87	100.25	99.85	99.63	100.55
Number of O	11	11	4	4	8	8	8	8	8
Si	3.84	3.86	0.00	0.00	2.62	2.57	2.86	2.75	2.61
Ti	0.00	0.00	0.00	0.00	0.00	0.00	0.00	0.00	0.00
Al	0.27	0.24	0.00	0.00	1.37	1.43	1.13	1.26	1.38
Cr	0.00	0.00	0.00	0.00	0.00	0.00	0.00	0.00	0.00
Fe^{3+}	-	-	1.98	1.99	-	-	-	-	-
Fe^{2+}	0.29	0.25	1.00	1.00	0.02	0.02	0.01	0.01	0.02
Mn	0.00	0.00	0.00	0.00	0.00	0.00	0.00	0.00	0.00
Mg	2.60	2.64	0.00	0.00	0.00	0.00	0.00	0.00	0.00
Ca	0.00	0.00	0.00	0.00	0.35	0.41	0.12	0.25	0.37
Zn	0.00	0.00	0.00	0.00	0.00	0.00	0.00	0.00	0.00
Na	0.03	0.01	0.00	0.00	0.65	0.56	0.88	0.72	0.62
K	0.00	0.00	0.00	0.00	0.00	0.00	0.00	0.00	0.00
P	0.00	0.00	-	-	-	-	-	-	-
Total Cation	7.04	7.02	3.00	3.00	5.02	4.99	5.01	4.98	5.01
S	-	-	-	-	-	-	-	-	-
F	0.00	0.00	-	-	-	-	-	-	-
Cl	0.00	0.00	-	-	-	-	-	-	-

Continued.

Mineral	Als	Als	Als	Ap	Ap	Ap	Scp	Scp	Scp	Scp
FNI no.	7	13	16	3	15	6	6	6	6	13
Analysis Point	I030_min109_10nA	I030_min118	I030_min148	I030_min042-3	I030_min088	I030_min096	I030_min095_3rd	I030_min092_3rd	I030_min093_3rd	I030_min119_3rd
SiO_2	36.96	36.62	36.47	0.41	0.36	0.08	49.74	50.51	60.68	55.09
TiO_2	0.00	0.00	0.00	0.00	0.06	0.02	0.00	0.00	0.00	0.00
Al_2O_3	61.88	62.81	62.13	0.18	0.04	0.04	25.90	24.60	21.82	22.92
Cr_2O_3	0.00	0.00	0.00	0.04	0.00	0.05	0.00	0.00	0.00	0.00
Fe_2O_3	1.68	1.66	1.86	-	-	-	-	-	-	-
FeO	-	-	-	0.63	0.49	0.65	0.82	0.38	0.46	0.32
MnO	0.03	0.04	0.03	0.01	0.05	0.12	0.07	0.00	0.00	0.00
MgO	0.11	0.10	0.10	0.02	0.00	0.01	0.12	0.04	0.00	0.00
CaO	0.00	0.02	0.00	52.73	53.67	53.47	12.81	12.40	4.17	7.41
ZnO	0.00	0.05	0.00	0.00	0.00	0.00	0.00	0.00	0.00	0.00
Na_2O	0.00	0.02	0.03	0.11	0.00	0.03	7.02	6.34	11.06	9.90
K_2O	0.00	0.00	0.00	0.00	0.03	0.01	0.11	0.06	0.17	0.19
P_2O_5	-	-	-	40.30	40.99	42.00	-	-	-	-
SO_3	-	-	-	-	-	-	0.24	0.25	0.00	0.10
F	-	-	-	0.70	0.27	0.17	0.00	0.00	0.00	0.00
Cl	-	-	-	3.03	1.60	1.61	1.89	1.73	3.98	3.19
O=-F	-	-	-	-0.29	-0.12	-0.07	0.00	0.00	0.00	0.00
O=-Cl	-	-	-	-0.68	-0.36	-0.36	-0.43	-0.39	-0.90	-0.72
Total	100.66	101.31	100.61	97.17	97.10	97.82	98.28	95.91	101.43	98.40
Number of O	5	5	5	12.5	12.5	12.5	-	-	-	-
Si	1.00	0.98	0.99	0.04	0.03	0.01	7.32	7.66	8.60	8.03
Ti	0.00	0.00	0.00	0.00	0.00	0.00	0.00	0.00	0.00	0.00
Al	1.97	1.99	1.98	0.02	0.00	0.00	4.50	4.39	3.64	3.94
Cr	0.00	0.00	0.00	0.00	0.00	0.00	0.00	0.00	0.00	0.00
Fe^{3+}	0.03	0.03	0.04	-	-	-	-	-	-	-
Fe^{2+}	-	-	-	0.05	0.04	0.05	0.10	0.05	0.05	0.04
Mn	0.00	0.00	0.00	0.00	0.00	0.01	0.01	0.00	0.00	0.00
Mg	0.00	0.00	0.00	0.00	0.00	0.00	0.03	0.01	0.00	0.00
Ca	0.00	0.00	0.00	4.92	4.94	4.87	2.02	2.01	0.63	1.16
Zn	0.00	0.00	0.00	0.00	0.00	0.00	0.00	0.00	0.00	0.00
Na	0.00	0.00	0.00	0.02	0.00	0.01	2.00	1.86	3.04	2.80
K	0.00	0.00	0.00	0.00	0.00	0.00	0.02	0.01	0.03	0.03
P	-	-	-	2.97	2.98	3.02	-	-	-	-
Total Cation	3.00	3.01	3.01	8.01	8.00	7.96	16.00	16.00	16.00	16.00
S	-	-	-	-	-	-	0.03	0.03	0.00	0.01
F	-	-	-	0.19	0.07	0.05	0.00	0.00	0.00	0.00
Cl	-	-	-	0.45	0.23	0.23	0.47	0.44	0.96	0.79

4.2.4. Pelitic Gneiss from Niban Rock

All iron in minerals except for aluminosilicates was treated as ferrous. Iron in aluminosilicates was treated as ferric.

Garnet

Garnet has almost homogeneous composition except for rim (Figures 4-63, 4-64). In the rim, XMg shows monotonic decrease toward periphery, which is regarded as retrograde zoning. Garnet rim in contact with matrix biotite show more depletion in Mg/(Mg+Fe) than that in contact with quartz, sillimanite, or plagioclase.

Biotite

No zoning in biotite was observed. Inclusion biotite in garnet shows higher Mg/(Mg+Fe) of 0.56 – 0.63 than matrix biotite not in contact with garnet (0.44 – 0.49) (Figure 4-66). Most matrix biotite in contact with garnet rim shows same composition as that not in contact with garnet. Some matrix biotite in contact with garnet rim shows slightly higher XMg. According to elemental mapping of Mg and Fe, small grains of the biotite show higher Mg and lower Fe (Figure 4-63). Therefore, the variation in the biotite is due to difference in effective volume for Mg-Fe exchange between garnet and biotite. Local Ti depletion in biotite in contact with ilmenite was detected (Figure 4-66). Inclusion biotite in matrix plagioclase are plotted in the compositional range of matrix biotite (Figure 4-66).

Plagioclase

Anorthite content of plagioclase is almost homogeneous in one grain except at the rim, where it slightly increases (Figure 4-63).

Rutile

Zr concentration in rutile included in garnet core shows narrow range of 364 – 448 ppm (n = 7).

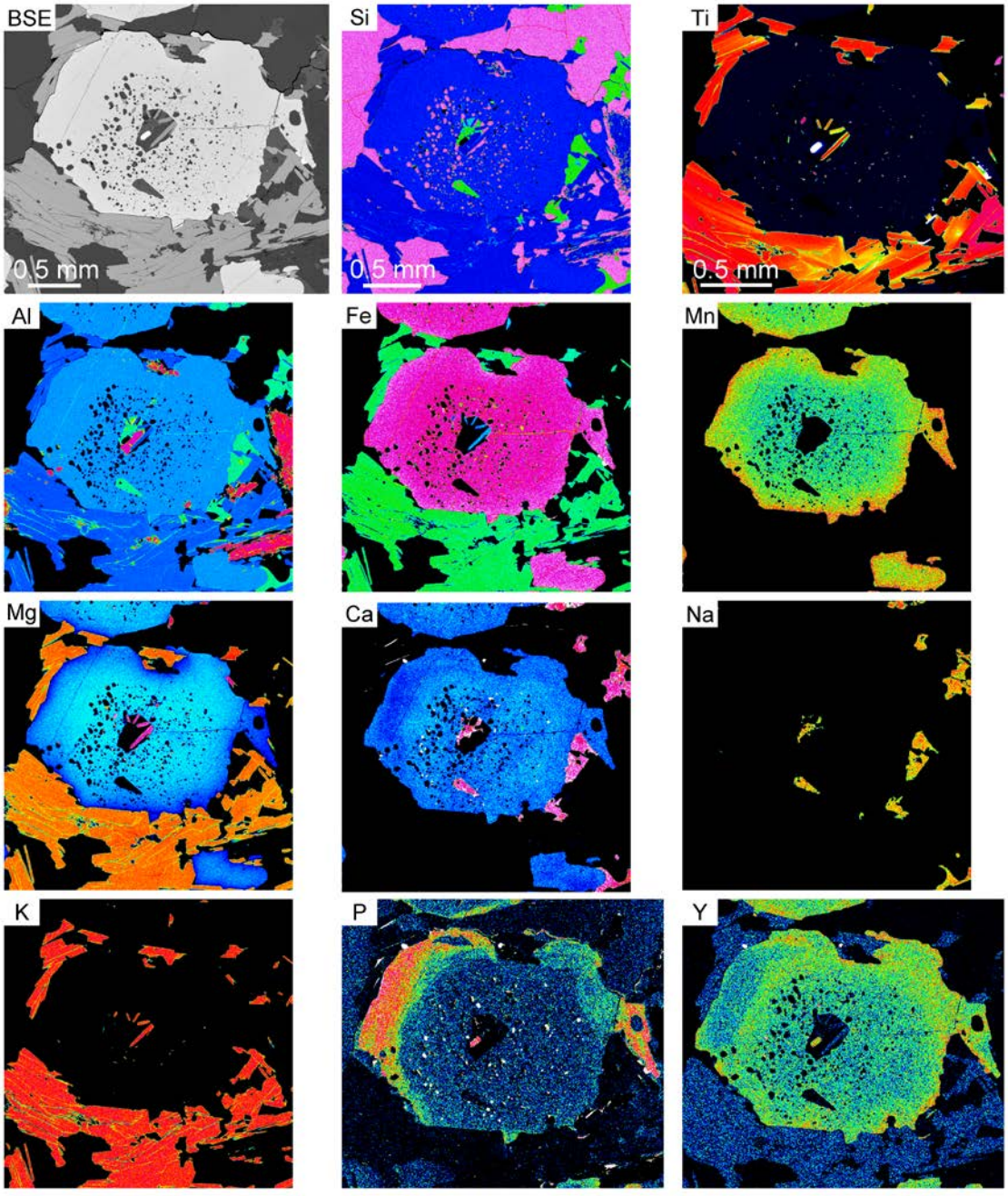

Figure 4-63. Elemental mapping of pelitic gneiss from Niban rock (no. TM11020702A). Scales of P and Y are same as that of Ti. Scales of other elements are same as that of Si. Analytical condition of Ti in this mapping is exceptionally obtained using a beam current of 500 nA.

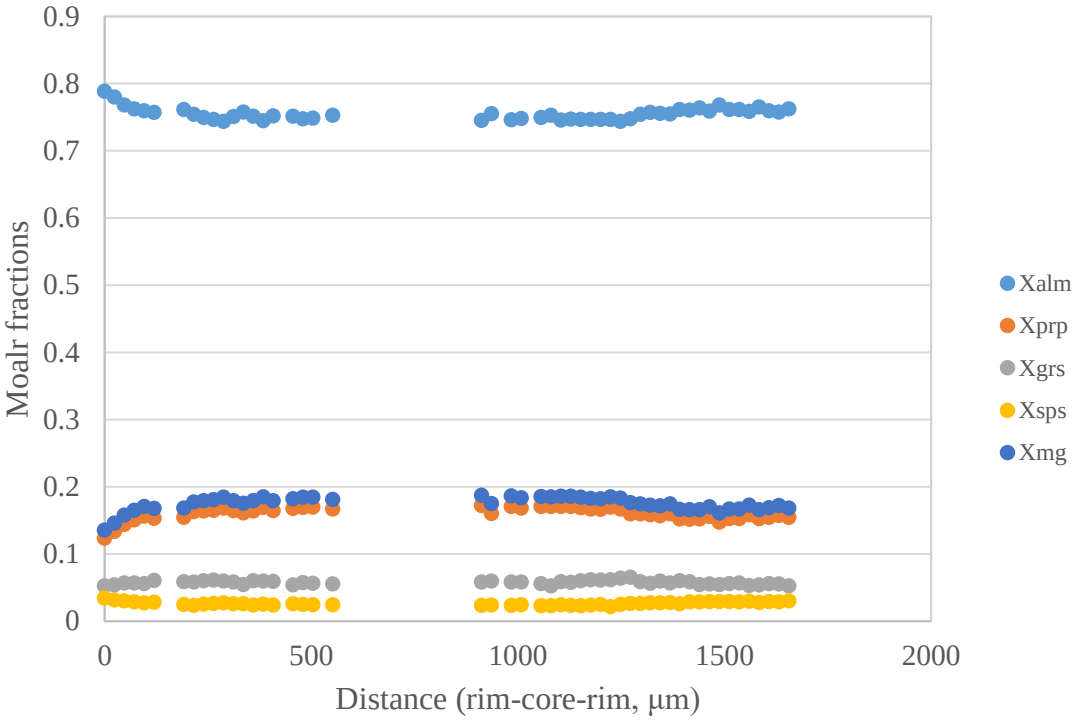

Figure 4-64. Zoning profile of garnet (rim to core to rim). The core is occupied by polymineralic inclusion.

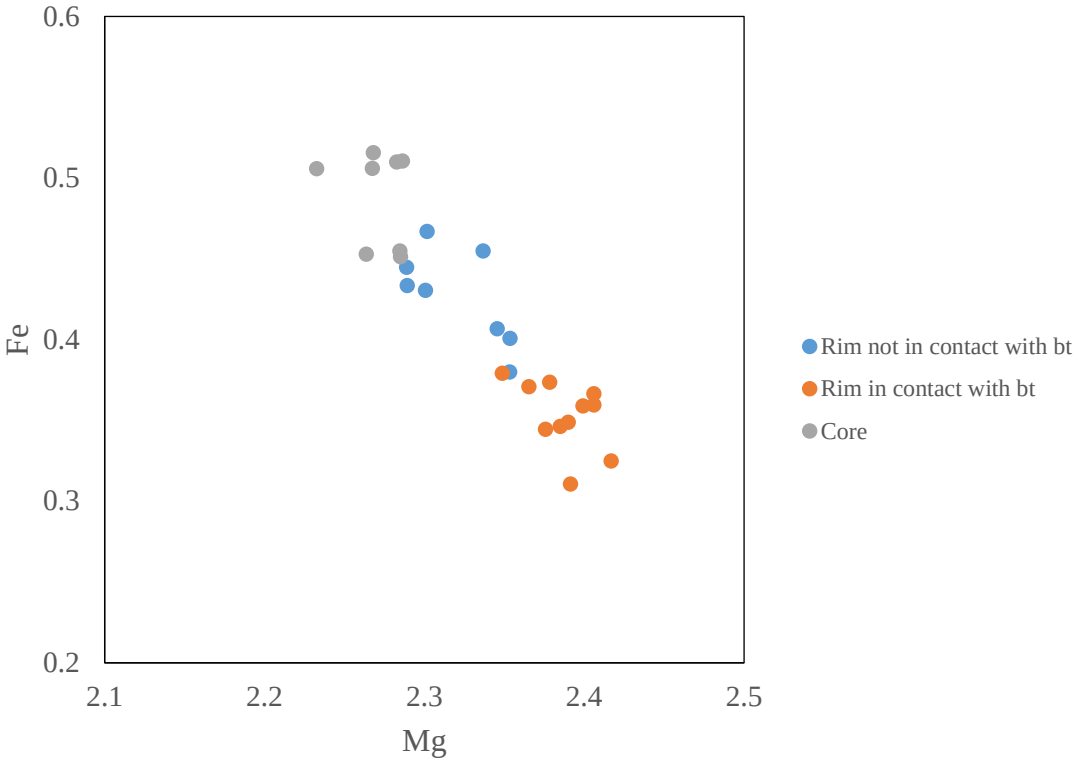

Figure 4-65. Fe versus Mg diagram showing difference in compositions among various parts of garnet.

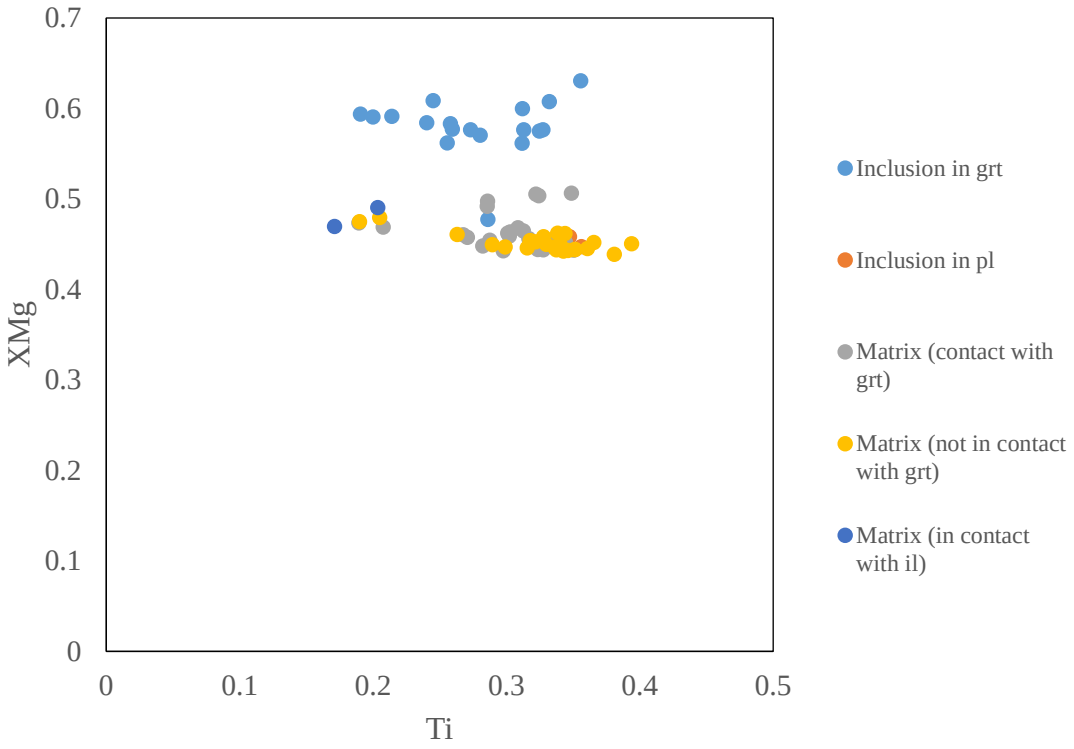

Figure 4-66. X_{Mg} versus Ti diagram showing difference in compositions among various occurrences of biotite.

4.3. Whole-rock Composition of Pelitic Gneiss from Niban Rock

The whole-rock composition of pelitic gneiss from Niban Rock is shown in Table 4-25.

Table 4-25. Whole-rock composition of pelitic gneiss from Niban Rock

	Pelitic
SiO2 (wt%)	64.67
TiO2	1.04
Al2O3	16.39
Fe2O3	10.03
MnO	0.15
MgO	2.56
CaO	1.54
Na2O	1.16
K2O	2.25
P2O5	0.08
Total	99.86
LOI (wt%)	0.46
Sc (ppm)	23.6
V	160.4
Cr	174.8
Ni	86.4
Cu	22.2
Zn	119.2
Rb	85.4
Sr	91.9
Y	33.6
Zr	172.5
Nb	14
Ba	369.6
Hf	6.3
Pb	10

5. DISCUSSION

5.1. Pressure-Temperature Estimations

5.1.1. Niban Rock

P-T condition of Niban Rock has not been well determined in previous studies. Corona does not occur in the Amphibolite-facies zone. Therefore, it is possible that metamorphic temperature is one of factors that controlling formation of corona. In this section, I perform P-T estimation of Niban Rock to compare that of Akarui Point where corona occurs.

Prograde

According to the chemical zoning of garnet, major elements of minerals are already affected by retrograde re-equilibration (Figure 4-64). In this study, I use Zr-in-rutile geothermometer to estimate prograde metamorphic condition. Some of rutile grains directly contacts with kyanite in garnet core (Figure 4-27). This textural relation means Zr concentration in the rutile was that of kyanite stability field. Zircon also included in garnet. Therefore, the equilibrium among rutile, zircon, and quartz can be considered, and this satisfies the condition to apply the Zr-in-rutile geothermometer.

The grain of rutile included in garnet core showed the Zr concentration of 364 – 448 ppm. Applying Zr-in-rutile geothermometer of Tomkins et al. (2007) to the rutile in garnet core yielded 650 – 701 °C, assuming pressure of 6.5 – 14 kbar (kyanite stability

field). This temperature is considered as that at start of garnet formation in the kyanite stability field.

Peak

The peak metamorphic condition was estimated constructing P-T diagrams using the simplified K_2O-Na_2O-CaO-FeO-MgO-MnO-Al_2O_3-TiO_2-SiO_2-H_2O system. P-T pseudosection were computed using the free energy minimization software Perple_X (Connolly, 2005) and the updated thermodynamic data set (hp62ver.dat) of Holland & Powell (2011). The solid-solution models of garnet, biotite, white mica, cordierite, chloritoid, chlorite, staurolite, melt of White et al. (2014) and that of plagioclase and K-feldspar of Fuhrman & Lindsley (1988) were considered in the calculation. The used whole-rock composition was obtained using XRF analysis (Table 4-25). The amount of H_2O was calculated based on stoichiometric relation between K and OH in biotite because biotite is only phase in the studied gneiss as K-bearing or hydrous mineral. According to the mineral chemical analysis, K:OH ratio of bioite is 1.8:4 in atomic ratio. Therefore, the composition input to the calculation was SiO_2, 64.91; TiO_2, 1.04; Al_2O_3, 16.45; FeO, 9.05; MnO, 0.15; MgO, 2.57; CaO, 1.54; Na_2O, 1.16; K_2O, 2.25; H_2O, 0.86 in wt% (normalized to be 100 wt%).

I consider the present matrix mineral assemblage (Grt + Bt + Qtz + Sil + Pl + Ilm) preserves that at peak metamorphic condition. The mineral assemblage appeared on the P-T space of 625 – 720 ℃ and 4.2 – 7.4 kbar (Figure 5-2). Muscovite appeared on high pressure side although any grains of muscovite were not found in the sample. This may be due to difference in amount of H_2O between high-P stage and the peak stage.

Retrograde

Compositional zoning in garnet shows retrograde zoning that is outward decrease in Mg/(Mg+Fe) (Figure 4-64). The compositions of rims of matrix minerals can be considered to have re-equilibrated and preserve the retrograde condition. Garnet-biotite geothermometer of Holdaway (2000) and garnet-plagioclase-sillimanite-quartz geobarometer of Holdaway (2001) were used for the estimation. These geothermobarometers are appropriate for P-T estimation of this sample because compositions of garnet, plagioclase, biotite in this sample and P-T condition expected from previous studies are within the calibration ranges of composition and P-T condition of the geothermobarometers.

The condition of the retrograde stage can be estimated using pairs of maximum and minimum X_{Mg} of matrix biotite, and rim of garnet, and rim of plagioclase, and I obtained 654 – 687 °C and 4.5 – 5.2 kbar as the condition. This P-T condition is included in the range of the peak metamorphic condition estimated using pseudosection. Almost homogeneous zoning in garnet except for extreme rim (Figure 4-64) may correspond to the composition at peak, and only slight effect of re-equilibrium during retrograde stage changed the composition of rims of constituent minerals in the studied gneiss and the composition would be almost same composition as that at peak.

All the results of P-T estimations of Niban Rock is summarized in Figure 5-1.

5.1.2. Akarui Point

P-T condition of Akarui Point has been estimated in some previous studies. However, low-pressure conditions have been never estimated (Figure 2-4). Many FNIs are found in large porphyrobrastic garnet in the sample no. I-030 from Akarui Point (Figure 4-23). The constituent minerals of FNIs are listed in Table 4-2. In two FNIs, Cl-rich scapolite and andalusite directly contact each other (Figure 4-25). There is a possibility of transformation to andalusite from other aluminosilicates. However, sillimanite was also found in a FNI, and thus transformation of aluminosilicate did not occur in the sample. The possibility may be rejected, and the andalusite is considered to be crystallized from melt directly because sillimanite is found in a FNI in the same garnet. Therefore, the andalusite-bearing FNIs are crystallized under andalusite stability field. Scapolite is known as a mineral that is stable at high-T conditions (e.g., Filiberto et al., 2014). According to the diagram of Filiberto et al. (2014), marialite, an endmember of scapolite, is stable at over 700 °C with almost no pressure dependence (Figure 5-1). In FNI, the constituent minerals are not equilibrated as whole (e.g., Hiroi et al., 2019). Previous studies that focus on fluid inclusion or equilibration between mineral and fluid proposed metamorphic condition at lower pressure, and almost isothermal decompression is known among the LHC (e.g., Satish-Kumar et al. 2006; Takahashi & Tsunogae, 2017). The estimated condition by considering stability field of andalusite + Cl-rich scapolite is over 700 °C at $P < 1.6$ kbar based on phase diagram of aluminosilicates of Bohlen et al. (1991) and Holdaway (1971) and that of marialite of Filiberto et al. (2014) (Figure 5-1).

Based on this P-T estimation at low-P condition combined with previous P-T estimations, the metamorphic condition of Akarui Point was almost isothermal decompression in a clockwise P-T path. Comparing to P-T path of Niban Rock, Akarui Point keeps high-T of 700 °C even at low-P. On the other hand, Niban Rock shows quite

lower metamorphic temperature. Therefore, metamorphic conditions are completely different between Niban Rock and Akarui Point.

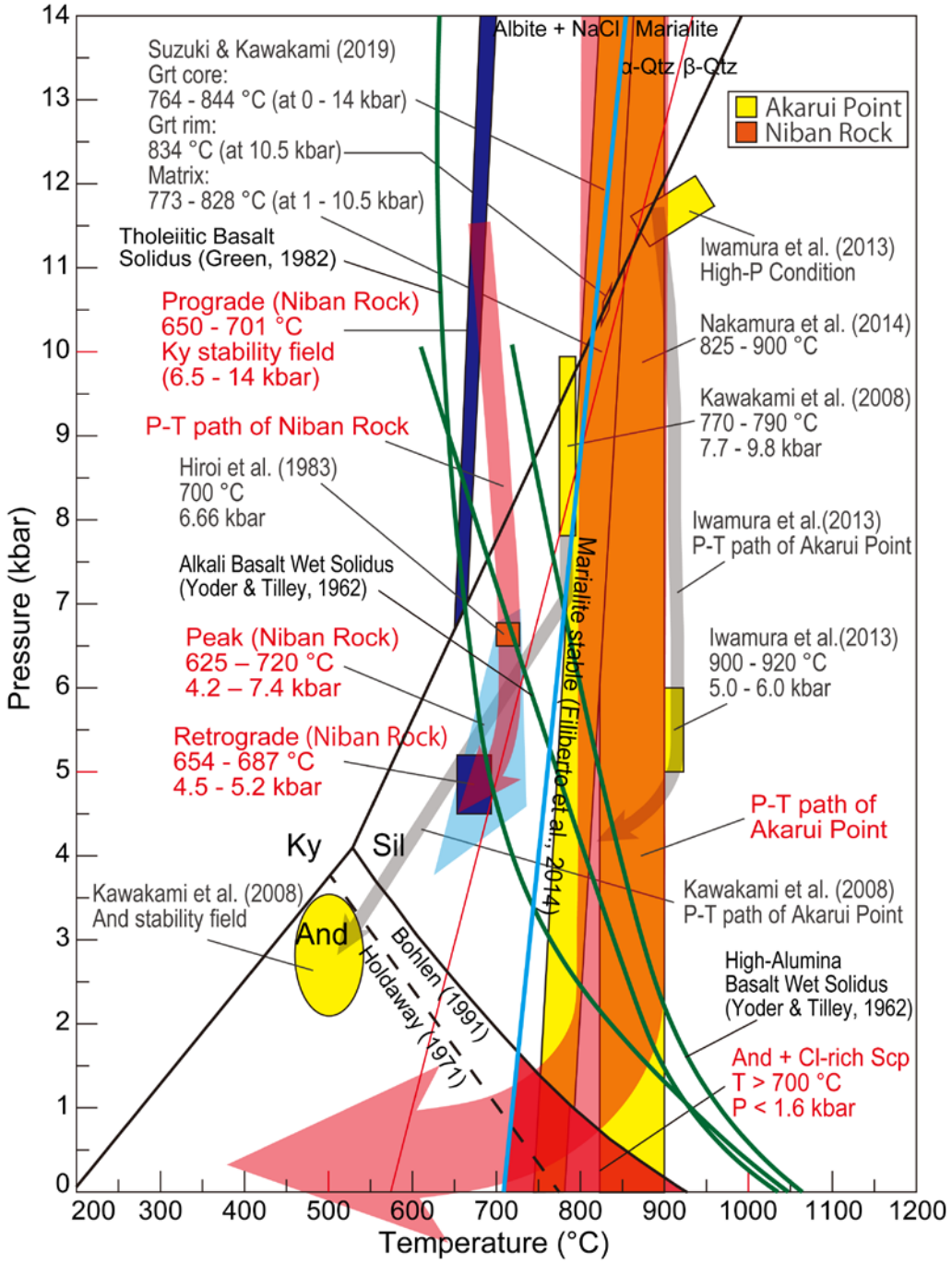

Figure 5-1. P-T diagram showing all the results of P-T estimation of Niban Rock and Akarui Point. Previously estimated conditions are also illustrated. Characters shown in red color are results of this study.

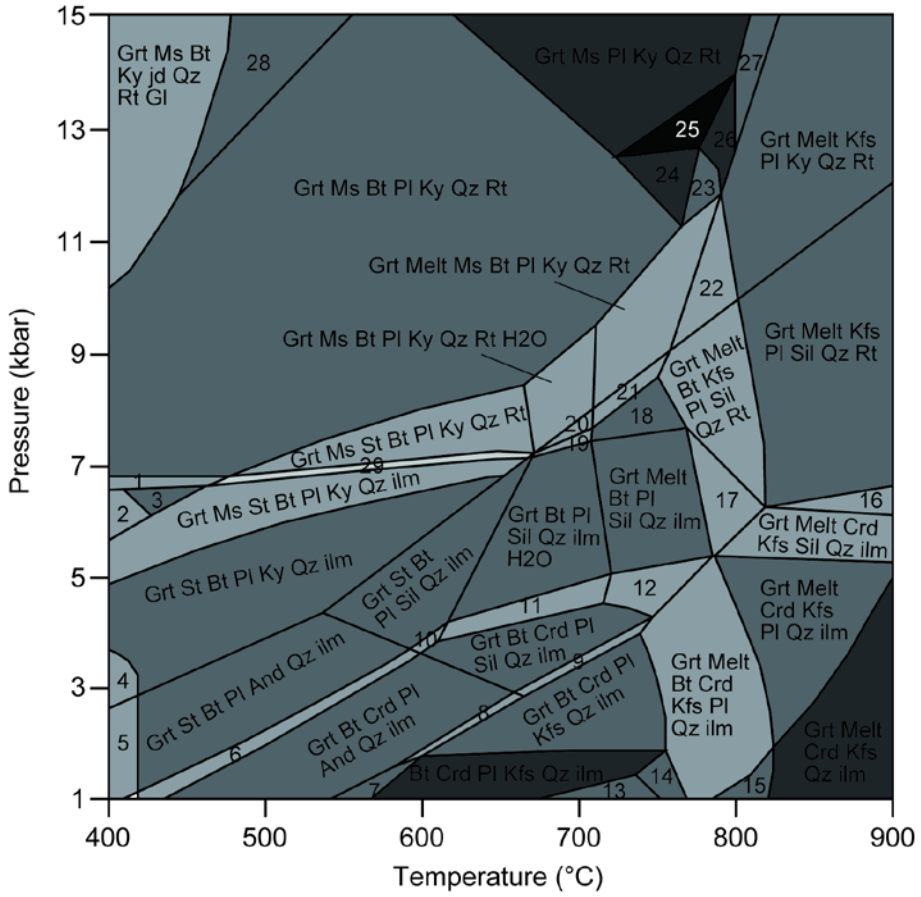

1 Grt, Ms, Bt, Pl, Ky, Qz, Rt, Ilm
2 Grt, Ms, Mica, Bt, Pl, Ky, Qz, Ilm
3 Grt, Mica, Bt, Pl, Ky, Qz, Ilm
4 Grt, St, Bt, Pl, Kfs, Ky, Qz, Ilm
5 Grt, St, Bt, Pl, Kfs, And, Qz, Ilm
6 Grt, St, Bt, Crd, Pl, And, Qz, Ilm
7 Bt, Crd, Pl, Kfs, And, Qz, Ilm
8 Grt, Bt, Crd, Pl, Kfs, And, Qz, Ilm
9 Grt, Bt, Crd, Pl, Kfs, Sil, Qz, Ilm
10 Grt, St, Bt, Crd, Pl, Sil, Qz, Ilm
11 Grt, Bt, Crd, Pl, Sil, Qz, Ilm, H2O
12 Grr, Melt, Bt, Crd, Pl, Sil, Qz, Ilm
13 Bt, Crd, Pl, Kfs, Qz, Ilm, H2O
14 Melt, Bt, Crd, Pl, Kfs, Qz, Ilm
15 Grt, Melt, Bt, Crd, Kfs, Qz, Ilm
16 Grt, Melt, Pl, Kfs, Sil, Qz, Rt, Ilm
17 Grt, Melt, Bt, Pl, Kfs, Sil, Qz, Rt, Ilm
18 Grt, Melt, Bt, Kfs, Sil, Qz, Rt
19 Grt, Bt, Pl, Sil, Qz, Rt, Ilm, H2O
20 Grt, Ms, Bt, Pl, Sil, Qz, Rt, H2O
21 Grt, Melt, Ms, Bt, Kfs, Sil, Qz, Rt
22 Grt, Melt, Bt, Pl, Kfs, Ky, Qz, Rt
23 Grt, Melt, Ms, Bt, Pl, Qz, Rt
24 Grt, Ms, Bt, Pl, Qz, Rt
25 Grt, Ms, Pl, Qz, Rt
26 Grt, Melt, Ms, Pl, Qz, Rt
27 Grt, Melt, Ms, Kfs, Ky, Qz, Rt
28 Grt, Ms, Bt, Ky, Jd, Qz, Rt
29 Grt, Ms, St, Bt, Pl, Ky, Qz, Rt, Ilm

Figure 5-2. Pseudosection of pelitic gneiss from Niban Rock.

5.2. Determination of Reactants

As pointed in the introduction section, determination of reactants has sorely been depended on textural observation in previous studies. In this section, I determine reactants by focusing chemical compositions and textures. I found that amphibole presents in corona-bearing samples in the most cases based on compilation of description in previous studies and textural observation in this study. Garnets containing FNIs are also surrounded by coronas as mentioned below. Therefore, I deal with garnet, melt, and amphiboles in this section.

5.2.1. Garnet

It seems clear that garnet is one of reactants of corona-forming reaction because corona develops around garnet. However, I cannot eliminate the possibility that the surface of garnet was the field of nucleation of the coronal minerals, and the evidence of consumption of garnet due to formation of corona has not been shown in previous studies.

In the garnet of I-122 from Rundvågshetta, Cr-zoning shows polygonal shape (Figure 4-49). This would be a euhedral shape of garnet, as judged from its shape. In some place of the examined grain, the zoning is cut by coronal orthopyroxene + plagioclase symplectite (Figure 4-49). The polygonal zoning of Cr may be complete shape when garnet grew. Therefore, this is one of evidence for consumption of garnet by corona-forming reaction.

At the rim of garnet in I-030 from Akarui Point, inclusion hornblende partially exposes to corona (Figure 4-24). The hornblende contains higher Cl content than

completely included hornblende (Figure 4-62). This is considered as a result of re-expose to Cl-bearing fluid or melt and additional incorporation of Cl during corona formation that consumes garnet. The origin of Cl will be mentioned later. Therefore, I consider that garnet is one of reactants.

5.2.2. Melt

Occurrence of FNIs in garnet in mafic gneiss from the LHC was reported only three cases from Skallevikshalsen, Rundvågshetta, and Austhovde in previous studies. I confirmed that the garnets in the samples from Rundvågshetta and Austhovde are surrounded by symplectitic coronas based on available photomicrographs in Yanagi et al. (2011) and Hiroi et al. (2016). Photomicrograph of texture of the samples from Skallevikshalsen was not available, and thus I could not check. In this study, I found FNIs in garnet in mafic gneisses from Akarui Point, Skallen, and Skallevikshalsen, as described before (Figures 4-12, 4-14, 4-25). Garnets in these samples also have corona (Figures 4-11, 4-13, 4-23). In addition, I did not find FNIs in corona-free garnet. Therefore, melt can be a candidate of reactants.

However, it is difficult to demonstrate after solidification of melt that melt react with garnet and other reactants to form corona if FNIs were not included in garnet. The constituent minerals of FNIs in garnet in I-030 from Akarui Point are rich in Cl (Table 4-24), and thus the melt coexisted with growing garnet was rich in Cl. If the Cl-rich melt react with garnet and other reactants to form corona, Cl should flow out to matrix from reaction front because most coronal minerals (e.g., orthopyroxene, plagioclase, gedrite) cannot incorporate Cl into their structures. In generally, volume diffusion of most

elements in amphibole, the most common matrix mineral in corona-bearing rocks, is more rapid than garnet (e.g., Spear, 1993). Major elements in hornblende are expected to have already affected by retrograde metamorphism because even all examined garnets surrounded by coronas show retrograde zoning. Cl can be incorporated in amphibole, and most major rock-forming minerals such as garnet, plagioclase, pyroxene in the samples examined in this study do not contain Cl. Therefore, there is no possibility to exchange Cl between amphibole and other minerals. Thus, I focus on Cl in amphibole to detect the evidence that melt is a reactant.

The rims of matrix amphiboles in the selected corona-bearing samples no. I-030 from Akarui Point, I-008 from Akarui Point, I-518 from East Ongul Island, and 93012301B from Austhovde show decrease in Cl with distance from corona (Figures 4-55, 4-56, 4-57, 4-62). The matrix amphiboles in these samples also contain Cl in their cores, and the concentration is lower than their rims (Figures 4-55, 4-56, 4-57, 4-62). If the Cl zoning was due to infiltration of exotic Cl-bearing fluid, Cl content in the rim will be same among all grains, and such gradual decrease in Cl in rims of amphibole with distance from corona would not be formed.

However, one possibility that the gradual decrease in Cl concentration is due to original gradual increase in Mg concentration remains. As mentioned in the introduction section, the nature of Mg-Cl avoidance in amphibole, i.e., Mg is strongly eliminated by Cl or Cl can be incorporated according to Mg concentration, is unclear. If gradual decrease in Cl is result of infiltration of Cl-bearing fluid into gneisses after formation of corona, corona formation would make Mg gradient on the matrix amphibole. Therefore, investigation of Cl-free corona-bearing sample is valid to check the possibility. The elemental mapping and quantitative chemical analysis of the selected Cl-free corona-

bearing sample I-122 from Rundvågshetta show no core-rim zonation in terms of Mg, as shown in the result section (Figure 4-60). Therefore, gradual decrease in Cl would not be due to original gradual increase in Mg.

In addition, I examined Cl-bearing corona-free sample no. 93012301C from Austhovde to confirm no zoning was formed due to no consumption of Cl-bearing amphibole. Its elemental mapping and quantitative chemical analysis show that amphibole in the matrix is almost homogeneous in one grain (Figure 4-59).

Throughout comparison among six samples of three types with regard to Cl concentration and presence of corona, the Cl zoning in matrix amphibole and Cl gradient in rims of amphibole are characteristic to corona-bearing samples, and the zoning is not controlled by original Mg zoning in amphibole. Therefore, I consider that the Cl flowed from corona side, and melt is one of reactants of coronal formation. Partially exposed inclusion hornblende in garnet in I-030 from Akarui Point was richer in Cl than completely included hornblende. This means that additional incorporation of Cl was taken place when the hornblende exposed to melt during consumption of garnet by corona formation. This also suggests that melt occupied the place of present corona and melt reacted with garnet.

Water-saturated basalt solidus (e.g., Yoder & Tilley, 1962; Green, 1982) locates almost between the temperatures of Niban Rock and Akarui Point, and thus the metamorphic condition of Akarui Point attained the temperature high enough for partial melting (Figure 5-1). Considering the common feature between presence of FNIs and coronas, garnet grew under melt-existing environment and the melt is one of reactants of coronal formation.

5.2.3. Calcic amphibole

I already demonstrated above that garnet and melt are reactants of corona formation. However, if only garnet and melt were reactants, corona would form around FNIs. FNIs in garnet do not show corona around them (Figure 4-25), and thus additional reactant is required to make corona. Calcic amphibole is the most common matrix mineral in the examined rocks and is obviously one of reactants based on textural observation. The inferred corona-forming reaction based on textural observation only is garnet + hornblende = corona. However, corona also does not develop around inclusion hornblende in garnet (Figures 4-23, 4-24). In I-122 from Rundvågshetta, matrix hornblende is directly in contact with garnet in part (Figure 4-17). Therefore, reaction among garnet, hornblende, and melt make corona. The Cl in flow from corona side may contain not only that in Cl-rich melt but also that released by breakdown of matrix hornblende at the corona formation.

5.3. Possible Scenario of Formation of Corona

As discussed before, this study can provide a scenario of formation of the coronas in the LHC that is common to all the examined coronas. The possible scenario that is common to all the coronas in the LHC is illustrated in Figure 5-3. If hornblende is Cl-free, explanation for Cl just be subtracted (e.g., for I-122 from Rundvågshetta).

At the stage before garnet growth and partial melting, hornblende would contain Cl before garnet growth because inclusion and matrix hornblendes have Cl-bearing cores. After start of garnet growth, Cl-rich melt coexisted with the growing garnet because scapolite, biotite, and apatite composing FNIs found from Akarui Point contain much amounts of Cl. The inclusion amphibole in garnet shows Cl-rich rim and Cl-poor core. This is considered to have affected by the Cl-rich melt.

The origin of Cl in the Cl-rich melt has two possibilities. One of the possibilities of the origin is consumption of Cl-bearing amphibole to make melt. If I think about it logically, it is high possibility because the matrix minerals should be consumed when garnet growth to make space for garnet. Hornblende is the most common mineral in the matrix among all the examined rocks. Plagioclase is also common minerals in the matrix. The inclusion plagioclase in garnet of I-030 from Akarui Point is smaller amount than inclusion hornblende. In generally, plagioclase starts melting at lower temperature than hornblende (Yoder & Tilley, 1962). Therefore, the reaction Cl-bearing hornblende + plagioclase = garnet + Cl-bearing melt can be considered. Another possibility is that infiltration of Cl-rich fluid had continued from before start of partial melting and garnet growth to end of them. However, the possibility is unlikely because inclusion hornblende in I-008 and I-030 from Akarui Point have higher Cl in their rims than that in the matrix

far from corona. If infiltration of Cl continued long time, matrix hornblende likely obtains more Cl than inclusion hornblende because inclusion hornblende is already isolated from Cl-rich melt or fluid by host garnet. Therefore, in the cases examined in this study, it is likely that hornblende that is originally present in the rocks before garnet formation contained Cl. It is still unclear that the Cl in hornblende is infiltration of Cl-bearing fluid at the early stage of metamorphism or originally contained in the protolith of the mafic gneiss.

The Cl in the melt was supplied by melting of matrix amphibole, not by infiltration of Cl-rich fluid, because the matrix amphibole contains Cl in its core that may be originally contained during prograde stage before initiation of garnet growth. With growth of garnet by consuming matrix amphibole, remaining component will concentrate into melt, and some part of melt was trapped as melt inclusion in garnet or may gather around garnet. The inclusion amphibole in garnet partially exposed from host garnet to corona is richer in Cl than non-exposed inclusion amphibole as observed in the Cl mapping. Therefore, reaction among garnet, melt, and matrix amphibole made corona after garnet growth, i.e., after peak metamorphism. The corona-constituent minerals, i.e., gedrite and plagioclase, cannot contain Cl in their structure, and thus Cl and remaining components would be released as fluid, and hence the fluid made a gradual decrease in Cl in rims of matrix amphibole with distance from corona.

I conclude that melt should be taken account into corona-forming reaction, and the difference between corona-bearing and corona-free gneisses are whether the gneiss has an experience of partial melting during garnet formation or not.

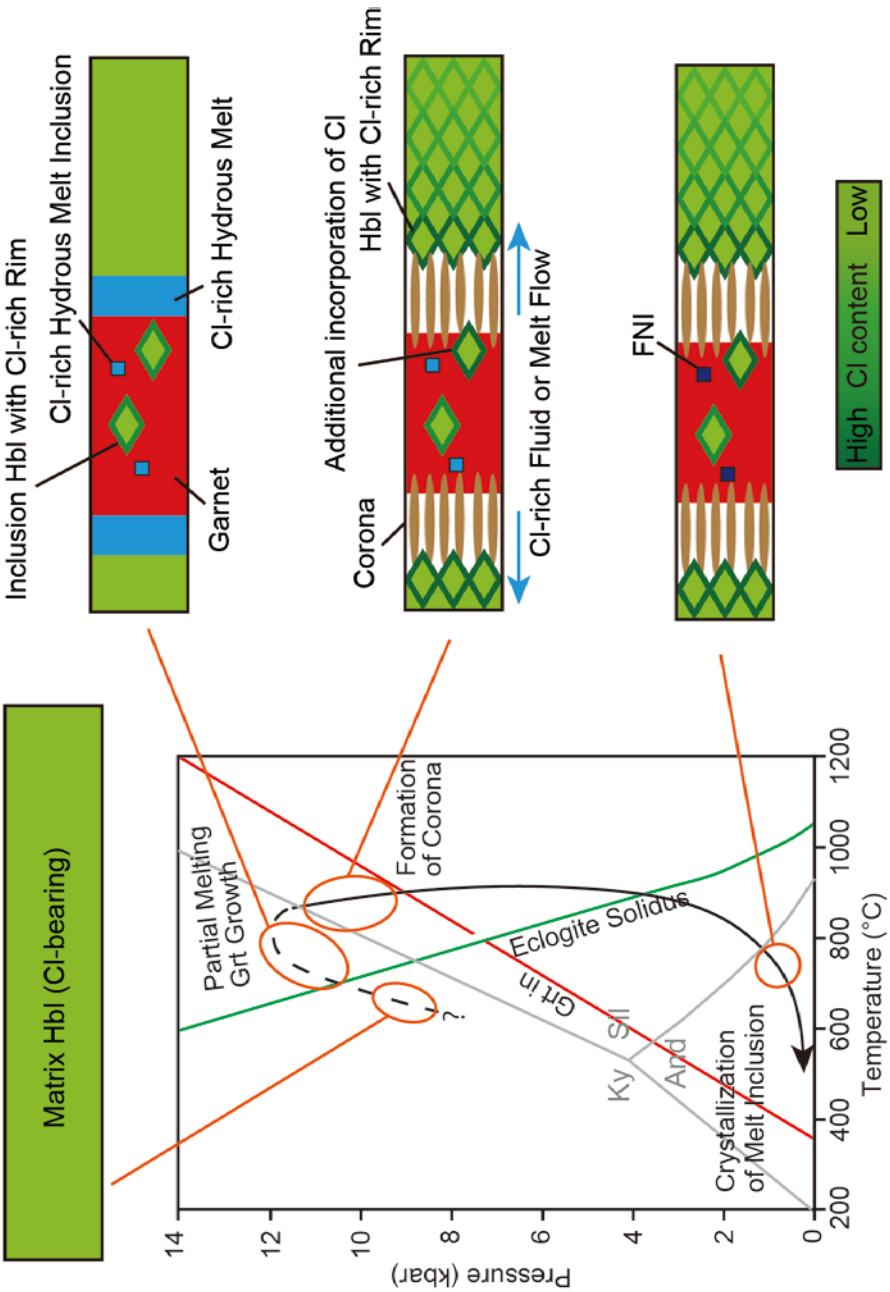

Figure 5-3. Possible scenario of formation of corona. P-T path is drawn based on that of Akarui Point. Triple point of aluminosilicates is after Bohlen (1991). Eclogite solidus is after Yoder & Tilley (1962). Garnet-in is defined by the reaction orthopyroxene + plagioclase + spinel = garnet + clinopyroxene shown in Ringwood (1975).

6. CONCLUSIONS

- Garnet preserves polygonal shape of Cr-zoning even though major elements are diffused or affected by retrograde stage.
- Calcic amphiboles in corona-bearing samples have Cl-rich rim and Cl-poor core. Cl in the rim decrease with distance from corona.
- Garnet and calcic amphibole are determined as reactants of corona-forming reaction.
- Metamorphic conditions at prograde stage, peak, and retrograde stage of Niban Rock were estimated using Zr-in-rutile geothermometer, pseudosection, garnet-biotite geothermometer, and garnet-silimanite-plagioclase-quartz geobarometer.
- Metamorphic condition at low pressure of Akarui Point is determined based on mineral assemblage in felsite-nanogranite inclusion of andalusite + Cl-rich scapolite.
- Cl-rich melt is generated during garnet formation by consuming Cl-bearing calcic amphibole.
- Melt should be taken into account for reactants of coronal formation.
- High temperature enough for melting during garnet formation is required for coronal formation.

7. ACKNOWLEDGMENTS

I am grateful to Takeshi Ikeda (Kyushu University) for critical discussions, constructive comments, encouragements, and providing samples. Atsushi Toramaru (Kyushu University) is thanked for development of research environment, critical discussions, constructive comments, and encouragements. Tomoharu Miyamoto (Kyushu University) is thanked for development of research environment, critical discussions, constructive comments, encouragements, providing samples, and operation of X-ray fluorescence spectrometer. Tetsuo Kawakami (Kyoto University) is thanked for careful reading and constructive review of the manuscript. I thank Tomokazu Hokada (National Institute of Polar Research), Yoichi Motoyoshi (National Institute of Polar Research), and Yoshikuni Hiroi (Chiba University) for providing samples. I acknowledge Tomoaki Kubo (Kyushu University) and Takaaki Noguchi (Kyushu University) for use of laser Raman microspectrometer and advising on the analysis. Kazuhiko Shimada (Kyushu University) is thanked for technical support with the mineral chemical analyses. Hayato Yodoya (Kyushu University) is thanked for assistance for sample preparation for whole-rock chemical analysis. I thank members of Group of Petrology and Volcanology for encouragement and members of department office for office processing.

This study was financially supported by the Late Professor Tatsuro Matsumoto Scholarship no. MT16010 to Yuki Mori, JSPS KAKENHI Grant Number JP C25400518 to Takeshi Ikeda, and National Institute of Polar Research (NIPR) through General Collaboration Project no. 28-23 to Takeshi Ikeda and no. 31-24 to Yuki Mori and Takeshi Ikeda.

8. REFERENCES

Arima, K., Ikeda, T., and Miyazaki, K. (2011) Reaction microstructures in corundum- and kyanite-bearing mafic mylonites from the Takahama metamorphic rocks, western Kyushu, Southwest Japan. Island Arc 20, 248–258.

Ashworth, J.R. and Birdi, J.J. (1990) Diffusion modelling of coronas around olivine in an open system. Geochimica et Cosmochimica Acta, 54, 2389–2401.

Bohlen, S.R., Montana, A., and Kerrick, D.M. (1991) Precise determinations of the equilibria kyanite ⇌ sillimanite and kyanite ⇌ andalusite and a revised triple point for Al2SiO5 polymorphs. American Mineralogist, 76, 677–680.

Chowdhury, P., Talukdar, M., Sengupta, P., Sanyal, S. and Mukhopadhyay, D. (2013) Controls of P–T path and element mobility on the formation of corundum pseudomorphs in Paleoproterozoic high–pressure anorthosite from Sittampundi, Tamil Nadu, India. American Mineralogist, 98, 1725–1737.

Connolly, J.A.D (2005) Computation of phase equilibria by linear programming: A tool for geodynamic modeling and its application to subduction zone decarbonation. Earth and Planetary Science Letters, 236, 524–541.

Dale, J., Holland, T.J.B. and Powell, R. (2000) Hornblende–garnet–plagioclase thermobarometry: a natural assemblage calibration of the thermodynamics of hornblende. Contributions to Mineralogy and Petrology, 140, 353–362.

de Capitani, C., and Petrakakis, K. (2010) The computation of equilibrium assemblage diagrams with Theriak/Domino software. American Mineralogist, 95, 1006–1016.

Droop, G.T.R. (1987) A general equation for estimating Fe^{3+} concentrations in

ferromagnesian silicates and oxides from microprobe analyses, using stoichiometric criteria. Mineralogical Magazine, 51, 431–435.

Dunkley, D.J., Shiraishi, K., Motoyoshi, Y., Tsunogae, T., Miyamoto, T., Hiroi, Y., and Carson, C.J. (2014) Deconstructing the Lützow-Holm Complex with zircon geochronology. Abstract of 7th International SHRIMP Workshop Program, pp. 116–121.

Faryad, S.W., and Fišera, M. (2015) Olivine-bearing symplectites in fractured garnet from eclogite, Moldanubian Zone (Bohemian Massif) – a short-lived, granulite facies event. Journal of Metamorphic Geology, 33, 597–612.

Ferry, J.M., and Watson, E.B. (2007) New thermodynamic models and revised calibrations for the Ti-in-zircon and Zr-in-rutile thermometers. Contributions to Mineralogy and Petrology, 154, 429–437.

Filiberto, J., Treiman, A.H., Giesting, P.A., Goodrich, C.A., and Gross, J. (2014) High-temperature chlorine-rich fluid in the martian crust: A precursor to habitability. Earth and Planetary Science Letters, 401, 110–115.

Fisher, G.W. (1989) Matrix analysis of metamorphic mineral assemblages and reactions. Contributions to Mineralogy and Petrology, 102, 69–77.

Fraser, G., McDougall, I., Ellis, D.J. and Williams, I.S. (2000) Timing and rate of isothermal decompression in Pan–African granulites from Rundvågshetta, East Antarctica. Journal of Metamorphic Geology, 18, 441–454.

Fuhrman, M.L. and Lindsley, D.H. (1988) Ternary-feldspar modeling and thermometry. American Mineralogist, 73, 201–215.

Fukuyama, M., Nishiyama, T., Urata, K. and Mori, Y. (2006) Steady–diffusion modelling of a reaction zone between a metamorphosed basic dyke and a marble from

Hirao–dai, Fukuoka, Japan. Journal of Metamorphic Geology, 24, 153–168.

Grant, S.M. (1988) Diffusion models for corona formation in metagabbros from the Western Grenville Province, Canada. Contributions to Mineralogy and Petrology, 98, 49–63.

Green, T.H. (1982) Anatexis of mafic crust and high pressure crystallization of andesite. In: Thorpe, R.S. (Ed.), Andesites. Wiley, London, pp. 465–487.

Higashino, F., Kawakami, T., Tsuchiya, N., Satish-Kumar, M., Ishikawa, M., Grantham, G., Sakata, S., and Hirata, M. (2019) Brine Infiltration in the Middle to Lower Crust in a Collision Zone: Mass Transfer and Microtexture Development Through Wet Grain–Boundary Diffusion. Journal of Petrology, 60, 329–358.

Hiroi, Y., Hokada, T., Kato, M., Yanagi, A., et al. (2019) Felsite–nanogranite inclusions and three Al2SiO5 polymorphs in the same garnet in ultrahigh–temperature granulites from Rundvågshetta, Lützow–Holm Complex, East Antarctica. Journal of Mineralogical and Petrological Sciences, 114, 60–78.

Hiroi, Y., Motoyoshi, Y., Ellis, D.J., Shiraishi, K. and Kondo, Y. (1997) The significance of phosphorus zonation in garnet from high grade pelitic rocks: A new indicator of partial melting. The Antarctic region: Geological evolution and processes, Terra Antarctica Publication, Siena, 73–77.

Hiroi, Y., Motoyoshi, Y., Ishikawa, N., Hokada, T., and Shiraishi, K. (2008) Origin of xenocrystic garnet and kyanite in clinopyroxene-hornblende-bearing adakitic meta-tonalites from Cape Hinode, Prince Olav Coast, East Antarctica. In: Satish-Kumar, M., Motoyoshi, Y., Osanai, Y., Hiroi, Y. and Shiraishi, K. (eds) Geodynamic Evolution of East Antarctica: a key to the East-West Gondwana Connection. Geology Society, London, Special Publications, 308, 333–350.

Hiroi, Y., Motoyoshi, Y., Satish-Kumar, M., Kagashima, S., Suda, Y., and Ishikawa N (2006) Granulites from Cape Hinode in the amphibolite-facies eastern part of Prince Olav Coast, East Antarctica: New evidence for allochthonous block in the Lützow-Holm Complex. Polar Geoscience, 19, 89–108.

Hiroi, Y., Shiraishi, K. and Motoyoshi, Y. (1991) Late Proterozoic paired metamorphic complexes in East Antarctica, with special reference to the tectonic significance of ultramafic rocks, In: Thomson, M.R.A, Crame, J.A. and Thomson, J.W. (Eds.) Geological Evolution of Antarctica. Cambridge University Press, Cambridge, 83–87.

Hiroi, Y., Shiraishi, K., Motoyoshi, Y. and Katsushima, T. (1987) Progressive metamorphism of calc–silicate rocks from the Prince Olav and Soya Coasts, East Antarctica. Proceedings of the NIPR Symposium on Antarctic Geosciences, 1, 73–97.

Hiroi, Y., Shiraishi, K., Motoyoshi, Y., Kanisawa, S., Yanai, K. and Kizaki, K. (1986) Mode of occurrence, bulk chemical compositions, and mineral textures of ultramafic rocks in the Lützow–Holm Complex, East Antarctica. Memoirs of National Institute of Polar Research, Special Issue 43, 62–84.

Hiroi, Y., Shiraishi, K., Nakai, Y., Kano, T. and Yoshikura, S. (1983a) Geology and petrology of Prince Olav Coast, East Antarctica. In Antarctic Earth Science (Oliver, R.L., James, P.R. and Jago, J.B. Eds.). Australian Academy of Science, Canberra, 32–35.

Hiroi, Y., Tabata, E., Hokada, T., Motoyoshi, Y., and Shiraishi, K. (2016) New occurrence of felsite inclusions in granulites from Lützow-Holm Complex, Antarctica: from Austhovde and Botnnuten. The 7th symposium on Polar Science Abstract.

Holdaway, M. J. (1971). Stability of andalusite and the aluminum silicate phase diagram. American Journal of Science, 271, 97–131.

Holdaway, M.J. (2000) Application of new experimental and garnet Margules data to the garnet–biotite geothermometer. American Mineralogist 85, 881–892.

Holdaway, M.J. (2001) Recalibration of the GASP geobarometer in light of recent garnet and plagioclase activity models and versions of the garnet-biotite geothermometer. American Mineralogist 86, 1117–1129.

Holland, T.J.B. and Blundy, J. (1994) Non–ideal interactions in calcic amphiboles and their bearing on amphibole–plagioclase thermometry. Contributions to Mineralogy and Petrology, 116, 433–447.

Holland, T.J.B. and Powell, R. (2011) An improved and extended internally consistent thermodynamic dataset for phases of petrological interest, involving a new equation of state for solids. Journal of Metamorphic Geology, 29, 333–383.

Ikeda, T. and Shimada, A. (2015) Isothermal decompression of Lützow-Holm Complex, East Antarctica, deduced from above-solidus corona microstructure, IAGR Conference Series No. 21, pp. 43.

Iwamura, S., Tsunogae, T., Kato, M., Koizumi, T. and Dunkley, D.J. (2013) Petrology and phase equilibrium modeling of spinel–sapphirine–bearing mafic granulite from Akarui Point, Lützow–Holm Complex, East Antarctica: Implications for the P–T path. Journal of Mineralogical and Petrological Sciences, 108, 345–350.

Kawakami, T. and Hokada, T. (2010) Linking P–T path with development of discontinuous phosphorous zoning in garnet during high–temperature metamorphism — an example from Lützow–Holm complex, East Antarctica. Journal of Mineralogical and Petrological Sciences, 105, 175–186.

Kawakami, T. and Motoyoshi, Y. (2004) Timing of attainment of the spinel + quartz coexistence in garnet–sillimanite leucogneiss from Skallevikshalsen, Lützow–Holm Complex, East Antarctica. Journal of Mineralogical and Petrological Sciences, 99, 311–319.

Kawakami, T., Grew, E.S., Motoyoshi, Y., Shearer, C.K., et al. (2008) Kornerupine sensu stricto associated with mafic and ultramafic rocks in the Lützow–Holm Complex at Akarui Point, East Antarctica: What is the source of boron? In: Geodynamic Evolution of East Antarctica: A Key to the East–West Gondwana Connection (Satish–Kumar, M., Motoyoshi, Y., Osanai, Y., Hiroi, Y. and Shiraishi, K. Eds.). Geological Society, London, Special Publications, 308, 351–375.

Kawasaki, T., Ishikawa, M. and Motoyoshi, Y. (1993) A preliminary report on cordierite-bearing assemblages from Rundvågshetta, Lützow-Holm Bay, East Antarctica: evidence for a decompressional P–T path?, Proceedings of NIPR Symposium of Antarctic Geosciences, 6, 47–56.

Kawasaki, T., Nakano, N. and Osanai, Y. (2011) Osumilite and a spinel + quartz association in garnet–sillimanite gneiss from Rundvågshetta, Lützow–Holm Complex, East Antarctica. Gondwana Research, 19, 430–445.

Kizaki, K., Hiroi, Y., Kanisawa, S., Explanatory text of geological map of Niban Rock, Antarctica. Antarctic Geological Map Series, Sheet 17 Niban Rock. NIPR, Tokyo, 1983.

Koizumi, T., Tsunogae, T., Dunkley, D.J., Miyamoto, T., and Kato, M (2014) Field occurrence of high-grade metamorphic rocks at Telen in the Lützow-Holm Complex, East Antarctica. Earth Evolution Sciences, 8, 3–12.

Kullerud, K. and Erambert, M. (1999) Cl-scapolite, Cl-amphibole, and plagioclase

equilibria in ductile shear zones at Nusfjord, Lofoten, Norway: implications for fluid compositional evolution during fluid-mineral interaction in the deep crust. Geochimica et Cosmochimica Acta, 63, 3829–3844.

Li, B., Ge, J., and Zhang, B. (2018) Diffusion in garnet: a review. Acta Geochim., 17, 19–31.

Mi, J.-X, and Pan, Y. (2018) Halogen-Rich Minerals: Crystal Chemistry and Geological Significances. In: Harlov, D.E. and Aranovich, A. (eds.) The Role of Halogens in Terrestrial and Extraterrestrial Geochemical Processes, Springer, 123–184.

Mori, Y., and Ikeda, T. (2018) Formation of triple–layer coronas between corundum and hornblende from the Lützow–Holm Complex at Akarui Point, East Antarctica. Journal of Mineralogical and Petrological Sciences, 113, 68–81.

Morrison, J. (1991) Compositional constraints on the incorporation of CI into amphiboles. American Mineralogist, 76, 1920–1930.

Motoyoshi, Y., Matsubara, S., Matsueda, H., and Matsumoto, Y. (1985) Garnet–sillimanitegneiss from the Lützow-Holm Complex, East Antarctica. Memoirs of National Institute for Polar Research Special Issue, 37, pp. 82–94.

Munoz, J.L. (1984) F-OH and Cl-OH exchange in micas with applications to hydrothermal ore deposits. Reviews in Mineralogy, 13, 469–494.

Nakada, S. (1985) X-ray fluorescence analysis of trace elements in silicate rocks using fused disk samples. Science Reports, Department of Geology, Kyushu University, 14, 117–127 (in Japanese with English abstract).

Nakada, S., Yanagi, T., Maeda, S., Fang, D., Yamaguchi, M. (1985) X-ray fluorescence analysis of major elements in silicate rocks. Science Reports, Department of Geology, Kyushu University, 14, 103–115 (in Japanese with English abstract).

Nakamura, A., Kitamura, M. and Kawakami, T. (2014) Microstructural records of multiple retrograde local H2O supplement in the pelitic gneiss, Lützow–Holm Complex at Akarui Point, East Antarctica. Mineralogy and Petrology, 108, 177–186.

Nakamura, D. (2002) Kinetics of decompressional reactions in eclogitic rocks – formation of plagioclase coronas around kyanite. Journal of Metamorphic Geology, 20, 325–333.

Nakano, N., Osanai, Y., Baba, S., Adachi, T., Hokada, T., and Toyoshima, T (2011) Inferred ultrahigh-temperature metamorphism of amphibolitized olivine granulite from the Sør Rondane Mountains, East Antarctica, Polar Science, 5, 345–359.

Nakano, N., Osanai, Y., Owada, M., Nam, T.N., Sharusiri, P., and Khamphavong, K. (2013) Tectonic evolution of high-grade metamorphic terranes in central Vietnam: Constraints from large-scale monazite geochronology. Journal of Asian Earth Sciences, 73, 520–539.

Nishiyama, T. (1983) Steady diffusion model for olivine–plagioclase corona growth. Geochimica et Cosmochimica Acta, 47, 283–294.

Nogi, Y., Jokat, W., Kitada, K., and Stenhage, D. (2013) Geological structures inferred from airborne geophysical surveys around Lützow-Holm Bay, East Antarctica. Precambrian Research, 234, 279–287.

Osanai, Y., Toyoshima, T., Owada, M. et al., 2004. Geological Map of Skallen, East Antarctica, Revised version. Antarctic Geologic Map Series, Sheet 39 (with explanatory text), 23 pp. National Institute of Polar Research, Tokyo.

Ringwood, A.E., Composition and petrology of the earth's mantle. McGraw-Hill Inc.

Santosh, M. and Sajeev, K. (2006) Anticlockwise evolution of ultrahigh–temperature granulites within continental collision zone in southern India. Lithos, 92, 447–464.

Satish-Kumar, M., Hermann, J., Tsunogae, T. and Osanai, Y. (2006) Carbonation of Cl–rich scapolite boudins in Skallen, East Antarctica: evidence for changing fluid condition in the continental crust. Journal of Metamorphic Geology, 24, 241–261.

Schantl, P., Hauzenberger, C., Finger, F., Müller, T., and Linner, M. (2019) New evidence for the prograde and retrograde PT-path of high-pressure granulites, Moldanubian Zone, Lower Austria, by Zr-in-rutile thermometry and garnet diffusion modelling. Lithos, 342–343, 420–439.

Shiraishi, K., Ellis, D.J., Hiroi, Y., Fanning, C.M., Motoyoshi, Y. and Nakai, Y. (1994) Cambrian orogenic belt in East Antarctica and Sri Lanka: Implications for Gondwana assembly. Journal of Geology, 102, 47–65.

Shiraishi, K., Hiroi, Y. and Onuki, H. (1984) Orthopyroxene–bearing rocks from the Tenmondai and Naga–iwa Rocks in the Prince Olav Coast, East Antarctica: First appearance of orthopyroxene in progressive metamorphic sequence. Memoirs of National Institute of Polar Research, Special Issue 33, 126–144.

Shiraishi, K., Hokada, T., Fanning, C.M., Misawa, K. and Motoyoshi, Y. (2003) Timing of thermal events in eastern Dronning Maud Land, East Antarctica. Polar Geoscience, 16, 76–99.

Shiraishi, K., Yoshida, M., 1987. Explanatory text of geological map of Botnneset. Antarctic Geological Map Series, Sheet 25 (Botnneset). NIPR (9 pp.).

Spear, F.S. (1993) Metamorphic Phase Equilibria and Pressure-Temperature-Time Paths.

Mineralogical Society of America, Washington, D. C., 799 pp.

Suda, Y., Kagashima, S., Satish-Kumar, M., Motoyoshi, Y., and Hiroi, Y. (2006) Geochemistry of mafic metamorphic rocks in the Lützow-Holm Complex, East Antarctica: Implications for tectonic evolution. Polar Geoscience, 19, 62–88.

Suzuki, K., and Kawakami, T. (2019) Metamorphic pressure–temperature conditions of the Lützow–Holm Complex of East Antarctica deduced from Zr–in–rutile geothermometer and Al2SiO5 minerals enclosed in garnet. Journal of Mineralogical and Petrological Sciences.

Takahashi, K. and Tsunogae, T. (2017) Carbonic fluid inclusions in a garnet–pyroxene granulite from Austhovde in the Lützow–Holm Complex, East Antarctica: Implications for a decompressional P–T path. Journal of Mineralogical and Petrological Sciences, 112, 132–137.

Takahashi, K., Tsunogae, T., Santosh, M., Takamura, Y., and Tsutsumi, Y. (2018) Paleoproterozoic (ca. 1.8 Ga) arc magmatism in the Lützow-Holm Complex, East Antarctica: Implications for crustal growth and terrane assembly in erstwhile Gondwana fragments. Journal of Asian Earth Sciences, 157, 245–268.

Takamura, Y., Tsunogae, T. and Tsutsumi, Y. Neoproterozoic protolith forming and late Neoproterozoic-Cambrian granulite-facies metamorphism in the northeastern Lützow-Holm Complex, East Antarctica: Implications for P-T-t evolution of Gondwana fragments, National Institute of Polar Research The Eighth Symposium on Polar Science Abstract, 2017.

Takamura, Y., Tsunogae, T., Santosh, M., Malaviarachchi, S.P.K, and Tsutsumi, Y. (2015) Petrology and zircon U–Pb geochronology of metagabbro from the Highland Complex, Sri Lanka: Implications for the correlation of Gondwana suture zones.

Journal of Asian Earth Sciences, 113, 826–841.

Tomkins, H.S., Powell, R., and Ellis, D.J. (2007) The pressure dependence of the zirconium-in-rutile thermometer. Journal of Metamorphic Geology, 25, 703–713.

Watson, E.B., Wark, D.A., and Thomas, J.B. (2006) Crystallization thermometers for zircon and rutile. Contributions to Mineralogy and Petrology, 151, 413–433.

White, R.W., Powell, R., Holland, T.J.B., Johnson, T.E. and Green, E.C.R. (2014) New mineral activity–composition relations for thermodynamic calculations in metapelitic systems. Journal of Metamorphic Geology, 32, 261–286.

Whitney, D.L. and Evans, B.W. (2010) Abbreviations for names of rock–forming minerals. American Mineralogist, 95, 185–187.

Yanagi, A., Hiroi, Y., and Kato, M. (2011) Volcanic rock-like inclusions enclosed within garnet porphyroblast in eclogitic rock from Rundvågshetta, the Lützow-Holm Complex, East Antarctica. The 31st Symposium on Polar Geosciences Abstract.

Yanai, K., Kizaki, K., Shiraishi, K., Hiroi, Y. and Kanisawa, S. (1984) Explanatory Text of Geological Map of Akarui Point and Naga–Iwa Rock, Antarctica. Antarctic Geological Map Series Sheet 20. National Institute of Polar Research, Japan.

Yang, P., and Rivers, T. (2002) The origin of Mn and Y annuli in garnet and the thermal dependence of P in garnet and Y in apatite in calcpelite and pelite, Gagnon terrane, western Labrador. Geol. Mater. Res. 4, 1–35.

Yardley, B.W.D. (1977) An empirical study of diffusion in garnet. American Mineralogist, 62, 793–800.

Yoder, H.S. and Tilley, C.E., (1962) Origin of Basalt Magmas: An Experimental Study of Natural and Synthetic Rock Systems. Journal of Petrology, 3, 342–532.

Yoshimura, S., Kuritani, T., Matsumoto, A., and Nakagawa, M. (2019) Fingerprint of

silicic magma degassing visualised through chlorine microscopy. Scientific Reports, 9, article number 786.

Zack, T., Moraes, A.R., and Kronz, A.A. (2004) Temperature dependence of Zr in rutile: empirical calibration of a rutile thermometer. Contributions to Mineralogy and Petrology, 148, 471–488.